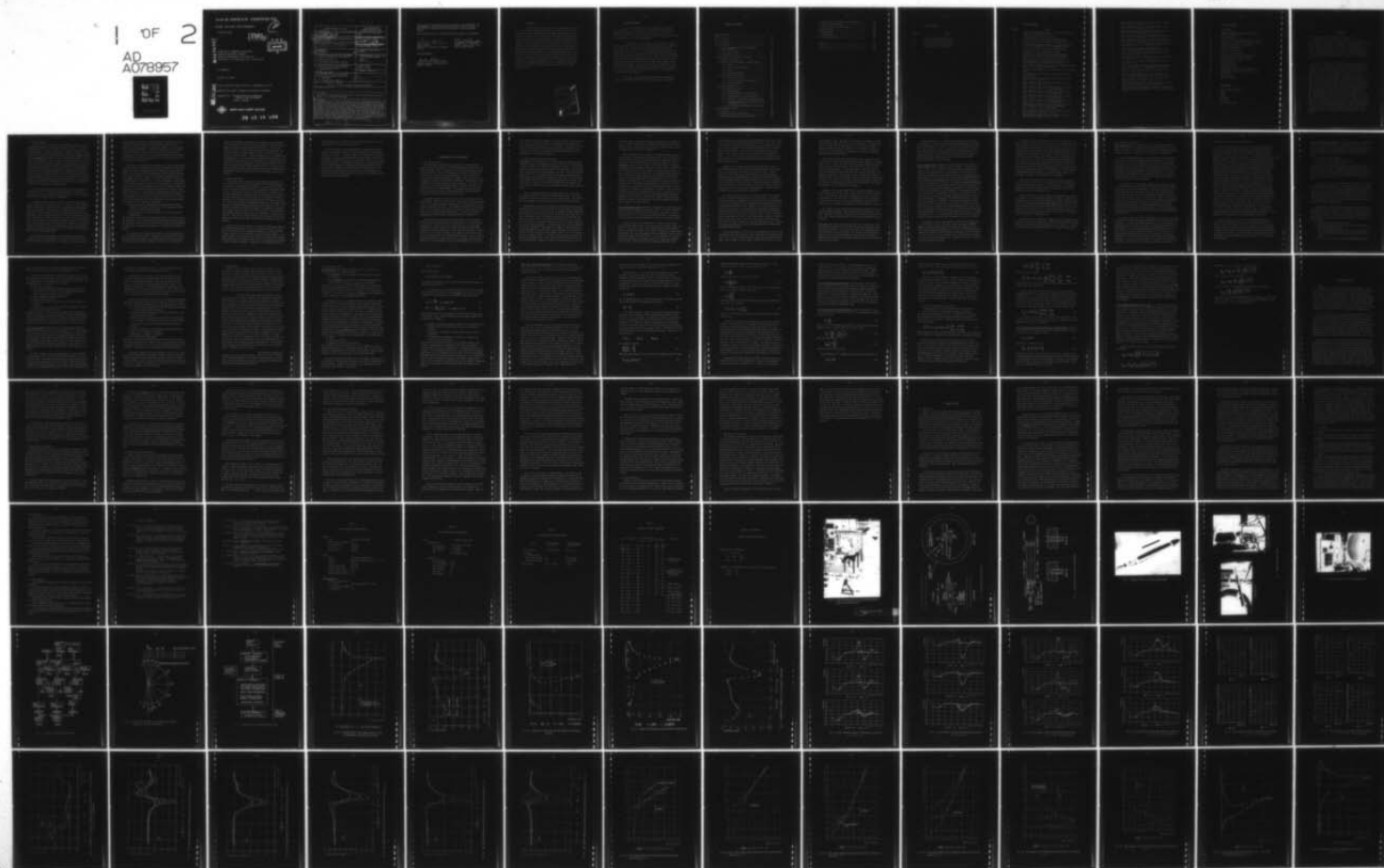


AD-A078 957 VON KARMAN INST FOR FLUID DYNAMICS RHODE-SAINT-GENESE--ETC F/6 20/4
VARIATION OF SPANWISE CIRCULATION ACROSS AN AIRCRAFT FUSELAGE: --ETC(U)
OCT 79 R DOWNSWILLO AFOSR-79-0099
UNCLASSIFIED VKI-1979-22 EOARD-TR-80-4 NL

1 OF 2

AD
A078957



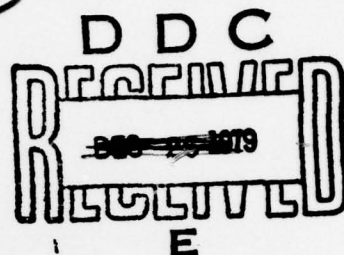
VON KARMAN INSTITUTE

FOR FLUID DYNAMICS

AFOSR 79-0099

AD A078957

LEVEL II



VARIATION OF SPANWISE CIRCULATION
ACROSS AN AIRCRAFT FUSELAGE :
Pressure measurements for a body of
revolution in the presence of a lifting wing

R. DOWGWILLO

October 12, 1979

DDC FILE COPY

Final Scientific Report, April 1, 1979-March 31, 1980

Approved for public release; distribution unlimited

Prepared for : European Office of Aerospace
Research and Development
London, England



RHODE SAINT GENESE BELGIUM

79 12 18 099

15 - AFO SR - 79-0099

16 2341 17 D1

12/187

19 REPORT DOCUMENTATION PAGE		READ INSTRUCTIONS BEFORE COMPLETING FORM
1. Report Number EOARD TR-88-4	2. Govt Accession No.	3. Recipient's Catalog Number
4. Title (and Subtitle) VARIATION OF SPANWISE CIRCULATION ACROSS AN AIRCRAFT FUSELAGE: Pressure measurements for a body of revolution in the presence of a lifting wing.	5. Type of Report & Period Covered Final Scientific Report 1 APR 1979 - 31 MAR 1980	
		6. Performing Org. Report Number VKI Project Report 1979-22
7. Author(s) R. Dowgwill	8. Contract or Grant Number AF SR-79-0099	
9. Performing Organization Name and Address von Karman Institute for Fluid Dynamics Chaussée de Waterloo, 72 B - 1640 Rhode Saint Genèse, Belgium	10. Program Element, Project, Task Area & Work Unit Numbers 61102F 2301 - D1 11/12 Oct 79	
11. Controlling Office Name and Address European Office of Aerospace Research and Development / LNV Box 14 FPO New York 09510	12. Report Date October 12, 1979	
14. Monitoring Agency Name and Address European Office of Aerospace Research & Development Box 14 FPO New York, 09510	13. Number of Pages 104	
15.		
16. & 17. Distribution Statement Approved for public release; distribution unlimited.		
18. Supplementary Notes		
19. Key Words aerodynamic interference-wind tunnel tests-pressure measurements- bodies of revolution-fuselages		
20. Abstract An experimental study of the load characteristics of a separated wing and body model was carried out in the VKI low speed wind tunnel. Measurements of the pressure distribution on the model were made for different wing pitch angles and wing-body gap heights. The body pitch angle was zero. Derived data consist of body chordwise and spanwise lift distributions, wing spanwise lift distribution and wing pitching moment distribution. Results show that the body always develops negative lift in the presence of the wing. Wing and body spanwise lift distribution magnitude are monotonically decreasing from centerline to wing root, but their distribution curve shapes are different. When the wing-body gap is filled, the spanwise lift distribution for the resultant configuration shows the lift increasing from wing root to centerline, a result considered typical of a high-mounted wing.		

367 475 79 12 18 099

This report has been reviewed by the Information Office (EOARD/CMI) and is releasable to the National Technical Information Service (NTIS). At NTIS it will be releasable to the general public, including foreign nations.

This technical report has been reviewed and is approved for publication.

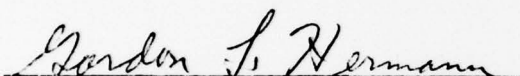


JOHN T. MILTON
Scientific and Technical Information
Officer



ROBERT D. POWELL, Major, USAF
Chief, Flight Vehicles

FOR THE COMMANDER



GORDON L. HERMANN, Lt Colonel, USAF
Executive Officer

ABSTRACT

An experimental study of the load characteristics of a separated wing and body model was carried out in the von Karman Institute low-speed wind tunnel. Measurements of the pressure distribution on the model were made for different wing pitch angles and wing-body gap heights. The body pitch angle was zero. Derived data consist of body chordwise and spanwise lift distributions, wing spanwise lift distribution and wing pitching moment distribution. Results show that the body always develops negative lift in the presence of the wing. Wing and body spanwise lift distribution magnitude are monotonically decreasing from centerline to wing root, but their distribution curve shapes are different. When the wing-body gap is filled, the spanwise lift distribution for the resultant configuration shows the lift increasing from wing root to centerline, a result considered typical of a high-mounted wing.

Accession For	
NTIS	<input checked="checked" type="checkbox"/>
DDC TAB	<input type="checkbox"/>
Unannounced	<input type="checkbox"/>
Justification	<input type="checkbox"/>
Ex	
Distribution /	
Availability Codes	
Dist	Availand/or special

ACKNOWLEDGEMENTS

I wish to extend my sincere thanks to Professor John Sandford, my advisor, for his invaluable counsel and support throughout the course of the project, and to Mr. Jean-Louis Hauchart for his ready assistance during the design and execution of the experimentation.

I also offer my gratitude to the following individuals without whose help this project would have been all the more difficult : Messrs Jacques Missart, Paul Desmet and Alain Petit of Facility L-1 and stagiaires Claude Radier and Derek Mess for their assistance during the testing; Professor Domenico Olivari, Messrs Roger Borres, Felix Thiry, and Patrice Pleitinx for their instrumentation support; Mr. Robert Lejour and his staff for their machine work. Mr. Jean-Claude Lobet for his photography; fellow students Eberhart Meineke, Peter Hambling, Constantine Cosmidis and Luis Lorenzo for availing me of their experience and William Herkes for his assistance in finalizing this report.

Finally, my thanks to all the remaining faculty, staff, and students who assisted in manners all and sundry.

TABLE OF CONTENTS

Acknowledgments	2
List of Tables	5
List of figures	6
List of symbols	8
1. Introduction	9
1.1 Lift characteristics of wing-body configurations	9
1.2 The panel method	10
1.3 The present study	12
2. Experimental set-up and procedure	14
2.1 General description	14
2.2 Model and model support system design	15
2.2.1 Body	15
2.2.2 Body support system	16
2.2.3 Wing	18
2.2.4 Instrumentation	19
2.3 Experimental procedure	21
2.3.1 Pretest set-up	21
2.3.2 Test set-up and calibration	23
2.3.3 Test procedure	24
2.4 Data reduction	26
2.5 Uncertainty analysis	27
2.5.1 Methodology	27
2.5.2 Test condition uncertainties	29
2.5.3 Instrumentation uncertainties	32
2.5.4 Pressure coefficient uncertainties .	32
2.5.5 Pressure coefficient uncertainty of galvanometer data	34
2.5.6 Integrated coefficient uncertainty	35
3. Experimental results	37
3.1 General	37
3.2 Repeatability and symmetry	38
3.3 Wing-body pressure distributions	39

3.4 Body and wing loading distributions	41
3.5 Flow visualization	44
3.6 Wing-body with sealed gap	45
4. Summary remark	47
4.1 Discussion	47
4.2 Conclusions	51
4.3 Recommendations	52
References	53
Tables	55
Figures	61

List of Tables

<u>Table</u>	<u>Title</u>
1	Model geometry specification
2	Test condition uncertainties
3	Instrumentation uncertainties
4	Summary of tests performed

LIST OF FIGURES

<u>Figure</u>	<u>Title</u>
1	View of experimental set-up, with wing and body models and instrumentation.
2	Model geometry and nomenclature.
3	Design details of ellipsoid-cylinder model.
4	"Exploded" view of ellipsoid-cylinder model.
5	View of body support system : a) sting and body; b) vertical support strut and support frame.
6	View of operator's station instrumentation.
7	Schematic of data acquisition system.
8	Location of instrumented wing stations and points of placement of the body tap meridian.
9	Organization of the data reduction process.
10	Demonstration of least-squares curve fit used for integration of pressure distributions.
11	Comparison of data logger and galvanometer pressure data : a) for body; b) for wing.
12	Pressure distribution for wing station in unsteady flow.
13	Demonstration of symmetry in the body pressure distributions.
14	Body chordwise pressure distributions for high-wing, $\theta_w = 3^\circ$, $H/C = .45$.
15	Body chordwise pressure distributions for low-wing, $\theta_w = 3^\circ$, $H/C = .45$.
16	Body chordwise pressure distributions for high-wing, $\theta_w = 3^\circ$, $H/C = .39$ (minimum gap).
17	Body chordwise pressure distributions for high-wing, $\theta_w = 9^\circ$, $H/C = .45$ (minimum gap).
18	Wing chordwise pressure distributions for high-wing, $\theta_w = 3^\circ$, $H/C = .39$ (minimum gap).
19	Wing chordwise pressure distributions for high-wing, $\theta_w = 9^\circ$, $H/C = .45$ (minimum gap).
20	Comparison of wing and body chordwise pressure distribution at $Y/S = .064$ for high-wing, $\theta_w = 3^\circ$, $H/C = .39$ (minimum gap).
21	Body chordwise normal force distribution versus gap height for high-wing, $\theta_w = 3^\circ$.
22	Body chordwise normal force distribution versus gap height for high-wing, $\theta_w = 9^\circ$.

- 23 Body chordwise normal force distribution versus gap height for low-wing, $\theta_w = 3^\circ$.
- 24 Body chordwise normal force distribution versus gap height for low-wing, $\theta_w = 9^\circ$.
- 25 Body chordwise normal force distribution versus wing pitch angle for low-wing, $H/C = .45$.
- 26 Body spanwise normal force distribution versus gap height for high-wing : a) $\theta_w = 3^\circ$, b) $\theta_w = 9^\circ$.
- 27 Body spanwise normal force distribution versus gap height for low-wing : a) $\theta_w = 3^\circ$; b) $\theta_w = 9^\circ$.
- 28 Wing-spanwise lift distribution versus gap height for high-wing : a) $\theta_w = 3^\circ$; b) $\theta_w = 9^\circ$.
- 29 Wing chordwise pressure distribution at $Y/S = .169$ versus gap height for high-wing, $\theta_w = 3^\circ$.
- 30 Wing chordwise pressure distributions for high-wing, $\theta_w = 9^\circ$, $H/C = .51$.
- 31 Wing spanwise lift distribution versus gap height for low-wing : a) $\theta_w = 3^\circ$; b) $\theta_w = 9^\circ$.
- 32 Wing lift curve versus wing station for high-wing, $H/C = .39$.
- 33 Wing quarter-chord pitching moment distributions versus gap height : a) high-wing; b) low-wing.
- 34 Body oil flow visualization for low-wing, $\theta_w = 9^\circ$: a) $H/C = .39$; b) $H/C = .45$.
- 35 Body chordwise normal force distribution for high-wing with sealed gap, $\theta_w = 3^\circ$, $H/C = .40$.
- 36 Body oil flow visualization for high-wing with sealed gap, $\theta_w = 3^\circ$, $H/C = .40$.
- 37 Configuration spanwise lift distribution for high-wing with sealed gap, $\theta_w = 3^\circ$, $H/C = .40$.
- 38 Upper surface wing chordwise pressure distribution versus gap height, including sealed gap, for high-wing, $\theta_w = 3^\circ$.

LIST OF SYMBOLS

c	wing chord
h	distance between body axis and wing quarter-chord point
s	wing semi-span
s_x	sample standard deviation for variable X
X	chordwise coordinate or general variable
\bar{X}	sample mean for the variable X
Y	spanwise coordinate
Z	vertical coordinate
C_l	local lift coefficient
C_m	local pitching moment coefficient
C_n	local normal face coefficient
C_p	pressure coefficient
P	static pressure
Q	dynamic pressure
μ_x	population mean for the variable X
σ_x	population standard deviation for the variable X
θ	pitch angle
ψ	body roll angle

Subscripts :

∞	freestream conditions
w	wing
b	body
c	chordwise
s	spanwise
l	local conditions

1. INTRODUCTION

1.1 Lift Characteristics of Wing-Body Configurations

A feature of the classic airplane configuration is the intersection of essentially non-lifting components (fuselages and nacelles) with lifting components (wings and tail surfaces). The resultant flow in the region of such wing-body junctions is highly three-dimensional and subject to large gradients, making it at once difficult and important to analyze. Significant drag will arise from poor junction aerodynamics and relatively large, wide-spread loads are induced by one component on another.

Certainly the crux of any airplane configuration is its ability to generate lift. A body, alone, does not develop much lift owing to its low aspect ratio, but in the presence of a wing its lifting capability is greatly enhanced. The mechanism responsible for this effect can be considered to be the local flow deflection created by the lifting wing¹. The portion of the body ahead of the wing is affected by upwash, and that behind the wing by downwash. In the area of the junction itself the flow is directed roughly along the chord of the wing, corresponding to a near-constant downwash. This modification of the velocity field manifests itself in the "carry-over" of the wing's high and low pressure regions onto the intervening body.² These pressures have a lower magnitude than would exist on the now-absent wing surface, but the larger body chord provides more area for the pressures to act upon. The result is that the geometric discontinuity of the wing chord at the junction is not reflected in a discontinuity of the spanwise lift distribution; instead the interference serves to smooth the distribution. Still, the lift of the wing-body combination is always less than that of the wing alone.³ It is thus of great importance to be able to assess the characteristics of a particular configuration during the design process.

1.2 The Panel Method

With the constant demand for better aerodynamic prediction and the increasing capability of electronic computers, the class of numerical techniques known as "panel methods" is fast becoming a principal tool in the analysis of airplane configurations. The basic feature of these methods is the ability to model an entire potential flow field by replacing the boundaries with "panels" consisting of distributions of certain essential singularities, such as sources, doublets, and vortices. Application of the Green's Function Technique to the differential equation for potential flow gives the form of these singularities and their relation to the boundary conditions of the problem. Thus, the field equation is transformed into an integral equation on the boundaries of the field. In solving this new equation the entire flow is not considered directly and, in principle, little or no restrictions are placed on the shape or number of the boundaries that now constitute the domain of the equation. The method offers distinct advantages when dealing with complex aircraft configurations immersed in an infinite fluid.

Panel methods had their practical beginnings with the formulation of Smith and Hess⁴ for a general, non-lifting body in subsonic flow. Since that time these methods have been generalized to include unsteady, compressible flows about lifting configurations.

A formulation which serves to illustrate the general approach and which is presently of particular interest is that due to Hunt and Semple of British Aerospace⁵. Here the chosen singularities are distributed sources and doublets. Wetted surfaces are represented by a system of flat panels, each containing a source distribution of uniform strength. This suffices for non-lifting components. For lifting components, a suitable camber surface is added, represented by panels of distributed doublets. On each such panel the doublet strength is assumed to vary linearly in two chosen directions. The problem is to determine the source distribution and spanwise circulation distribution satisfying an integral equation for the prescribed normal flow at the surface of the body and a Kutta condition, where appropriate.

With the functional dependence of the singularity distributions specified, as above, the integrals of the subject equation may be evaluated--analytically or numerically--for each panel. In this manner the

original integral equation is transformed into a linear system of equations. The source strengths on the wetted panels and the doublet strengths at the Kutta points constitute the unknowns. The zero-normal-velocity boundary condition is enforced at each wetted panel centroid and the Kutta points. After solution, insertion of the new-found strengths into a special form of the original integral equation enables the flow velocity--and hence the pressure--to be calculated at any point on the surface or in the flow.

With practical formulations and computer codes in hand, much emphasis currently centers on improving the accuracy of the method. In the first instance the concern is with how well the solution of the discretized problem represents the flow described by the original integral equation. Here, "accuracy" relates to how well the boundary conditions are satisfied between collocation points, i.e. points constrained to satisfy the conditions exactly. Failure to do so is termed "leakage", and can distort the calculated tangential velocities. The possibilities for improvement in this respect are revealed by the fact that, in principle, a given configuration can be exactly represented by any number of different singularity distributions. In practice the achievable accuracy becomes a function of panel size, singularity "mix", and the manner of distributing the singularities over the panels. Obviously what is desired is the discretization scheme which gives the best accuracy for the minimum effort. Two approaches to this end can be identified:

- 1) an increase in the complexity of the singularity distribution function of the panels, much like the use of high-order "super-elements" in finite element methods,
- 2) an optimization of the use of simple, first-order singularity distributions.

The Hunt-Semple formulation described earlier adopts the second tack for the construction of a desirable chordwise doublet distribution for lifting components. The aim is to increase accuracy without placing additional requirements on computer performance, e.g. storage capacity and word length.

The second point of concern about accuracy is the representation of the less ideal, more real flows. Of course, a purely potential analysis can not describe the details of non-potential flows such as those found in boundary layers and wakes. However, in the limit of large Reynolds

numbers and negligible unintentional flow separation, some important effects of such thin shear layers can be modeled by a potential analysis guided by suitable experimentally-derived criteria. The classical example of such a criterion is the Kutta-condition for fixing the total circulation about a lifting aerofoil section, a circulation due, in reality, to viscous effects. Practical application of the condition has been enhanced as a result of continued experimental investigation of the relaxation⁶ and trajectory⁷ of the real wake near a wing trailing edge. Other work has provided information on the effective spanwise location of the concentrated vortex system found at the tip of a lifting wing or deflected control surface. Thus there still exists an important role for experimental study even within the context of low speed, inviscid aerodynamics.

1.3 The Present Study

While panel methods offer a means of studying and predicting the interference effects of aircraft configurations, a difficulty arises in the modeling of configuration lift which is not present for the wing-alone case, namely the body's ability to contribute a significant amount of lift. To account for this lift, the body becomes a candidate for doublet singularities. However, though the lift variation is expected to be smooth, the absence of a Kutta-condition on the body for fixing the magnitude of the circulation associated with this lift leaves the spanwise circulation distribution incompletely specified. The method of optimizing the chordwise doublet distribution is also affected. With little information available to help the situation³, some arbitrary assumption must be made about the nature of the lift carry-over⁵. For a wing-body the assumption generally made is that the circulation is constant across the body. This becomes totally inadequate for configurations with small wing-span-to-body-diameter ratios and requires more explicit empirical guidance.

The aim of the present study is to provide some experimental data on the loading characteristics of a general wing-body combination. It is part of an on-going study of wing-body combinations in sideslip,^{8,9,10}, a flight situation not yet well predicted by panel method schemes. A two component model is used, consisting of a body of revolution and a lifting, finite span wing. By varying the gap between the components, the build-up of induced loading is examined. Convergence to both high-wing and low-

wing configurations is obtained so far as the model will allow. In the high-wing case the gap is ultimately sealed.

Section 2 describes the testing performed. Equipment and instrumentation are treated in detail in order to document new items and aid testing in the future. A complete subsection is devoted to an uncertainty analysis of both the basic measurements and the derived coefficients. The results are presented in Section 3, primarily in terms of force coefficient distributions. Of particular interest are the spanwise distributions on the wing and body. Representative pressure distributions are also included. Section 4 contains a discussion and conclusion of the results with recommendations for future work. It is hoped that this study will ultimately prove useful in the treatment of wing-body combinations by potential flow modeling.

2. EXPERIMENTAL SETUP AND PROCEDURE

2.1 General Description

The experiments reported here were performed in the three-meter diameter open-jet wind tunnel at the von Karman Institute (Facility L-1) during April-May, 1979. An overall view of the test arrangement is presented in Figure 1. The test configuration consisted of an ellipsoid-cylinder and a straight, untwisted wing placed in close proximity to each other but supported independently. Figure 2 gives a sketch of this arrangement along with some pertinent terminology. The definition of the coordinate axes follows standard aeronautical practice. The roll angle convention is that normally used for bodies of revolution¹¹, while the body description comes from DATCOM³. The wing-body gap distance used here is taken from the earlier experimental work of Jacobs and Ward². A summary of the model geometry is given in Table 1.

Independent variables of the test were the wing pitch angle and the wing-body gap. Body pitch and yaw angles and wing yaw angle were nominally zero. The primary dependent variables were the measured static pressure distributions on the model. Two methods were employed for data acquisition. In the primary system, data were digitized and recorded on magnetic tape by a semi-automatic data logger. A backup system required recording data by hand from the analogue display of a galvanometer.

Two main objectives have influenced the design of the experiment. First, the model should represent, in a general way, a relevant airplane configuration. To this end both the body shape and the overall model configuration resemble those of the current generation of wide-bodied transports. The necessary absence of external cockpit geometry, or "cab", from the model also better typifies these airplanes, since the relative size of the cab decreases with increasing body diameter. Second, the flow conditions should be as nearly "potential" as possible. Since the ultimate aim is to provide guidance for panel methods modeling, the reported

test conditions should be amenable to treatment by such a method to be of use. This means that large regions of separation and/or significant separation-induced unsteadiness are to be avoided. Translating this into practical terms, surface oil flow visualization was employed to reveal any extensive separation along with realtime data monitoring to detect unsteadiness in the measured pressures.

2.2 Model and Model Support System Design

2.2.1 Body The body consists of an semi-ellipsoid followed by a right circular cylinder, an arrangement generally referred to as an ellipsoid-cylinder. Details of the body are illustrated in Figure 3. The nose and cylinder are fabricated of aluminum and steel, respectively, and joined by three countersunk bolts running through a lap joint. The joint is placed downstream of the nose tangency point to facilitate nose-body matching. The resultant joint is barely discernable to the touch. A coat of black polyurethane paint provides a contrasting background for oil flow visualization and is sanded to a matte finish suitable for photography. The final surface is generally smooth, with shallow streamwise brush marks in places.

Two steel bulkheads bolted to internal flanges near either end of the cylinder connect the body to the support system sting. These bulkheads may be removed to provide access to the body interior. The forward unit also provides the mounting point for the roll motion drive shaft.

Instrumentation consists of 84 pressure taps located along a meridian extending from near the nose tip to the end of the cylinder. The 1mm diameter taps are set normal to the surface at intervals of 20mm, reducing to 10mm from about .25c forward of to 1.25c behind the wing leading edge station. To provide a means of aligning the body with the freestream, additional taps are used to form a cruciform pattern at two nose stations. These two stations correspond, respectively, to areas of highest and lowest surface velocity gradient, as calculated for zero incidence potential flow by Hess and Smith⁴. This results in a higher or lower sensitivity to any unaligned flow over the body. In all the body is fitted with 90 taps: 26 on the nose and 64 on the cylinder. Details of the tap construction are included in Figure 3. Note that different designs are used for the nose and cylinder taps. Those taps selected for monitoring are connected by thin plastic tubing to a 48-port scanivalve mounted at the aft

end of the body. The scanivalve extends through one of the lightening holes in the aft bulkhead and is attached to the bulkhead by two bolts. Thus the device can be extracted for inspection and maintenance. This and other details can be seen in Figure 4.

Much consideration has been given to defining the body geometry in order to realize the objectives outlined earlier. Of major concern are the separation and vortex systems generally associated with bodies at incidence. The smooth, blunt nose is intended to delay the onset of asymmetric vortex formation to angles of incidence beyond the maximum total angle of 18° anticipated for future testing. Unfortunately, this has little if any effect on the symmetric vortex formation, which is more a function of body fineness ratio. The bluntness should also minimize the sometimes large variations in flow pattern found during the rotation of pointed bodies due to small asymmetries in the nose tip geometry. The actual choice of an ellipsoid nose reflects the desire for a shape which is both simple and representative. With respect to the latter point, it should be noted that Munk's general theory of bodies of revolution¹² incorporates an "equivalent ellipsoid" as a basis for describing the geometry of an arbitrary body. Here, an examination of the fineness ratios exhibited by several wide-bodied transport airplanes provided a relevant value of eccentricity. Finally, the maximum body diameter was chosen to be identical to that of the tangent-ogival body used by Repetti in related tests.¹⁰

2.2.2 Body Support System The body is supported by a sting-type support system expressly designed for the present study. It is seen in Figure 5 as it was installed in the tunnel test section. The system provides remote control of roll, pitch, and vertical translation. Yaw and horizontal translation may be introduced by movement of the entire assembly.

The main elements of the system are the sting, vertical support strut, and the support stand. The sting comprises a spindle, flare, and extension tube. These pieces are of finished steel and use threaded joints to facilitate assembly. The spindle, a 900mm long by 50mm diameter thick-walled tube, passes through the two body bulkheads, bearing the body loads and defining the body roll axis. It is followed by a 10° conical flare which provides the structural transition to the larger-diameter extension tube. The flare also reacts body drag loads via a Teflon

thrust bearing placed between the body aft bulkhead and the flare. Teflon is used to minimize friction during body roll motions. Body thrust loads are reacted by an aluminum split ring secured to the spindle on the opposite of the aft bulkhead. A Teflon washer separates the ring and bulkhead to reduce friction. Some details of the assembly can be seen in Figure 4. The extension tube places the body away from interfering effects of the vertical support strut and carries the consequently large bending moments. The tube is 1500mm long by 100mm in diameter and has a wall of 10mm thickness.

Integral with the sting is the body roll motion drive system. A plate welded to the aft end of the extension tube provides the mounting point for a high torque, low shaft r.p.m. electric motor. Torque is transmitted to the body along a 10mm diameter steel shaft extending through the hollow sting and ending in a small steel plate which bolts to the body forward bulkhead. A brass cylinder with two set screws couples the motor and shaft. Reference points for marking the body's position in roll are provided by white paper disks placed at 10° intervals around the circumference at the aft end of the body. Each disk is labeled with its angular position from the pressure tap meridian.

Two square section steel tubes, one inside the other, are the major elements of the vertical support strut. The inner tube, to which the sting is attached, is supported by a screwjack located on the upwind side of the strut. Connection of the screwjack and the inner tube is made via a thick-walled tube bolted to the screwjack at one end and pinned to the inner tube at the other. The lower end of the screwjack runs through a threaded bearing bolted to a platform on the outer strut. This bearing can be driven by an electric motor and chain. Chain tension is maintained by an adjustable idler wheel. The vertical strut assembly is stabilized by a large space frame, to which the outer tube is connected by two pin joints. The upper connection is made directly to the frame. The lower connection communicates with the frame through another screwjack-and-threaded-bearing assembly.

Vertical translation of the sting is accomplished by rotation of the threaded bearing by the chain drive, thus displacing the screwjack and the inner tube. A liberal coating of grease reduces friction between the two tubes. Useful length of the screwjack is 900mm, which defines the avail-

able translation span. The datum of this span can be adjusted by changing the length of the tube at the top of the screwjack. Pitching of the sting is accomplished by translating the second screwjack through its threaded bearing, causing the outer tube to pivot about the upper pin joint. Since such movements are infrequent, the bearing is turned by hand with a purpose-built wrench.

The sting is carried by a platform welded to the upper end of the inner tube. To enable the sting length to be readily adjusted, a clamped joint is used to fasten the sting to this platform. Uploads and lateral loads are reacted by three U-bolts fitted over the extension tube and connected to the platform. A steel pad welded to each bolt provides increased bearing area between bolt and tube to diffuse the loads. Downloads are transmitted to the platform via two contoured wooden blocks, which also serve to diffuse the loads. Friction alone reacts loads acting parallel to the sting axis. By first supporting the weight of the model and sting and then slackening the U-bolts, the sting may be slid forward and backward to give the desired sting length.

Yawing of the sting when under load is suppressed primarily by the interference between the two square section tubes of the vertical support strut. A more positive mechanism is available in a pair of set screws incorporated into the outer strut. By tightening the screws against the inner tube, motion in yaw can be nearly eliminated. The screws also provide a means of making fine adjustments of the yaw angle of the sting.

The vertical support system has been designed to maximize the use of readily available equipment. The electric motor and chain drive, screwjacks, bearings, and support frame have been borrowed from other test rigs. Their original functions have in no way been compromised by their use here.

2.2.3 Wing The wing is as supplied by D.F.V.L.R., Germany, and is the same wing used by Repetti.¹⁰ A complete description of the wing can be found in that reference. For the present tests, four inboard stations are monitored for a total of 124 taps. The taps are vented through steel tubing let out of the starboard wingtip, where they are connected by plastic tubing to a series of scanivalves mounted on an elevated platform placed near the wingtip.

Supporting the wing is a network of wires connected to the tunnel overhead balance. The wires are tensioned by weights hung from the wing. Two attachment points are located on the wing itself and define the pitch axis. This is located at .3c. A third point is at the end of a cantilevered arm attached to the wing trailing edge, providing the means for varying pitch angle. Gaps in the wing necessitated by the suspension points are blanked off with plastic tape to minimize flow between pressure and suction sides of the wing.

2.2.4 Instrumentation Components of the data acquisition system are shown in Figure 6 and a schematic is given in Figure 7. The principal feature of the system is the use of the data logger and galvanometer in parallel. This arrangement was adopted because of uncertainties surrounding the reliability of the logger and a desire to monitor the pressures during the course of the test. The data logger (DATAFORCE 008 with a model 100 SIGNAL CONDITIONER) was the primary acquisition instrument, with the three moving-coil, light spot galvanometers (SEFRAM GALVANOMETRE) serving as a back-up. Problems with electrical interactions between the logger and the galvanometers required the introduction of a 9.1k resistor to increase the galvanometer input impedance. This interaction results from the back-e.m.f. generated by the moving coil during deflection. The resistance value selected was that which allowed the highest sensitivity of the data logger. Unfortunately, the additional resistance is detrimental to galvanometer performance. The resultant measurement circuit resistance is over ten times the coil resistance, reducing the instrument's sensitivity. Moreover, the resultant damping ratio of the instrument is not optimum for dynamic response. For the basically steady-state measurements made here, this affects the instruments response to a change in scanivalve tap. A less compromising system using isolation amplifiers had been considered initially, but the required units were unavailable.

Measurements of model static pressures and freestream dynamic pressure were made with three strain gage pressure transducers (STATHAM PM5TC). Maximum rated differential pressures were 350mm H₂O for the freestream and wing and 105mm H₂O for the body. The wing and body transducers were connected to their respective scanivalves by plastic tubing. A pitot tube placed in the exit plane of the settling chamber provided the input for the freestream pressure. Reference for all the transducers was local atmospheric pressure.

In order to reduce overall response time, the transducers for the wing and body were placed as close as possible to the scanivalves. The body transducer was secured to the screwjack extension tube of the vertical support strut, while that for the wing was secured to the pole supporting the wing scanivalves. Both were embedded in plastic foam to isolate them from vibration. The reference sides were vented to local atmospheric pressure through large diameter plastic tubing routed to a point outside the test section jet. Transducer power and adjustment were supplied by two inhouse transducer power supplies different from those normally packaged with these transducers at V.K.I. These units gave better isolation from 50Hz and were grounded to the mixing box (see Figure 7) to help suppress drift of the logger zeros. A Betz manometer (E. SCHILTKNECHT, ING.) provided an accurate pressure reference for transducer calibration and setting the tunnel windspeed.

Local static temperature was measured with a mercury thermometer located near but outside the jet. While the jet static temperature is actually higher than that used here, the difference is not considered significant. Local atmospheric pressure was measured with a mercury barometer installed in an adjacent room.

Angular displacements of the model were determined with two different instruments. For setting body and wing pitch angle, a bubble level and quadrant was used. For determining body roll angle during the course of a test, a transit (WILD NIVEAU DE HAUTE PRECISION N3) sighted on the body provided a datum for the roll angle markers found at the aft end of the body. The roll motion itself was remotely controlled using a bipolar switch inserted in the power lead to the roll motor, allowing the body to be rotated in either direction.

Inhouse-built units comprising a trigger button and a lighted display were used to control the scanivalves. A separate box contained a vernier control for tunnel speed and an emergency stop. For operator convenience, a remote data entry trigger substituted for the logger's built-in unit.

2.3 Experimental Procedure

2.3.1 Pretest Setup The simultaneous use of separate wing and body models dictated careful prepositioning for proper definition of the configuration under test. Moreover, it was desirable to define the configuration as simply as possible for ease in set-up and repeatability.

Following established practice, the wing attitude was determined by survey alone. Previous testing had fixed the wing in the central horizontal plane of the jet at essentially zero roll angle, as determined by a bubble level. Yaw attitude was set to zero by rotation of the overhead balance turntable until the wing leading edge was parallel to the exit plane of the settling chamber. Pitch attitude was set by placing the bubble level and quadrant on a board whose lower surface contour matched the upper surface of the wing and then adjusting the length of the wing's rear support wire as required.

The mobility of the body support system was relied upon to achieve the desired configuration. The body's fore and aft position was defined by setting the nose tip 700mm forward of a plumb bob suspended from the wing leading edge, with the wing at zero pitch. The maximum possible sting length was used in order to minimize the aerodynamic interference of the vertical support strut. This resulted in a body-strut separation of about 1m. To make the best use of the wing's pressure tap arrangement, the body was positioned off the geometric centerline of the wing to a region of high tap density. The final arrangement placed the body centerline 120mm outboard of the wing centerline. This also eliminated the possibility of structural interference between the sting/body and the aft support wire.

The desire to have the body be non-lifting in the absence of the wing required that the body be closely aligned with the tunnel freestream, i.e. the angles of incidence and sideslip should be zero. This alignment was performed using a combination of wind-off surveying and wind-on pressure measurements. For the initial yaw attitude, the body was positioned over a line on the test section floor parallel to the tunnel axis by using plumb bobs suspended from both ends of the model. Differential tightening of the two vertical strut set screws provided the necessary adjustments. The initial pitch attitude was the horizontal defined by a bubble level placed along the body surface, adjustments being made via

the support system 's pitch control mechanism.

Following this initial positioning, wind-on pressure measurements were taken to reveal differences between these (geometric) angles of pitch and yaw and the corresponding (aerodynamic) angles of incidence and sideslip actually seen by the body. Since it was impractical to remove the wing, the body was positioned as far as possible below it, at a gap distance of 690mm. The wing was set to zero degrees to further reduce interference. Originally, one of the cruciform tap groups was used for the body alignment. With the tap pattern set parallel to the pitch and yaw axes, misalignment was sensed as a pressure difference between taps located on opposite sides of the body axis. The body axis was then adjusted to null out these differences. Unfortunately, the method proved unreliable in practice. For example, nulling in pitch resulted in an unreasonably high nose-up angle of 4° . Oversensitivity of the system was probably the problem, in that small differences in the shape and axial location of the taps masked the misalignment effects. The alternate and more successful approach called for monitoring a single tap as the body was rotated, the resultant pressure map indicating the degree of symmetry of the flow. Both a tap on the nose and the midbody were used for this purpose. The alignment was considered adequate when the pressure variations at the nose station were within $\pm 2\text{mm H}_2\text{O}$ and those for the body station within $\pm .5\text{mm H}_2\text{O}$, or values of pressure coefficient of $\pm .04$ and $\pm .01$, respectively. The sensitivity of the nose was again apparent. Resultant pitch attitude was $.7^{\circ}$ nose-up and essentially zero yaw. With such a small correction, it was decided to use the surveyed pitch angle as the geometric angle of incidence and therefore achieve compatibility with the wing attitude reference. These wing and body alignments were not repeated during the testing.

On three occasions a leak check of the model pressure taps was performed. The procedure was to select the tap via the scanivalve control, apply a low pressure to the tap, and detect the pressure with the Betz manometer. With the pressure removed and the tap sealed (with a finger tip, for instance) a steady decline in pressure would indicate the presence of a leak. Care must be taken to avoid over-pressuring the scanivalve and thereby degrading the close tolerances of the rotating valve mechanism.

2.3.2 Test Set-up and Calibration Each test began with a configuration set-up and instrument calibration. Wing pitch angle was set in the manner described in 2.3.1. For practical reasons, the wing-body gap to be set was taken as the distance between the body and wing surfaces at the wing quarter chord, with the wing at 0° . The procedure was as follows:

- 1) set wing at 0° pitch angle
- 2) translate the body to give the desired gap
- 3) set wing to the test pitch angle

Since the wing was always above the body, a negative angle of pitch corresponded to a low-wing configuration at positive pitch angle. Since it was generally necessary to slacken the yaw motion set screws in order to move the body, each of these screws was fitted with a pair of interfering nuts to define the position of the screw for the proper yaw attitude.

Setting the body at a new vertical position required a new calibration of the roll attitude system. To accomplish this, the tap meridian was first set to the $\psi = 90^\circ$ location by suspending a plumb bob over the side of the body and then rotating the body until the tap meridian coincided with the point of tangency of the body surface and plumb line. With the position defined, the transit was sighted on the most convenient roll position marker. Once this marker was identified, all other roll positions could be inferred from it.

Calibration was performed separately for the two different data acquisition systems. In either case, the calibration pressure standard was provided by the Betz manometer connected via a manifold to the input side of the transducers. The galvanometer calibration was designed to enable pressure coefficients to be directly displayed. The procedure was as follows:

- 1) set mechanical, then electrical zeros
- 2) apply 50mm H₂O pressure, which represents the nominal value of the freestream dynamic pressure
- 3) place the resultant galvanometer output at a convenient point on the display scale by adjusting the transducer excitation voltage
- 4) set this point as $C_p = 1$ and scale-off the display accordingly.

Note that the usefulness of this method requires that the freestream dynamic pressure be held fairly constant throughout the test.

The data logger calibration established the scale factors relating input pressure to digital counts. Thus, the calibration was necessarily an integral part of the test data and, as such, was recorded on the logger magnetic tape. The procedure was as follows:

- 1) record test identifier
- 2) apply 50mm H₂O pressure and adjust the logger span to a count level which will accomodate the anticipated maximum absolute value of the pressure, then release pressure
- 3) record calibration pressure identifier
- 4) apply calibration pressure
- 5) record logger counts, taking three scans of data in quick succession
- 6) repeat steps 3 to 5 for a set of positive and negative pressures
- 7) record end-of-calibration marker

Calibration pressures were applied in ascending and descending order to check for hysteresis. None of significance was found. Maximum absolute value of the calibration pressure was limited to 105mm H₂O, the rating of the body transducer. The count levels set in 2) above were 250 for the wing, 300 for the freestream, and either 300 or 600 for the body.

2.3.3 Test Procedure Details of the test procedure were generally related to the efficient use of the data logger. The data were organized into blocks of 48 records, each record corresponding to a sample from each of the three data channels for a particular scanivalve position. As noted above, a data logger record actually comprised three scans of the transducer outputs taken in quick succession. This allowed an averaging of the data to be made during the subsequent data reduction. A galvanometer record, of course, comprised only a single reading of each channel.

The body scanivalve, with its greater number of taps, determined the blocklength. Thus, one block comprised the data taken at a particular roll angle, the complete body pressure map being obtained by placing the body tap meridian at various roll angles. Wing pressures were included in the first four blocks, each of these blocks containing data from one of the instrumented wing stations. The wing pressures were not

recorded for the remainder of the test. Freestream dynamic pressure was recorded on the data logger throughout the test.

Figure 8 depicts the position of the wing tap stations and the successive locations of the tap meridian. The roll angle spacing reflects the anticipated variation in the body pressures due to the wing. The flowfield was considered symmetric about a vertical plane through the body despite the slight geometrical non-symmetry of the configuration (this was experimentally verified). Thus, except for one test, pressure measurements were made only on the port side of the body, i.e. the same side as the instrumented wing stations.

Operator action during the course of a test consisted of maintaining freestream conditions, setting body roll angle and scanivalve tap position, and noting the galvanometer output. The procedure was as follows:

- 1) set tunnel freestream dynamic pressure at 50mm H₂O with reference to the pitot probe and Betz manometer
- 2) set body roll angle using transit and roll motor control, then record roll angle identifier
- 3) simultaneously step through the body and wing (when required) taps, recording at each position three scans on the data logger and noting the C_p values on the body and wing galvanometer displays
- 4) set both scanivalves to a tap vented to atmosphere and check logger zeros, resetting if necessary
- 5) repeat steps 1 through 4 as necessary
- 6) record end-of-test-data marker

Noting the local static temperature and pressure before and after the test completed the data set. Between tests, body and wing were covered with thick plastic sheet to protect the taps and model surface from contamination, particularly from oil seeping from the overhead balance.

It should be noted that the above procedure evolved as the testing progressed. In particular, resetting the logger zeros after each data block was begun only after large shifts appeared at about the middle of the test program. Prior to that, they had only been checked at the end of the test. A typical test required a total time of two to three hours, permitting a maximum of two tests per day.

2.4 Data Reduction

Figure 9 outlines the data reduction process. Because of the characteristics of the available inhouse computing facilities, it was necessary to separate the process into three distinct steps. In the first step, data were read from the magnetic tape cassette and stored on the MITRA 15 disk for input to the main data reduction computer program. Several operations were performed at this time: editing of data errors, averaging the three scans of each record, and calculation of calibration factors. These factors were provided in terms of the slope and intercept of a least-squares linear curve fitted to the calibration data.

Note that the operator exercised a degree of interactive control via a teletype terminal. The second step comprised the actual reduction of the data to the physical parameters of interest. After conversion of the data from counts to pressures, via the previously derived calibration factors, pressure coefficients were formed using an average value of the measured freestream dynamic pressure. For the galvanometer data, the pressure coefficient distributions were input directly on punched cards. Integration of the pressure distributions was carried out by evaluating the known integral of a quadratic function fitted in least-squares sense to groups of four adjacent data points, with the second and third points defining the sub-interval of integration. Such a "smoothing" procedure was chosen in order to give, in some sense, a best estimate of the integral of data known to be in error, i.e. to be within some uncertainty interval. Such intervals were determined within the program and used to judge the goodness of fit of the quadratics. If the variance of the curve fit exceeded the variance estimated for the data a warning was issued. The results of these integrations were body axial and spanwise normal force distributions and wing spanwise force and pitching moment distributions. The corresponding non-dimensional coefficients all used wing chord as the reference length, including those for the body.

The third step comprised the automatic plotting of selected results. Because of a lack of communication between the MITRA 15 and the PDP-11 which supported the plotter data to be plotted needed to be input from a keyboard. The data plots included in this report are machine plots.

2.5 Uncertainty Analysis

2.5.1 Methodology The foregoing analysis serves to determine two characteristics of the experimental data:

- 1) the magnitude of the uncertainty associated with the measurement process,
- 2) the probability that the difference between the measured and "true" values is less than or equal to this magnitude.

The result is a "confidence interval" which defines the range within which, to a specified probability, the true value is expected to lie. This probability defines the "level of confidence" of the uncertainty estimate. It is important to recognize that both items are required for a proper statement of the experimental uncertainty.

The determination of a confidence interval is relatively straightforward when the contributing variables can be considered random and normally distributed, i.e. have a Gaussian probability density function. Then, the theory of statistics provides methods for estimating uncertainties which are intimately tied to the level of confidence; the two characteristics are not independent. This feature makes a statistical approach particularly attractive. However, that the experimental data reported here mainly consists of so-called "single point" measurements precludes a direct application of statistics. Nevertheless, to capitalize on the rigor and consistency offered by the statistical approach, the uncertainty analysis adopted here utilizes general statistical ideas together with certain assumptions about the statistics of the test conditions and instrumentation. The principal assumption is that each of the many sources of uncertainty can be attributed to a variable which is

- 1) random
- 2) normally distributed
- 3) independent from the other variables

The consequence of such an assumption is that a variable, x , say, is completely described by its mean μ_x and variance σ_x^2 . The mean plus or minus the standard deviation σ_x defines an uncertainty interval with a confidence level of 67%; $\pm 2 \sigma_x$ gives 95.5%; $\pm 3 \sigma_x$ gives 99.7%.

Once each contributing variable has been assigned a variance, rules are available for determining the variance resulting from combinations of these variables. Consider two variables x and y satisfying the above assumption. The variance of their sum is

$$\sigma_{x+y}^2 = \sigma_x^2 + \sigma_y^2 \quad (1)$$

and of their product

$$\sigma_{xy}^2 = \sigma_x^2 \sigma_y^2 + \mu_x^2 \sigma_y^2 + \mu_y^2 \sigma_x^2 \quad (2)$$

Of course, the confidence level of the constituent terms determines the overall confidence level.

It is important to note that the derivations of (1) and (2) assume that the means and variances are known exactly. In reality only "best estimates" of these parameters are available. These are given by

$$\mu_x \simeq \bar{x} = \frac{\sum x_i}{N} \quad (\text{the sample mean}) \quad (3)$$

$$\sigma_x^2 \simeq s^2 = \frac{\sum (\bar{x} - x_i)^2}{N - 1} \quad (\text{the sample variance}) \quad (4)$$

Only in special cases is the confidence interval of the estimates themselves known. Thus, a further assumption is that these estimates are representative "enough".

In summary, the analysis procedure consists of the following steps:

- 1) identify sources of uncertainty in terms of the available variables
- 2) assign values of variance consistent with a chosen level of confidence
- 3) use combinations of Equations (1) and (2) to evaluate the variance of the final result

These steps are described in detail in the following sections. The sources of uncertainty are considered to fall into two categories:

1) test conditions, and 2) instrumentation. Lacking information to the contrary, it is assumed that manufacturers' specifications of equipment performance are for a confidence level over 95%. Hence all uncertainty intervals will be considered as $\pm 3s$ for consistency. Also, uncertainties are dealt with in absolute terms and not in the more common relative terms. This is because the specifications are only available as "percentage of full-scale value" and not the more useful "percentage of true value".

2.5.2 Test Condition Uncertainties Test condition uncertainties derive from three areas: 1) freestream, 2) local flow on the model, and 3) model geometry. The associated uncertainties discussed below are summarized in Table 2.

Previous flow quality surveys¹³ of the open jet, performed without a model, indicate the degree of uniformity in the freestream dynamic and static pressures. Within a radius of 1250mm from the tunnel axis and roughly in the plane of the wing support points, the dynamic pressure is within $\pm 1\%$ and the static pressure within $\pm .3\%$ of a reference value of dynamic pressure. As indicated in Figure 2, the model is always well within this region. Along the axis in the downstream direction there is an overall rise in dynamic pressure and fall in static pressure over the length of the test section. Dynamic pressure is within $\pm 1\%$ and static pressure within $\pm .5\%$ of a reference dynamic pressure for a region extending 500mm upstream and 1000mm downstream from this plane. The body is not completely contained within this region, with the nose extending a further 230mm upstream. However, this is not considered significant. Thus, $\pm 1\%$ of the freestream dynamic pressure represents the spatial variation of the dynamic pressure. However, there is no justification for the assumed randomness and normal distribution, whose meaning is not very clear within the present context.

Besides nonuniformity, there is a temporal variation in the freestream as well. This is estimated by applying (3) and (4) to pitot probe data obtained throughout the period of the test. It must be assumed that the results are representative of temporal variations at all points in the test section. The typical value of this temporal variance for all the tests so considered is about $.49\text{mm}^2\text{H}_2\text{O}$, which gives $\pm 2.1\text{mm H}_2\text{O}$ for the desired confidence interval. Applying a Chi-Square Test to data obtained from two different tests shows the hypothesis of a normal distribution function for the freestream dynamic pressure to be "not rejected" to a 5% significance level. This does not confirm that the dynamic pressure is so distributed, but does suggest that the computed temporal variance is representative of the spread in the data. Nevertheless, the results of a distribution-free test¹⁴ for trends shows that an hypothesis of "no-trend" should be rejected, indicating that the variations are not strictly random. This is not surprising, since the freestream dynamic pressure was observed to fall steadily with time.

The final value for the dynamic pressure uncertainty is obtained by combining the temporal and spatial contributions via (1).

With the presence of non-ideal freestream conditions, the local pressures on the model surface must also be considered uncertain. Although a statistical approach similar to that used for the freestream is impractical because of the large amounts of data required, it is not unreasonable to assume that the static pressure variation is in some way directly related to the freestream variation. Writing the Bernoulli equation as

$$P_l = P_\infty + Q_\infty - Q_l \quad (5)$$

and considering $P_\infty + Q_\infty$, i.e. the total pressure, to be constant throughout the flowfield, the corresponding variances are

$$S_{P_l}^2 = S_{Q_l}^2 \quad (6)$$

It is now necessary to relate the local dynamic pressure variance with that of the freestream. The actual physical mechanism involved here is a point of conjecture. The assumption made here is based upon results from incompressible potential flow theory: the velocities on the surface of the model are directly proportional to the freestream velocity. This implies that the ratio of local velocity at the surface, U_l , and freestream velocity, U_∞ , remains constant. Considering local and freestream velocities and freestream dynamic pressure, respectively, to be expressed by

$$\overline{U_l} + \Delta U_l \quad \overline{U_\infty} + \Delta U_\infty \quad \overline{Q_\infty} + \Delta Q_\infty \quad (7)$$

the assumption requires

$$\frac{\overline{U_l} + \Delta U_l}{\overline{U_\infty} + \Delta U_\infty} = \frac{\overline{U_l}}{\overline{U_\infty}} \quad (8)$$

Using the expressions in (7), the definition of dynamic pressure becomes

$$\overline{Q_l} + \Delta Q_l = \frac{1}{2} \rho (\overline{U_l} + \Delta U_l)^2 \quad (9)$$

Expanding (9) and retaining only first-order terms gives a relation between velocity and dynamic pressure variations like

$$\Delta U_i = \frac{\Delta Q_i}{\rho U_i} \quad (10)$$

Substitution of this relation into (8) gives

$$\Delta Q_l = \left(\frac{\overline{U_l}}{\overline{U_\infty}} \right)^2 \Delta Q_\infty \quad (11)$$

while the assumption leading to (8) implies that the consistent definition of pressure coefficient in this case is

$$C_p = 1 - \left(\frac{\overline{U_l}}{\overline{U_\infty}} \right)^2 \quad (12)$$

Substituting (12) into (11) and replacing the Δ 's with standard deviations gives, upon squaring,

$$S_{P_l}^2 = S_{Q_l}^2 = (1 - C_p)^2 S_{Q_\infty}^2 \quad (13)$$

which is the required relation between local and freestream pressure uncertainties.

Geometric uncertainties can be significant for the tests reported here due to the relative motion between the model elements and the necessity of rotating the body taps during the course of the test. The uncertainties for pitch angle represent the supposed reliability of the instrument used for the measurements. Yaw angle variations are attributed to minor differences between set screw settings from test to test. The quoted value represents the angular displacement caused by a 3mm error in the insertion length of one screw. In either case, wind-on deflections due to airloads were not evident. The body roll angle, or the angular location of the body tap meridian, was subject to both errors in initial setting due to system friction and to small but detectable shifts during the test. The quoted value represents an uncertainty in location of 4mm along the circumference of the body due to all causes.

Wing-body gap, being a principal variable, was given much attention during the set-up of each configuration. Accuracy and repeatability were aided by the use of cardboard strips sized to the desired gap

heights as a sort of feeler gauge. The longitudinal position of the wing with respect to the body was fixed for these tests, though the leading edge station varied slightly with wing pitch angle. Independent measurement showed an excellent agreement between the design-specified pressure tap locations and those of the finished model. The quoted value represents the typical tap diameter.

2.5.3 Instrumentation Uncertainties The uncertainty characteristics of the instruments used in the data acquisition system are summarized in Table 3. The values quoted for the transducers and data logger are taken directly from the manufacturers' specifications. That for the galvanometer is only representative of moving-coil, light spot instruments. In all cases the values are considered to represent hysteresis and non-linearity effects; zero-drift is not included. The "as used" values are the absolute uncertainties calculated from these specifications for the particular instruments used.

2.5.4 Pressure Coefficient Uncertainties With logger data, the pressure coefficients are formed from the ratio of two independently derived pressures such that

$$C_P \equiv \frac{P}{Q_\infty} \quad (14)$$

where P is the local gauge pressure and Q is the reference freestream dynamic pressure. Applying (2) gives, to first order,

$$S_{C_P}^2 = \frac{S_P^2}{Q_\infty^2} + \left[\frac{C_P}{Q_\infty} \right]^2 S_Q^2 \quad (15)$$

where the approximation

$$S_{(1/Q_\infty)}^2 = \frac{S_Q^2}{Q_\infty^4} \quad (16)$$

has been used in the second term.

Each measurement of P and Q_∞ is derived from the recorded data by

$$P, Q_\infty = A + BX \quad (17)$$

where X represents digital counts, B a scale factor, and A the "zero". Applying (1) and (2) successively gives the variance of the result as

$$S_P^2 = S_A^2 + \bar{B}^2 S_X^2 + \bar{X}^2 S_B^2 \quad (18)$$

The first term represents the contribution from zero drifting, a major problem with the data logger. Usually, the drift was monotonically increasing and positive, with the magnitude of the drift ranging from zero to 30 counts, depending on the particular test. Moreover, experience showed that the drift could not be assumed linear with time. Such a wide variation makes it difficult to quote a value representative of all the tests, though logger data with drifts of over 5 counts were rejected in favor of galvanometer data. The 3s value is taken to be one-half of the overall zero drift. Squaring this gives the required variance.

The second term represents two effects:

- 1) the uncertainty in the local pressure at the tap location
- 2) the uncertainty in the analogue-to-digital conversion.

The local pressure uncertainty itself is a combination of freestream and transducer uncertainties, which have already been described in 2.4.2 and 2.4.3, respectively. Collecting results from Tables 2 and 3 and using (1) gives

$$\bar{B}^2 S_X^2 = (1 - C_p)^2 (4.66)^2 + 4 \bar{B}^2 + \begin{cases} .28 & \text{for body} \\ 3.24 & \text{for wing} \end{cases} \quad (19)$$

With $\bar{B} = .167$ (maximum) for the body and .20 for the wing, the second term is the smallest, at less than .16, and thus will be considered negligible.

The third term represents the uncertainty in the scale factor associated with pretest calibration and drifting during the course of a test. The uncertainty interval for the slope of the least-squares curve fitted to the calibration data for each channel can be determined from statistics.¹⁴ The available calibrations exhibit a maximum 3s value of .00044 mm H₂O/count for any of the channels, corresponding to $\pm .5\%$. This is certainly negligible. For scale factor drift, experience suggests values of .0033 mm H₂O/count for the body and .004 for the wing, or about 2%. Upon replacing \bar{X} by $C_p Q_\infty / B$ the term becomes

$$\overline{X}^2 S_B^2 = \frac{C_P^2}{B^2} \begin{cases} .027 & \text{for body} \\ .040 & \text{for wing} \end{cases}$$

The final variance is then

$$S_P^2 = S_A^2 + 4.66(1 - C_P)^2 + \frac{C_P^2}{B^2} \begin{bmatrix} .027 \\ .040 \end{bmatrix} + \begin{bmatrix} .28 & \text{body} \\ 3.24 & \text{wing} \end{bmatrix} \quad (20)$$

Although S_Q^2 could be treated similarly, the availability of statistical results makes this unnecessary.

The fact that (15) and (20) depend on the C_P associated with an individual data point is inconvenient. Suitable "typical" C_P values are considered to be -.5 for the body and -2.0 for the wing. In each case, about 99% of the respective data sets is greater, i.e. less negative, than these values. The values of B used are .167mm H₂O/count for the body and .20 for the wing. Substitution of this information into (15) and (20) and taking S_Q^2 from Table 2 gives a resultant variance like

$$S_{C_P}^2 = 0.0025 S_A^2 + \begin{cases} 0.0048 & \text{body} \\ 0.025 & \text{wing} \end{cases} \quad (21)$$

If a zero drift of five counts is assumed, the relatively large contribution from the zero drift term becomes evident. Therefore (21) is best evaluated for each test individually.

2.5.5 Pressure Coefficient Uncertainty of Galvanometer Data The pressure coefficients displayed directly by the galvanometer are considered to be derived from an operation like

$$C_P = A + BP \quad (22)$$

resulting in a variance given by

$$S_{C_P}^2 = S_A^2 + \overline{B}^2 S_P^2 + \overline{P}^2 S_B^2 \quad (23)$$

As before, the first term represents the zero drift. In general, electrical and mechanical zeros were maintained to within one-half a division on the galvanometer display, corresponding to $\pm .01$ in C_P . Also included here is the basic accuracy of the instrument as given in Table 3, full scale of -3 giving a 3s value of .03 in C_P .

The second term represents uncertainties in the local pressure. The appropriate value of S_p^2 is given by the first and third terms of (19). Here, B represents a scale factor which is set during the calibration. It was always initially equal to the reciprocal of the target freestream pressure, i.e. $1/50\text{mm H}_2\text{O}$. The third term is the uncertainty in this scale factor. Since B is the reciprocal of the freestream dynamic pressure, the earlier evaluation of $S_{1/Q}^2$ is applicable. However, a second effect exists here because the logger data indicate that the actual mean dynamic pressure typically did not equal the target dynamic pressure, i.e. there is an uncertainty in the mean which defines the central point of the confidence interval expressed by S_B . If (16) is used to evaluate this contribution with a representative value of $S_Q = 1\text{mm H}_2\text{O}$, the result is $S_B = .0004/\text{mm H}_2\text{O}$. Assuming that the two effects can be combined via (1) gives $S_B^2 = 9 \times 10^{-7}$.

2.5.6 Integrated Coefficient Uncertainty To estimate the uncertainties in the integration of the pressure coefficient distributions, the following procedure is adopted. First, the standard deviation of the pressure coefficient is integrated over each subinterval of the domain of integration, just as the pressure coefficient itself is. This provides an estimate, though pessimistic, of the uncertainty associated with this "sub-integral". Second, if each such sub-integral is considered to be the standard deviation of a random, normally distributed, independent variable then the corresponding variances of all the sub-integrals can be combined via (1) to yield the standard deviation of the complete integral. From a statistical viewpoint, it is felt that the procedure is well founded. Moreover, it is consistent with the notion that the accuracy of numerical integration increases with decreasing sub-interval size. Nevertheless, an overly-conservative result is expected due to the convenient assumption of a constant value of S_{C_p} .

Applying the above procedure to the calculated body chordwise lift distribution

$$S_{B,C} = \cos \theta_B \sqrt{\sum_i \left[\frac{D}{C} \int_i^{i+1} S_{C_p} \cos \psi \, d\psi \right]^2}$$

or

$$S_{B,C} = \cos \theta_B \frac{D}{C} S_{C_p} \sqrt{\sum_i \left(\sin \psi \Big|_i^{i+1} \right)^2}$$

Similarly, for the body spanwise lift distribution

$$S_{B,S} = \cos \theta_B \cos \psi \frac{S_{CP}}{C} \sqrt{\sum_i (x |_{i+1})^2}$$

and the wing spanwise distribution

$$S_{W,L} = \cos \theta_W \frac{S_{CP}}{C} \sqrt{\sum_i (x |_{i+1})^2}$$

Finally, treating the wing spanwise pitching moment distribution

$$S_{W,M} = \frac{S_{CP}}{C^2} \sqrt{\sum_i \left(\frac{x^2}{2} |_{i+1} \right)^2}$$

Note that in each case the summation must be evaluated over the complete domain of integration. For the body chordwise lift distribution, this means from $\psi = 0^\circ$ to 180° , as discussed in 2.3.3.

3. EXPERIMENTAL RESULTS

3.1 General

A summary of the tests performed is provided in Table 4. In all there were 20 tests. Fifteen tests were concerned with pressure measurements, with one, 017, having a foam block to seal the wing-body gap. Five additional tests provided surface flow visualization for the detection of significant regions of separation. Again, one had the foam block in place. Wing pitch angle ranged from -9° to $+9^\circ$ and wing-body separation distance (surface-to-surface) from 'contact' to 80 mm. A high-wing configuration was represented by the wing at a positive angle; a low-wing configuration by a negative angle. Body pitch angle remained at 0° .

The uncertainty intervals come directly from the analysis of Section 2. While the logger and the galvanometer uncertainties are, at times, quite different for the pressure coefficient, those for the integrated coefficient are essentially the same, a result of neglecting the zero shifts. For the tests where both logger and galvanometer data were available the more reliable data is quoted. In general the logger data was used whenever possible because of its better sensitivity, even if the calculated uncertainty interval might be slightly larger. Since the integrated results are of primary interest here, this poses no real penalty.

The performance of the curve fitting for the numerical integration described in Section 2.4 is demonstrated in Figure 10. The data chosen are for a wing station at 9° pitch angle, whose sharp pressure peaks, especially on the suction side, present the most demanding fitting task. The fitted curve shown is constructed of least-squares parabolas placed between each pair of adjacent data points; consequently the curve is not continuous from one segment to the next. Overall the curve behaves well. The smoothing offered by the least squares approach is most evident on the suction side between .5c and .8c. At the pressure peaks, however, the fit is subject to spiking, due to the large changes of curvature required of

the low order polynomial. This behavior is typical of the wing chordwise integration. It is detected by the computer program as a failure of the curve fit variance to be less than the variance of the experimental data. The present example gave three such failures. On occasion the same problem arises with the integrations for the body chordwise force distribution, but are almost never found for integration for the body spanwise distribution. Though aesthetically undesirable, the effect of the spikes on the integration is negligible. Comparison of the present calculation with values obtained by using a polar planimeter show good agreement. Interestingly multiple trials showed the planimeter results to be no more certain than the numerical results.

Another feature of the wing chordwise integration is the behavior at the trailing edge. With no data available, the fictitious but typical value of $C_p=0$ is assigned to the trailing edge to define the interval of integration. However, it is apparent that the fitting procedure does not necessarily pass the curve through the point. Regardless of what the trailing edge pressure is, the contribution of this region to the integral is small and the value of the integral is not critically dependent on the trailing edge C_p .

3.2 Repeatability and Symmetry

Logger and galvanometer results were compared to determine the degree of interchangeability of the two data sets and give an indication of repeatability. Figure 11 shows body pressure distributions along the $\psi=180^\circ$ meridian obtained from the two acquisition systems. The agreement is good, with both data sets being included in the uncertainty interval. That the galvanometer data lies consistently above the logger data probably indicates a zero shift. Integrations of the data (along with distributions at $\psi=0^\circ$, not shown) gives the quoted nominal force coefficients. The difference is larger than desirable, being just on the edge of the uncertainty interval, which implies that these intervals are not overly conservative.

A similar comparison of wing pressures is shown in Figure 11. Again the galvanometer data tend to be above the logger data, especially on the suction side. This difference is reflected in the lift coefficients and is contained within the confidence interval.

Referring to the Remarks of Table 4, Tests 007 and 011, both high-wing, $\theta_w=9^\circ$ configurations, displayed a large degree of unsteadiness of pressures on the suction side near the leading edge. At the time the galvanometer output indicated variations of up to ± 1 in C_p . Nevertheless, comparison of logger and galvanometer data for the $y/s = .094$ wing of Test 007, Figure 12 shows generally good agreement, except for very near the leading edge. The resulting C_l 's show some difference but are comparable. This is an indication that the averaging of the multiple logger readings and the operators' estimate of the galvanometer output are comparable. Though not considered in Section 2.4 the unsteadiness is generally contained within the quoted confidence intervals.

To determine the effect of the geometric asymmetry of the model configuration on the symmetry of the flow local to the wing-body gap, body chordwise pressures were measured along meridians symmetrically disposed about a vertical plane through the body axis. Distributions along the $\psi = 190^\circ$, 170° meridians are shown in Figure 13. These include regions of the body very close to the wing. No significant difference in the pressure distribution is evident, nor for measurements (not shown) along the $\psi = -10^\circ$ and $+10^\circ$ meridians. Besides verifying the flow symmetry, these results show that the body roll positioning methodology is acceptable.

3.3 Body-Wing Pressure Distributions

Figures 14 and 15 depict typical body chordwise pressure distributions for high-wing and low-wing cases, respectively, with the wing at 3° and a gap of about .44. Each plot shows the distributions for the two meridians in the same vertical plane. Hence, the area between the two curves is directly proportional to the normal force coefficient at a corresponding spanwise station on the body. It is evident that the resulting integral for the high-wing is, effectively, the difference between the two large values, making accurate calculation difficult. No such problem exists for the low-wing case.

Several common features are evident. The wing-induced pressures are confined to that half of the body facing the wing. For the present axial position of the wing, pressures on the nose and afterbody are hardly affected by the wing. Regardless of configuration, some positive pressure rise occurs upstream of the wing leading edge.

When the wing and body in the high-wing case are nearly touching, noticeable changes occur in the pressure distributions. For the 3° case, Figure 16 shows a much modified suction peak. At $\psi=180^\circ$ the peak is flattened. Since, at 3° the wing lower surface aft of midchord is nearly parallel to the body surface, this constant pressure region may reflect a constant area duct-type flow. The behavior is very localized and at $\psi = 150^\circ$ a more complicated situation exists. By $\psi = 120^\circ$ the position of Figure 14 returns.

At 9° , Figure 17, the suction peak disappears completely. At $\psi = 180^\circ$ a second, sharper pressure peak appears at the trailing edge. The duct analogy fails here, however, since such reasoning would predict a high suction at the trailing edge due to the minimum wing-body clearance (1 mm) at this location. Again, the behavior is highly localized and disappears at least by $\psi = 150^\circ$. Dominating the situation is the large pressure associated with the pressure-side leading edge region of a lifting aerofoil. Unlike the 3° case, these pressures are impressed about the entire circumference of the midbody.

The wing pressure distribution for these minimum gap cases are given in Figures 18 and 19 for 3° and 9° angle, respectively. At 3° , the pressure-side distributions are noticeably distorted, as shown by comparing the data for $y/s = .169$ with those further inboard. The abrupt behavior about $.3c$ is due to the fact that $.3c$ being the maximum thickness location for the RAE 101 section, is nearly the point of minimum wing body clearance. At the trailing edge there is a significant difference between the suction and pressure side distributions.

Interestingly this effect is most evident at the intermediate wing stations. Comparison of Figures 20 and 22 shows, in fact, that the distribution at $y/s = .064$ on the wing is similar to the body distribution at $\psi = 150^\circ$, also at $y/s = .064$. This is shown explicitly in Figure 20. A similar comparison shows that the flatness of the suction peak at $\psi = 180^\circ$ ($y/s = 0$) is reflected even in the (relatively distant) wing distribution at $y/s = .019$.

The wing pressure distributions at 9° are much less affected, with a trailing edge pressure distortion evident for the $y/s = .019$ station only. This is not unexpected since here less of the wing is actually close

to the body than in the 3° case. One interesting trend here is that the suction peak increases with y/s , indicating that the local effective incidence and/or section camber are/is also increasing. Surprisingly, examination of the 3° data shows just the opposite trend. However, the location of the peak is less defined in this case, so that the measured values may not adequately indicate the peak values.

3.4 Body and Wing Loading Distributions

Chordwise normal force distributions calculated from the measured body pressures are given in Figures 21 through 24 for varying gap height. These force distributions are very similar in shape to the $\psi = 180^\circ$ pressure distributions from which they are derived. Figures 25 and 26 show the high-wing results for 3° and 9° pitch angle, respectively. As expected, the force levels increase as gap is decreased. However, the "relaxation" rate of the induced forces increases with decreasing gap, with the forces never being of significance beyond $.7c$ upstream or downstream of the wing. The most striking feature is the presence of points within the region of major influence at which the various distributions intersect. For 3° these are located at $-.25c$, $.25c$, and $.9c$, with the curve for minimum-gap slightly missing the second and completely missing the third. For 9° two such points are evident, at $-.25c$ and $.5c$. At either angle the locations of pressure peaks are generally insensitive to gap height, although the leading edge peak at 3° moves slowly downstream with decreasing gap. The peak magnitudes themselves appear to vary nearly linearly with the geometric-like change in the gap.

Similar characteristics can be identified in the low-wing distributions of Figure 23 and 24. Note that the data is corrected for the fact that this configuration is actually tested inverted. Here, the intersection points are in the vicinity of $.1c$ and $.7c$ for both wing angles. These data also confirm that the small loading peak near the trailing edge station disappears at the higher wing angles, a feature evident in the earlier high-wing data.

The effect of wing pitch angle with a constant gap height is shown in Figure 25 for the low-wing configuration. Note that the magnitude of the induced loading is much greater for positive angles. Interestingly, the 0° (nominally non-lifting) case induces an adverse loading on the body, i.e. negative lift. An overall neutral body loading is realized

for the -3° case. The negative angle data (which are actually from the high-wing at positive angles) has little practical significance for wing-body combinations, but has some relevance for the tail-body, especially if the tail is all-moving. Note that inverting the curves and reversing the signs of the angles gives results applicable to the high-wing configuration.

The results most pertinent to the present investigation are the spanwise load distributions on the body and wing. Figure 26 shows body distributions for the high-wing case at both 3° and 9° . For either angle there are indications that the loading increases with decreasing gap, as expected, but the close grouping of the data makes this a tenuous conclusion. At any rate, the dependence on gap is small, generally within the uncertainty bounds of the data. The loading magnitudes are greater for the higher angle, but in either case they drop monotonically toward the zero loading expected at the body edge.

The 3° , minimum gap case is a noticeable exception to the above observations. Both the centerline load magnitude and the overall load gradients are about double those of the rest of the data. The distribution seems no longer to be monotonic, but rather displays a maximum near $y/s = .064$, with the subsequent convergence to the zero loading expected at the body edge not being very obvious. An explanation of the behavior can be found in the pressure distribution of Figure 20. Moving outboard from the centerline sees the pressure magnitude decrease while the suction increases. At or near $y/s = .064$ ($\psi = 150^\circ, 30^\circ$) the net loading becomes zero or even positive. Continuing outboard, the pressure dominates again, moving the loading negative, from which point it finally approaches zero. While this explains the trend of the present data, the computed magnitudes of the loading at $y/s = .064$ and outboard must be suspect because of the problem noted in 3.3. Integrating the appropriate pressure distribution of Figure 14 with a polar planimeter gives a result much closer to zero than that calculated. This is indicated in the figure. The advantages of dealing with large net magnitudes is certainly apparent in the 9° data.

Figure 27 shows the body spanwise force distribution for the low-wing configuration. For the same pitch angles, the magnitudes are greater than for the high-wing, but they are still negative. Thus, the

lift induced on the body is negative regardless of the configuration. The 9° data show the magnitude increase with decreasing gap, and a much greater dependence on gap than the high wing case, especially near the centerline. As before, the 3° data are more tightly grouped and evidence no consistent dependence on gap, though one might be supposed to exist. The behavior of the inboard data is particularly confused. Indications that the lift is not monotonic are suspect, based on physical grounds, although inspection shows that they accurately reflect the pressure distribution behavior. The appropriate galvanometer-derived pressure distributions do not indicate such a trend but instead give force coefficients at the two inboard stations which are about the same, at least for the larger gaps. As a point of comparison, such results for the small gap are included in the figure. The two data sets differ noticeably near the centerline but agree very well in their outboard trend. Note that the difference in the centerline data is not contained within the uncertainty interval.

The wing spanwise loading distributions for the high-wing configurations are given in Figure 28. Unfortunately, the results are particularly confused. For 3° , the identification of a dependence of loading on gap is hindered by the completely different magnitude of the intermediate gap data. The discussion of 2.5 suggests an undetected error in the scale factor to explain the behavior (these data are from the galvanometer) except that the required size of the error would seem to make this improbable. A comparison of the various pressure distributions taken at the outboard station, given in Figure 29, does indeed show an unsystematic difference in the intermediate gap data. The unique behavior of the minimum gap data is readily explained by the discussion of the associated pressure profiles given in 3.3. The result of modifying the trailing edge pressures to give a more typical distribution are included in the figure as a point of interest.

For 9° , much of the data is compromised due to the effects of flow unsteadiness. The unsteadiness was observed during the testing and is probably accompanied by significant flow separation. The small gap data, which were observed to be steady, show a smooth, monotonic decrease in lift with increasing y/s . The distributions for the larger gaps are very erratic, with particularly large departures at $y/s=.094$. The pressure distribution at this station, shown in Figure 30 along with that of the

outboard station, is quite distorted, especially on the suction side between .2c and .5c. Both logger and galvanometer data display this behavior.

The wing load distributions for the low-wing are shown in Figure 31. Here, the data is better behaved, with a clear dependence on gap. Overall, the loading decreases with increasing y/s . The interesting feature is the crossover of the small and intermediate gap curves which can be found for both wing angles.

The lift curve of each of the four wing stations is given in Figure 32 for the high-wing configuration at constant gap ($h/c=.51$). As expected, the lift curve slope decreases with increasing pitch angle, and the lift magnitude decreases with increasing y/s . Note that the trend in lift at 0° is opposite that at 9° , suggesting that the curve rotates about some point as y/s increases. In view of the estimated uncertainty interval, however, the significance of the ordering of the data at 0° is questionable.

Distribution of pitching moment about the wing quarter-chord is given in Figure 33 for all the configurations tested. Besides being an indicator of static stability, the pitching moment gives a rough idea of the nature of the chordwise pressure distribution relative to an undisturbed distribution, i.e. for a wing-alone situation. For the high-wing, the moment decreases with increasing pitch angle. Surprisingly, this trend is reversed for the low-wing case. Data for the low-wing at 9° and high-wing at 3° show that the moment increases with decreasing gap and decreases with increasing y/s . There is good convergence toward a common value at the outboard station for the different distributions. Trends opposite to both of those mentioned above are exhibited by the low-wing, 3° , and high-wing, 9° , data, though the significance of any trend could be questioned in view of the relatively large data uncertainty here.

3.5 Flow Visualization

Surface oil flow visualization indicated no appreciable separation on the body for the high-wing configurations. However only the considered critical case-- 9° , minimum gap--was studied. The absence of separation here was considered applicable to the cases with lower angle and larger

gap. The unsteadiness reported in 3.4 is not thought to appreciably affect the body flow, since it is confined to the upper surface of the wing and, hence, would be "shielded" from the body. For the low-wing, separation-like features were observed for the small and intermediate gaps at 9° . Photographs of the resulting oil flows are presented in Figure 34. Note that the body has been rotated 180° away from the wing for the purpose of photography. The white disks mark the location of the wing leading and trailing edges during the test. Taking the surface streaklines as streamlines, the lines first diverge at the leading edge due to the pressure there, then begin to converge with the development of suction farther downstream. At .5c for the small gap, there begins a region of seemingly undisturbed oil bounded by a line of accumulated oil. These features are taken to denote a region of separated flow. For the intermediate gap, there is a similar accumulation line beginning near the trailing edge. However, it is less distinct than that of the previous case and the "separated" region shows more evidence of oil movement.

3.6 Wing-Body with Sealed Gap

The sealed-gap configuration requires some differences in data reduction and interpretation from the previous cases. Figure 35 shows the normal force distribution for the body. Here, however, the portion of the wing spanned by the foam block is considered part of the body. The upper surface wing pressures in this region are thus substituted for the now-meaningless body pressures. Because the spanwise tap stations for the wing and body do not match, linear interpolations of the wing data have been made in order to conform to the body tap locations. Also, there are no wing data on the configuration centerline and, therefore, some extrapolation has been required. The adopted procedure fits a parabola to the pressure value and the estimated spanwise gradient at $y/s=.019$ while requiring zero gradient at the centerline. Aside from being continuous and meeting the requirements for symmetry, the method has no physical basis and can only be considered an expedient. Therefore, the force magnitudes of Figure 36 between the wing leading and trailing edges are in error by some unknown amount. The trend is considered unaffected. The negative peaks just before and after the wing mark the stagnation points and separation associated with the bluff faces of the foam block. These separation regions are revealed by the oil flow visualization in Figure 36.

Figure 37 depicts the spanwise lift distribution for the wing and

body. Note that the two are identical inboard because of the presence of the foam block. Outboard, the coefficients remain directly comparable, since wing chord is the non-dimensionalizing length for all the data. The convergence of wing and body lift and wing alone lift is very good. The pressure distribution for the body stations outboard of the foam have a shape like that shown in Figure 14. Thus, as shown, the resultant force is near zero. The effect of gap and sealed gap on the wing suction-side pressure distribution is shown in Figure 38 for $y/s=.019$, i.e. the most inboard station. The leading edge suction increases with decreasing gap until $h/c=.45$, after which little or no change is evident. Sealing the gap, however, causes a further large increase in suction, even though the "gap" here is actually larger than the minimum gap for the unsealed gap cases.

4. SUMMARY REMARKS

4.1 Discussion

Direct comparison of logger and galvanometer data gives a good degree of confidence in the repeatability of the measured pressures. Certainly the biggest problem with the data acquisition centered on the logger zero drift. Dealing with the drift was difficult owing to its large change in magnitude and occasional change in sense from test to test. However, the fact that tests performed in the morning tended to experience the largest drift and the results of some nighttime monitoring of the drift suggest

the most likely cause to be temperature changes. The transducers are considered the most likely source since they are immersed in a flow which experiences larger than ambient temperature variations. If so, calculations indicate that the transducer's temperature sensitivity to be at least four times greater than the manufacturer's specification. The problem remains unresolved. Only frequent monitoring and adjustment seems practical for minimizing such drifting. Certainly a contributing factor to the drifting was the excessive length of time required for each test.

The results of the uncertainty analysis appear verified by the test data behavior. Although the logger offers more sensitivity than the galvanometer, the aggregate uncertainties are roughly the same. The difference depended mainly on the logger zero shift. The freestream temporal variation is also a dominant factor. Thus, frequent adjustment here is beneficial.

The pressure distributions on the body are well behaved and demonstrate clear trends with gap. Notable is the similarity of wing and body pressure distributions which are located in the same vertical plane, i.e. a plane parallel to the assumed plane of symmetry of the flow. This indicates that the vertical pressure gradients are small in the region between the sting and body, even for relatively large gaps. In light of this behavior, it may have been expected that the wing wake would also impress a pressure on the body. The high-wing, small gap, 9° case would

seem a strong candidate for such an interaction. As reported by Preston and Sweeting⁶ for a Joukowski aerofoil, a characteristic of the wake is a peak in the static pressure immediately downstream of the wing trailing edge, about .005c, after which the pressure falls monotonically to the freestream value. No such behavior was observed for the body pressures in the vicinity of the wing trailing edge. However, assuming that these referenced findings are even applicable to a non-cusped aerofoil, it is questionable whether the means existed to resolve such a localized feature. The effect of the near-wake remains unknown.

A notable feature of the minimum gap, high-wing cases is the significant difference between upper and lower surface pressures near the wing trailing edge. Whether this constitutes a true breakdown of the Kutta-condition can not be answered with the available data. However, it would be an apparent breakdown for those potential flow modeling methods which enforce the Kutta-condition on the wing surface upstream of the trailing edge and not, say, in the wake. This appears to be a problem only for the separate wing and body; with the gap sealed there is no significant pressure difference near the trailing edge for the stations located outboard of the foam block.

The integrated results are of major interest but, unfortunately, give a spotty performance. The chordwise normal force distributions are quite good; trends in gap are unmistakable. The body experiences a net negative lift regardless of wing location, gap distance, or (positive) pitch angle. For the spanwise distributions the situation is less favorable. Coefficients derived from both logger and galvanometer data display "scatter" that is only just within the prescribed confidence interval. The overall behavior is as expected: The magnitude of the loading decreases with increasing y/s for both the wing and the body. For the body, the variation appears linear over much of the span. The distributions tend to flatten near the centerline because of the local symmetry of the configuration, but this is not always consistent and there are some (doubtful) indications that the changes in this region are not monotonic. A low-wing gives higher loading at 3° pitch than a high-wing. At 9° the two are nearly the same. The distributions for the wings are typically non-linear in appearance, and concave upward, but there are exceptions. The inflection point needed for zero slope at the centerline is not evident with the little data that is available. The very strange behavior of

some wing data , while identified as a result of flow unsteadiness, makes the recognition of trends that much more difficult.

The dependence of the body spanwise lift distribution on gap height is small at 3° , being well within the uncertainty interval. This obviates any direct identification of a trend while making the inconsistent pattern of the curves a bit more acceptable. This small dependence is due to the fact that while the induced pressures increase in magnitude with decreasing gap, their chordwise relaxation also increases. The net result is that the integrations taken over a chordwise interval to find the local force coefficient for the spanwise distribution are little different with different gap. At 9° the gap dependence is more apparent but usually only over the inboard half of the body span. For the wing, the monotonic gap dependence is evident at the inboard station but can become uncertain farther outboard.

The results at minimum gap and the sealed gap reinforce the findings of Jacob and Ward²: the wing may almost touch the fuselage (say, a clearance of .02c) before interference effects become large. This is especially true of the body spanwise loading in the present tests. However, in this reference much emphasis is placed on drag as the principal interference phenomenon. This was not measured directly here, but insofar as this drag is usually associated with flow separation, the flow visualization results offer one point of comparison: that low-wing combinations alone exhibited large flow separation is a feature determined from balance measurements by Jacob and Ward and noted by Hoak³ for both the separate wing and body and integral wing-body combinations. In the former work, high wing drag was also found for $h/c=.4$ for a high-wing of symmetrical section near a circular section fuselage. Wing flow unsteadiness during the present tests was detected at $h/c=.52$. No separation was detected for the low-wing at this gap setting, though it has been found in the other studies.

The increase in the local lift curve slope with decreasing y/s found for the high-wing may be best explained as a change in the effective downwash of the wing due to the presence of the body. In this sense the body acts as would a ground plane on the inboard portion of the wing: blocking the normal development of wing downwash and, hence, increasing the effective angle of incidence and lift of the adjacent wing. This

effect would, of course, decrease with distance from the body. Thus, at any positive pitch angle, a section near the body would tend to develop more lift than one farther outboard, resulting in an apparent increase in the section lift curve slope.

The differences in the trend of pitching moment versus pitch angle found between the high-wing and low-wing can be ascribed to a difference in the chordwise location and extent of the region of minimum physical separation of the wing and body. For the high-wing, this region is on the pressure side, behind the section's maximum thickness point. At 3° , a large portion of the aft part of the aerofoil is parallel to the body surface, while at 9° the minimum is located right at the trailing edge. The region of minimum flow area is always associated with a high suction (the venturi effect), explaining the positive sense of the pitching moments. For the high-wing, the low suction present over a large area at 3° gives a larger moment than does the high suction concentrated near the trailing edge at 9° . For the low-wing, the minimum flow area is near the section maximum thickness station and moves forward with increasing positive pitch angle. The combination of high suction and longer moment arm leads directly to the observed trend of increasing moment with increasing pitch angle.

The results of the oil flow studies seem significant at least for the small gap case. However, such oil flows must be interpreted with caution because of the unavoidable flow along the body circumference due to gravity. Thus, there may be an appreciable difference between the apparent and real spanwise extent of the separation region. The lack of any indication of flow within the region is puzzling. Of course, the flow velocities and resultant surface shear stresses may well be simply too low to move the oil.

Especially significant are the results for the sealed-gap case. The body chordwise normal force distribution ahead of the wing is very similar to that found for the minimum gap, even to the magnitude of the maximum download found near the leading edge. The contribution of the relatively high suction on the wing's upper surface dominates the distribution. Indications are that this suction is increased by the introduction of the foam block over that which would exist without it. The spanwise lift distribution shows that the lift increases from wing root to the centerline

of the configuration. This result appears to be in direct contradiction with the calculations of Gregoriou¹⁵ and some general comments made by Ashley¹⁶: the body lift on a wing-body combination is a maximum near the root and decreases over the body. However, it is thought that this description is only appropriate for configurations which exhibit a significant increase in the local effective wing incidence due to the acceleration of the induced crossflow over the body circumference. This will occur for configurations having mid or shoulder-mounted wings. The mechanism is apparently unimportant for the high-wing studied here. The small lift at the body stations outboard of the foam block indicates that the effect of the block itself is localized with respect to the lift on the body, unlike the situation with the wing. The fact that the body pressure distributions in this area are much like those of the unsealed gap support this contention.

4.2 Conclusions

Based on the presented data and discussion, the following conclusions may be drawn:

- 1) The performance of the model was acceptable. In particular, no significant flow asymmetry is evident despite the geometric asymmetry of the model.

- 2) Body chordwise normal force distributions display increasing magnitudes but decreasing level of chordwise influence with decreasing gap. Magnitudes of body loading are greater for the low-wing configuration. For the separate wing and body the net induced lift on the body is negative.

- 3) The body spanwise lift distribution is monotonic, starting from a negative value at the centerline and increasing to zero at the maximum body span. The distribution appears to vary linearly with spanwise station over most of the body span, with the slope decreasing near the centerline, as would be expected of a smooth, symmetric distribution. The magnitudes increase with decreasing gap. The dependence on gap is most pronounced along the inner half of the body span.

- 4) The low-wing spanwise lift distribution decreases monotonically with increasing spanwise station, and magnitudes increase with decreasing gap. For the spanwise region investigated, the slope of the distribution increases inboard, suggesting an inflection point and large curvature of the distribution near the centerline. The high-wing spanwise distributions are much affected by flow unsteadiness, making the data irregular

and inconclusive.

5) In cases where the wing trailing edge is nearly touching the body, the wing pressure distribution is significantly distorted in the trailing edge region. This can lead to problems in accurate potential flow modeling if the Kutta-condition is enforced on the wing surface within this region.

6) Pressure gradients in the vertical direction between the wing and body tend to be small, so that pressures on facing regions of the wing and body are similar.

7) The pressures induced on the body by the wing appear confined, for the most part, to that portion of the body directly facing the wing.

8) Separation and unsteadiness are present with some configurations, and are not necessarily associated only with the small gap configurations.

9.) The wing spanwise pitching moment distribution for the separate wing and body decreases monotonically with increasing wing station, and is almost always positive.

10) The wing section lift curve slope increases with decreasing spanwise station. This is probably due to a reduction in downwash caused by the body.

11) The spanwise lift distribution for the sealed gap configuration shows the lift to increase from wing root to centerline. This behavior suggests that the dominant mechanism for induced loads is the change in local flow velocities due to the wing circulation (for a high-wing configuration).

4.3 Recommendations

The following recommendations are offered in support of future experimentation:

1) The data acquisition should be automated as much as possible to reduce operator-induced error and the period required for each test. This could be done with as little as a clock circuit with electrical trigger to sequence the operation of the scanivalve and data logger.

2) Further studies should be made for surface-to-surface gap heights of between 20mm and contact.

3) An intermediate angle of pitch, say, 6° , should be used to verify the trends with pitch angle reported here.

4) The sealed gap situation should be further studied, with rigid, non-porous contoured blocks used in place of the expanded foam of the present study.

LIST OF REFERENCES

1. GREGORIOU G. : The consideration of wing-body and wing tail interference in missile designs, lecture series on Missile Aerodynamics, the von Karman Institute for Fluid Dynamics, Belgium, 12-16 March 1979.
2. JACOBS E.N. and WARD K. : Interference of wing and fuselage from tests of 209 combinations in the NACA variable density tunnel, Report N° 540, National Advisory Committee for Aeronautics, Washington, 1935.
3. HOAK D.E. et al : USAF stability and control DATCOM, Flight Control Division, Air Force Flight Dynamics Lab., Wright-Patterson Air Force Base, Dayton, Ohio, USA, July 1963.
4. HESS J.L. and SMITH A.M.O. : Calculation of potential flow about arbitrary bodies", in Progress in Aeronautical Sciences, Vol.8, pp.1-138, Pergamon Press, Oxford, England 1967.
5. HUNT B. : The panel method for subsonic aerodynamic flows, A survey of mathematical formulations and numerical models and an outline of the new British aerospace scheme, von Karman Institute for Fluid Dynamics, Belgium, Lecture Series 1978-4, March 1978.
6. PRESTON J.W. and SWEETING N.E. : The experimental determination of the boundary layer wake characteristics of a simple Joukowski airfoil with particular reference to the trailing edge region. Aeronautical research council R and M N° 1998, March 1943.
7. MANGLER K.W. and SMITH J. : Behavior of the vortex sheet at the trailing edge of a lifting wing, RAE TR 69049, March 1969.
8. GUALDONI F. : Aerodynamic characteristics of a sweptback wing in sideslip, von Karman Institute for Fluid Dynamics, Project Report 1977-8, June 1977.

9. MEINEKE G. : A wake survey behind a sweptback wing, PR 1978-14, the von Karman Institute for Fluid Dynamics, Belgium, June 1978.
10. REPETTI G. : Wing pressure distribution of a straight wing-body in sideslip, PR 1979-2, the von Karman Institute for Fluid Dynamics, Belgium, June 1979.
11. TENLING B.E. and ALLEN C.Q. : An investigation of normal force and vortex wake characteristics of an ogive-cylinder body at subsonic speeds, NASA TN D-1297 April (1962).
12. DURAND W. ed.: Aerodynamic theory, Volume VI, Springer, 1936, Germany.
13. _____ : Rapport sur les mesures faites au tunnel soussonique à Rhode-Saint-Genèse, Ko-50-71, von Karman Institute/Escher-Wyss, 1950.
14. KREYSZIG E. : Advanced engineering mathematics, John Wiley and Son, New York.
15. GREGORIOU G. : On the calculation of the pressure distribution of wing-body combinations in the non-linear angle of attack range; in "Prediction of Aerodynamic Loading, AGARD-CP-204, Feb. 1977.
16. ASHLEY H. and LANDAHL M. : Aerodynamics of wings and bodies, Reading, Mass. Addison-Wesley, 1965.

TABLE 1

MODEL GEOMETRY SPECIFICATION

Body:

Type:	Ellipsoid Cylinder
Nose Fineness Ratio:	1.5
Overall Length:	1300 mm
Diameter:	200 mm
Nose Length:	300 mm

Wing:

Type:	Straight, Untwisted
Profile:	RAE 101, Symmetrical, $t/c = .09$
Chord:	300 mm
Actual Semi-Span:	900 mm .
Tested Semi-Span:	780 mm
Actual Aspect Ratio:	6.0
Tested Aspect Ratio:	5.2

Configuration:

Nominal Leading Edge	
Station:	700 mm from Nose of Body
Tested Wing Span/Body	
Diameter:	7.8

TABLE 2

TEST CONDITION UNCERTAINTIES

Item:	3 Standard Deviation
Freestream:	
Q_{∞} Spatial:	.5 mm H ₂ O (= .01 Q_{∞})
Q_{∞} Temporal:	2.1 mm H ₂ O
Q_{∞} Total:	2.1 mm H ₂ O
P:	2.1(1-C _p) mm H ₂ O
Geometric:	
Gap Distance:	2 mm
L. E. Station:	2 mm
Tap Station:	1 mm
Pitch Angle:	.5°
Yaw Angle:	2°
Roll Angle:	2°

TABLE 3

INSTRUMENTATION UNCERTAINTIES

Item	Given Accuracy (F.S.V.)	Used Accuracy 99% Confid.
Galvanometer	1% (See Text)	.03 in C_p
Statham		
Transducers:		
Body (105 mm H_2O)	.5%	.525 mm H_2O
Wing (350 mm H_2O)	.5%	1.75 mm H_2O
Data Logger	.2% \pm 1 count	2 counts

TABLE 4

SUMMARY OF TESTS PERFORMED

Test	Wing	O_w (%)	h/c	Data Source: Body	Wing	$S_{C_p, B}$	$S_{C_p, W}$	Remarks
002	low	3	.446	L/G	L/G	.05/.03	.06/.06	
003 004	low	9	.436	L	L	.07	.08	
005	high	9	.451	G	L	.03	.08	
006	high	3	.446	G	L	.03	.07	
007	high	9	.518	L	L	.04	.07	unsteady wing pressures
008	low	9	.503	G	G	.03	.06	
009	low	3	.508	L	L	.03	.05	
010	high	3	.513	G	G	.03	.06	very large logger zero drift
011	high	9	.651	L	L	.04	.09	unsteady wing pressures
012	low	9	.636	L	L	.07	.08	
013	low	3	.641	L	L	.04	.06	
014	high	3	.646	G	G	.03	.06	logger failed
015	N/A	0	.444	G	G	.03	.06	logger failed
016	high	3	.389	G	G	.03	.06	logger failed
017	high	3	.400	L	L	.05	.05	gap sealed with foam block
018	high	9	.451					oil flow study
019	low	9	.436					oil flow study
020	low	3	.446					oil flow study
021	low	9	.503					oil flow study
022	high	3	.400					oil flow study

TABLE 4 (CONTINUED)

SUMMARY OF TESTS PERFORMED

Nominal Test Conditions:

$$V = 28.5 \text{ m/s}$$

$$Re = 1.86 \times 10^6 / m$$

$$Re_c = .56 \times 10^6$$

Nominal 1 s Uncertainties for Body-Force Coefficients:

$$\text{Body: } .01$$

$$\text{Wing: } .02$$

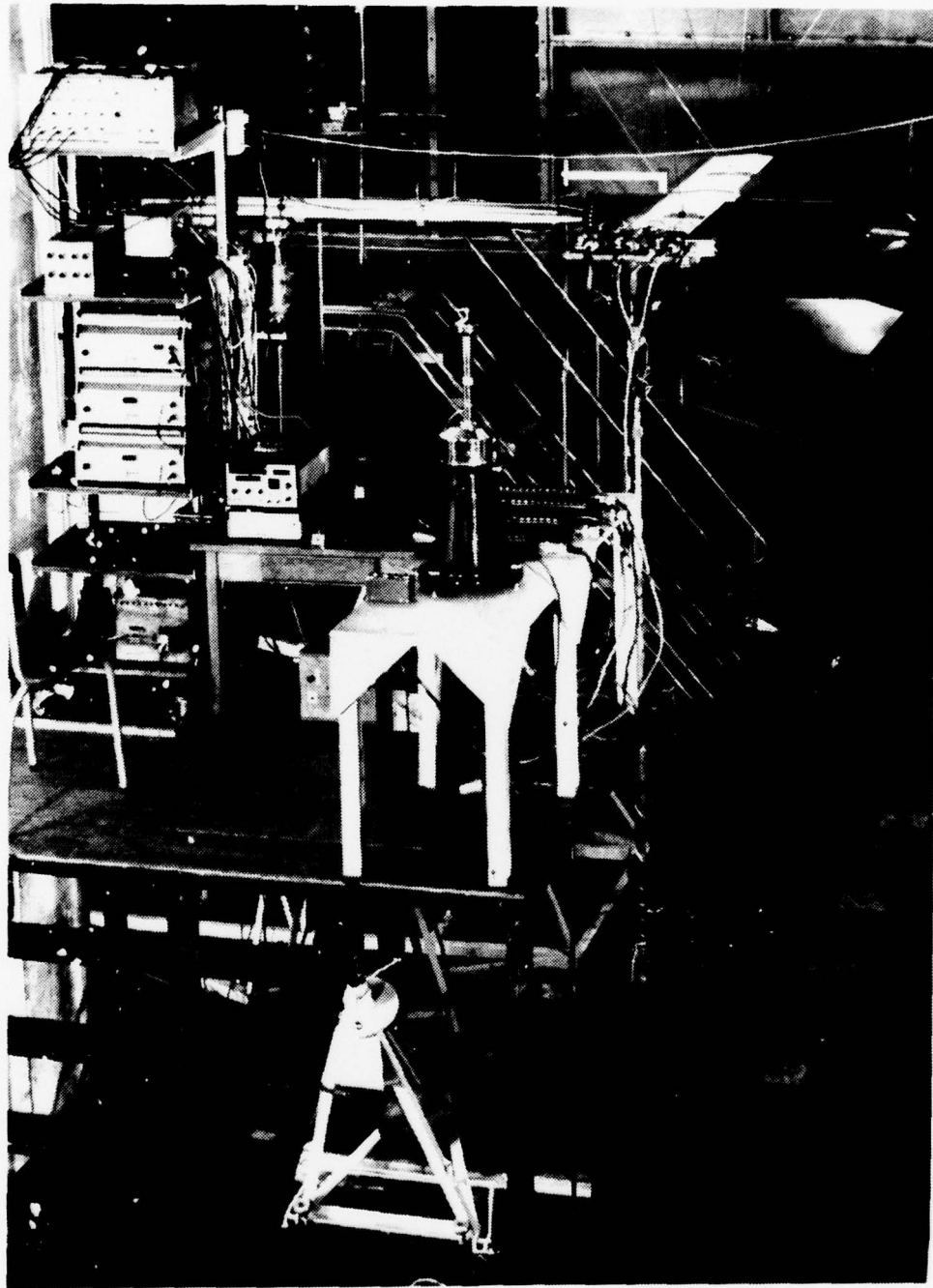


FIG. 1 - VIEW OF EXPERIMENTAL SET-UP, WITH WING AND BODY
MODELS AND INSTRUMENTATION

PRECEDING PAGE NOT FILMED
BLANK

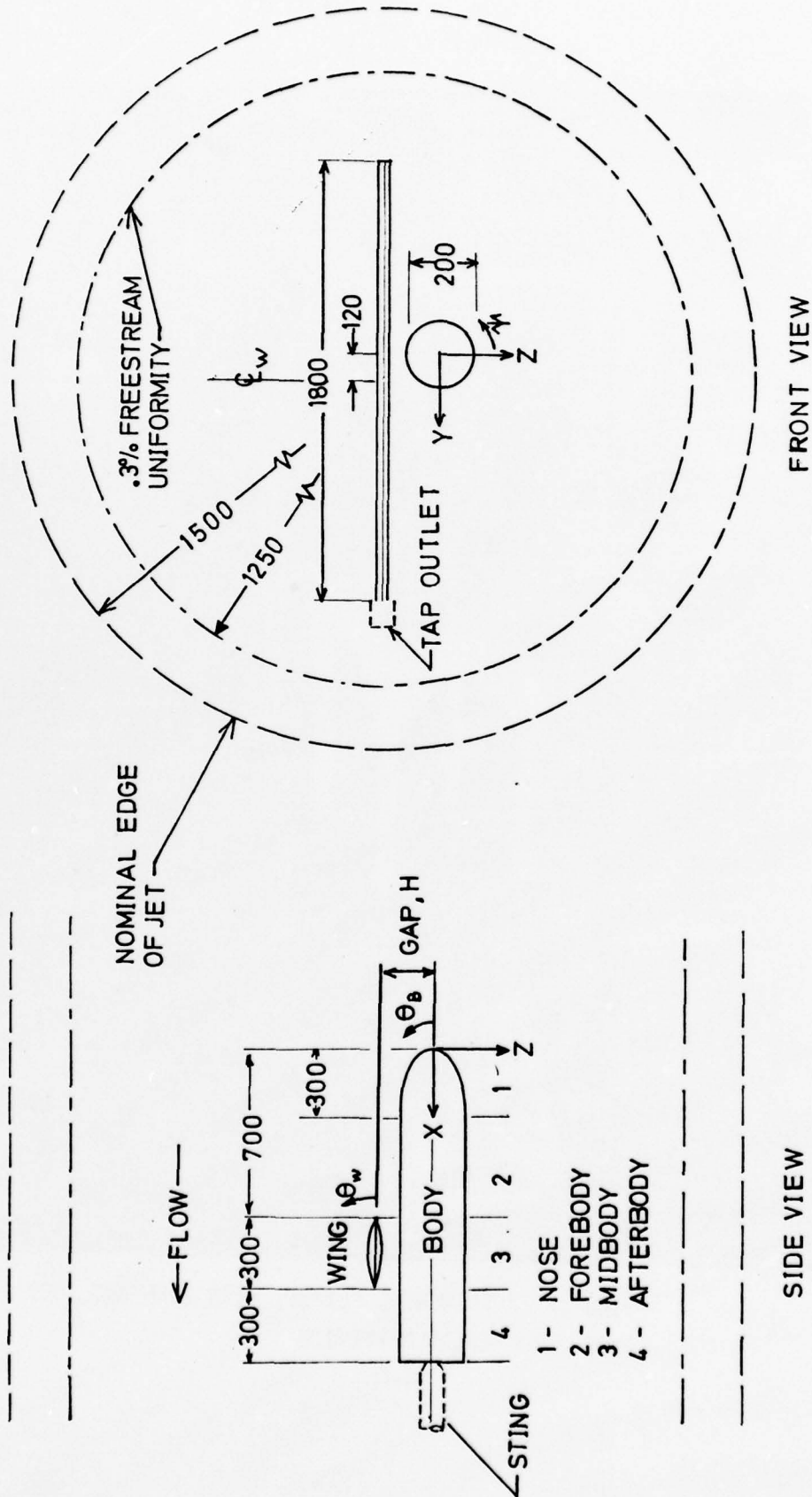


FIG. 2 - MODEL GEOMETRY AND NOMENCLATURE

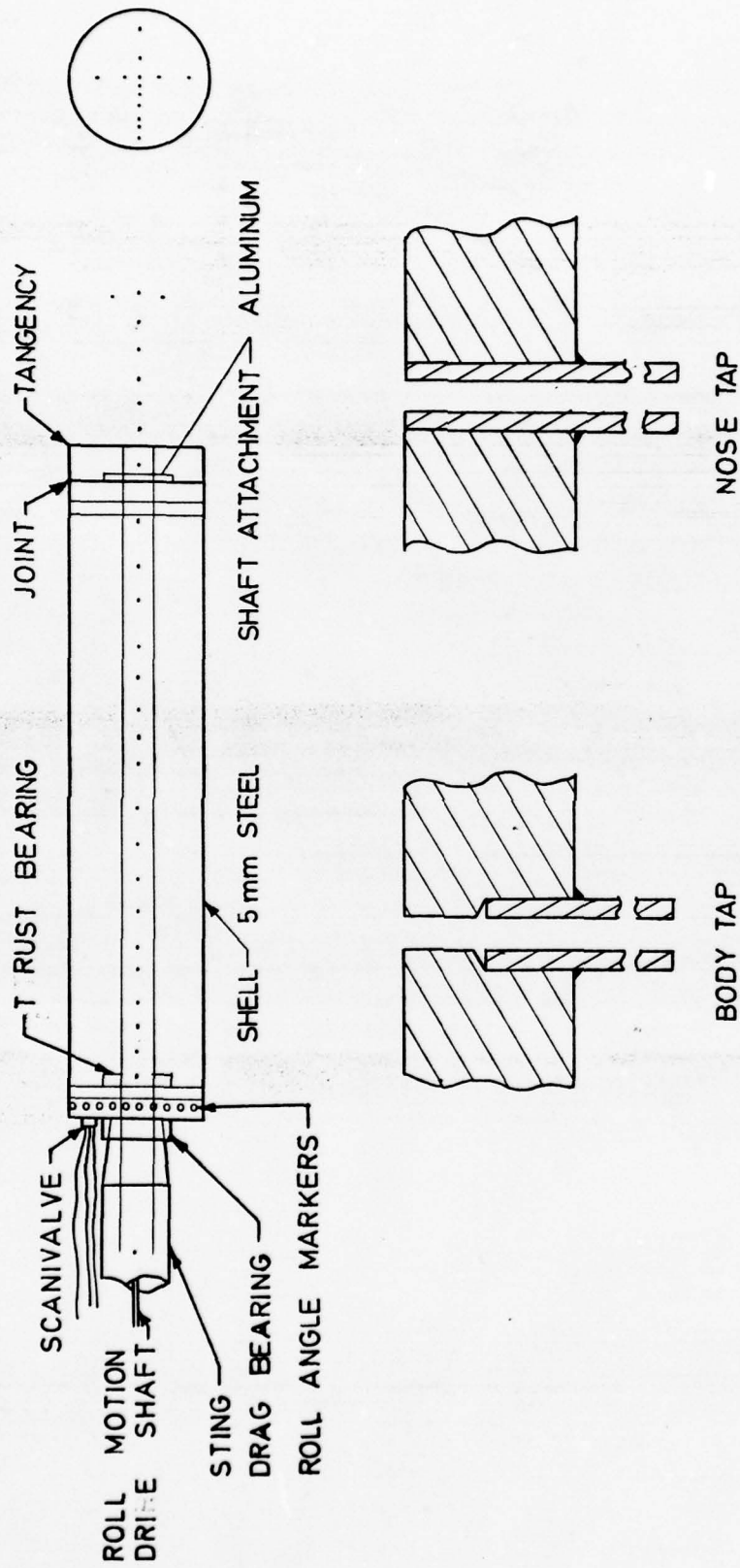


FIG. 3 - DESIGN DETAILS OF ELLIPSOID-CYLINDER MODEL

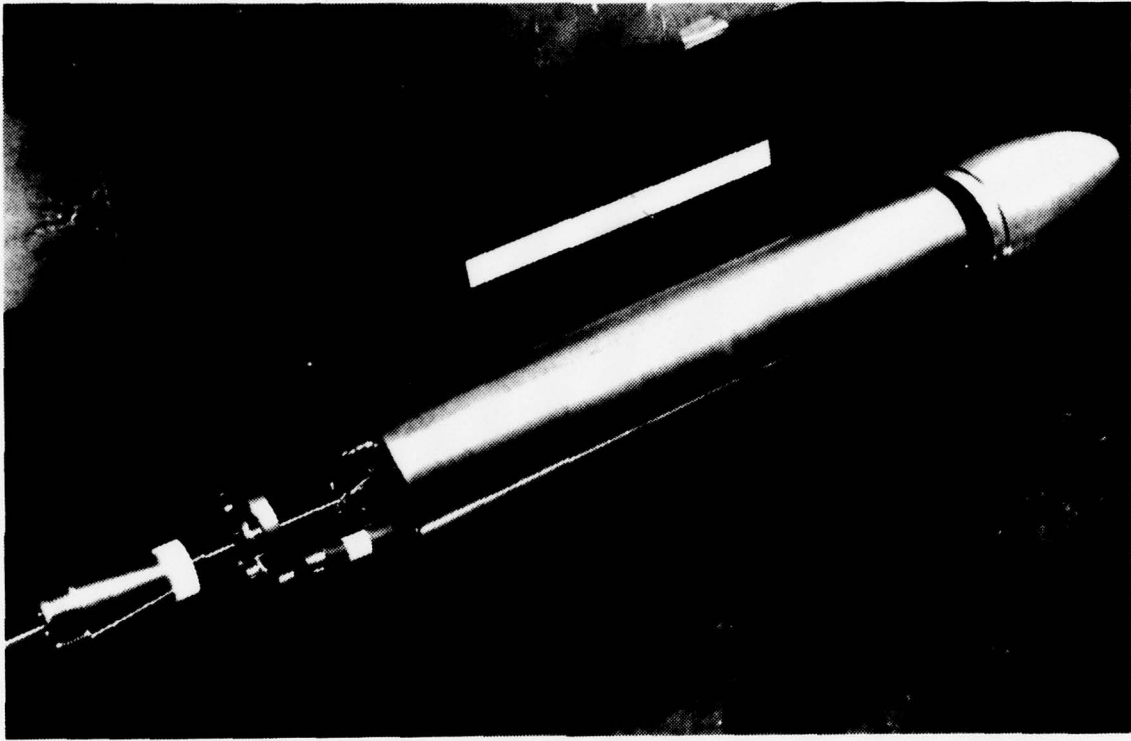
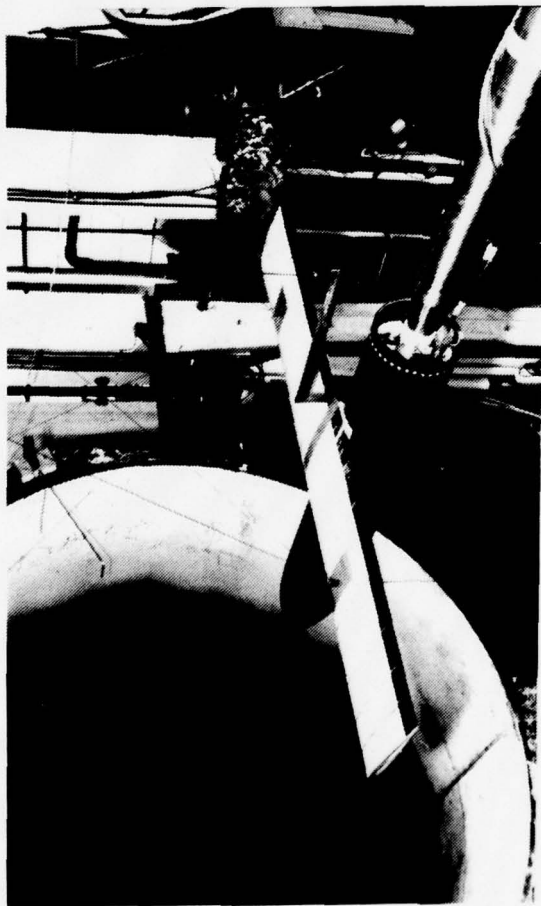
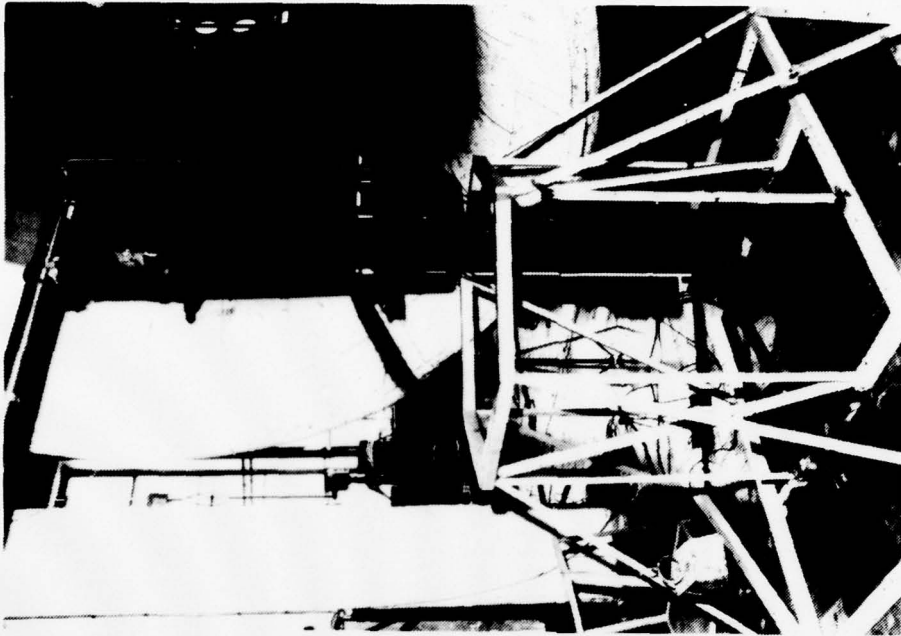


FIG. 4 - "EXPLODED" VIEW OF ELLIPSOID-CYLINDER MODEL



a) STING AND BODY



b) VERTICAL SUPPORT STRUT AND SUPPORT FRAME

FIG. 5 - VIEW OF BODY SUPPORT SYSTEM

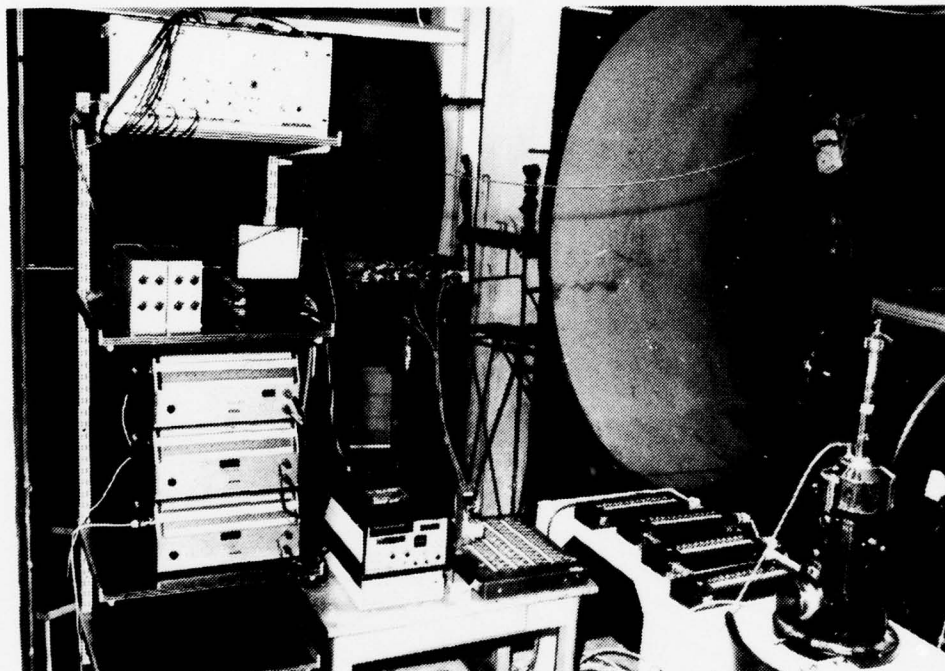


FIG. 6 - VIEW OF OPERATOR'S STATION INSTRUMENTATION

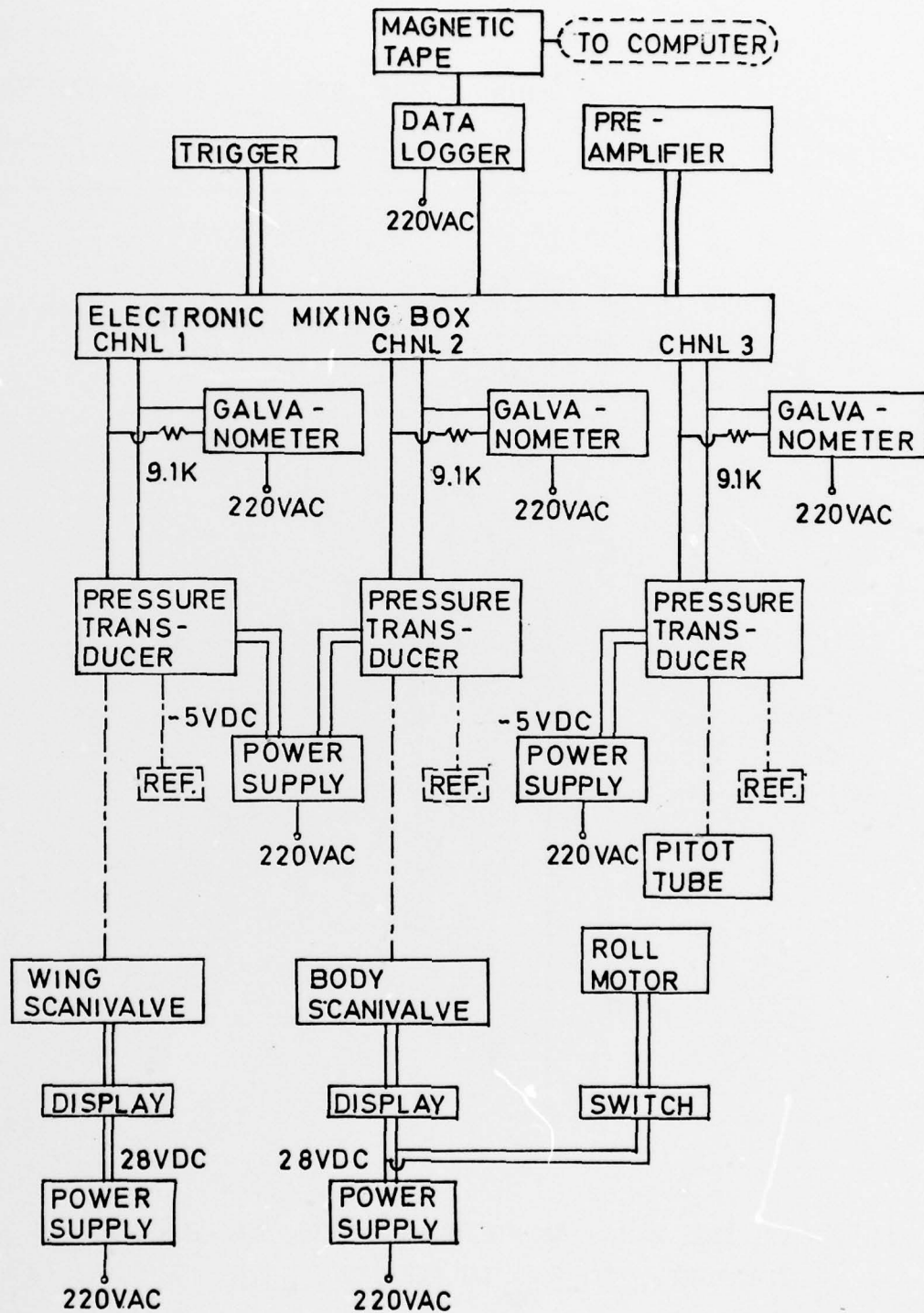


FIG. 7 - SCHEMATIC OF DATA ACQUISITION SYSTEM

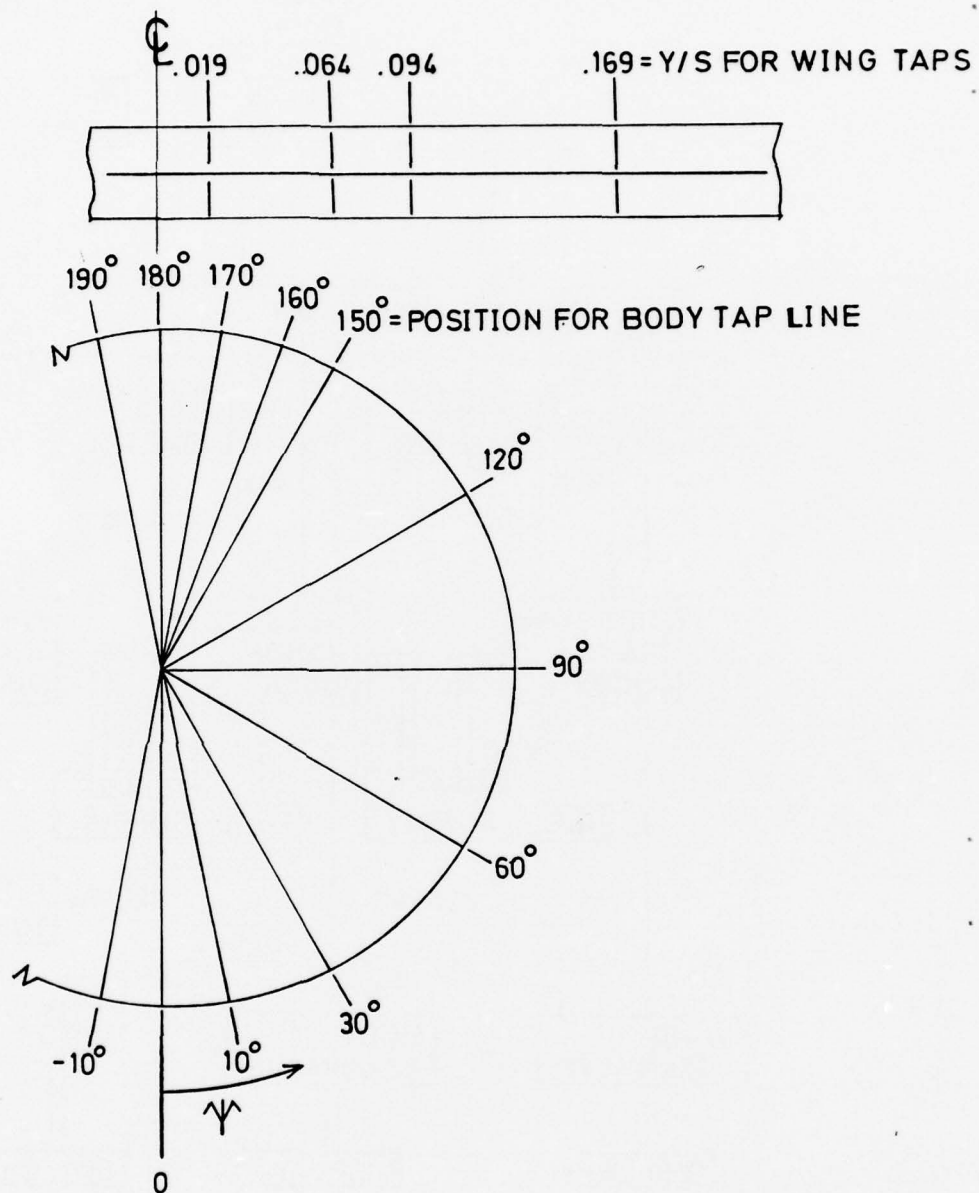


FIG. 8 - LOCATION OF INSTRUMENTED WING STATIONS AND POINTS OF PLACEMENT OF THE BODY TAP MERIDIAN

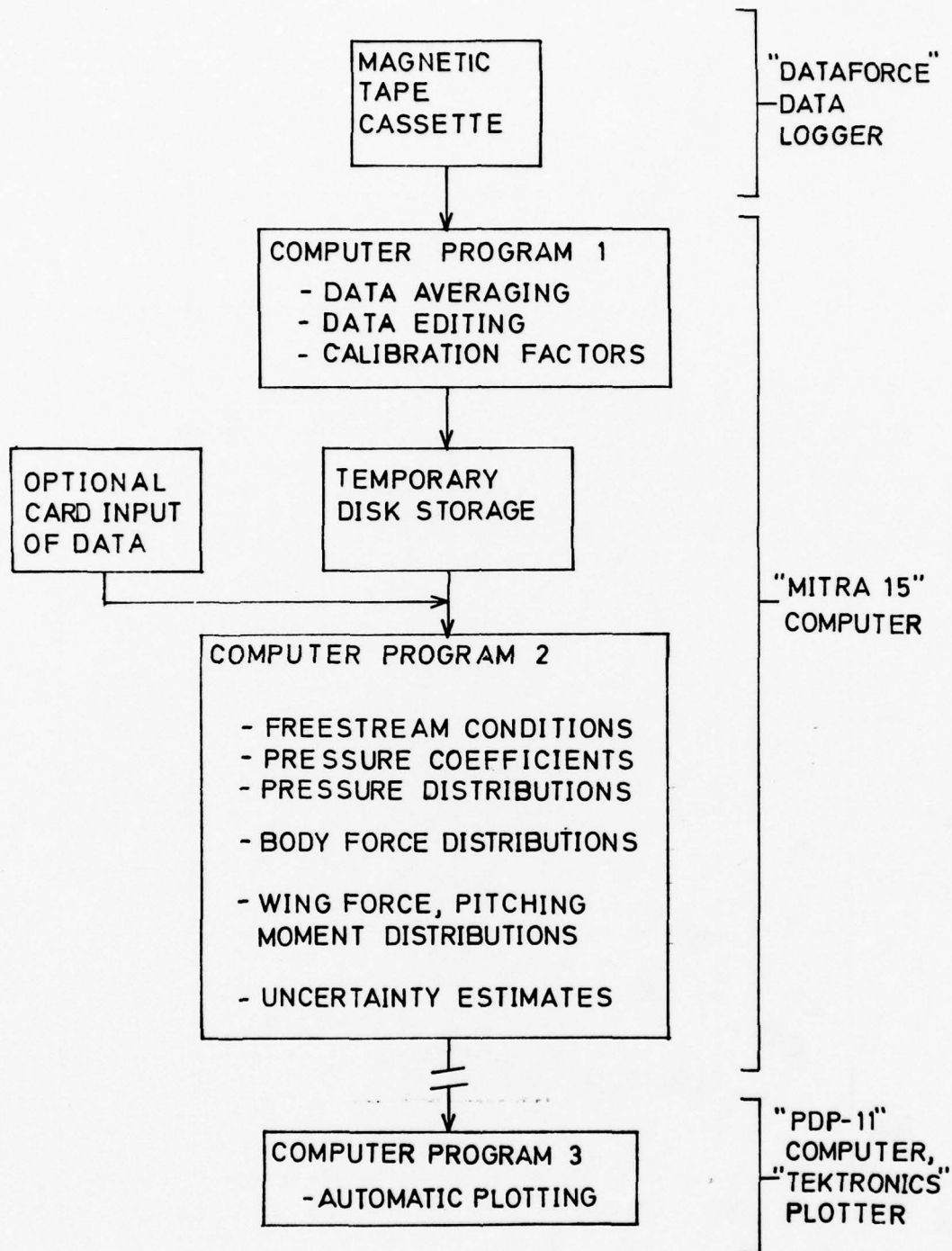
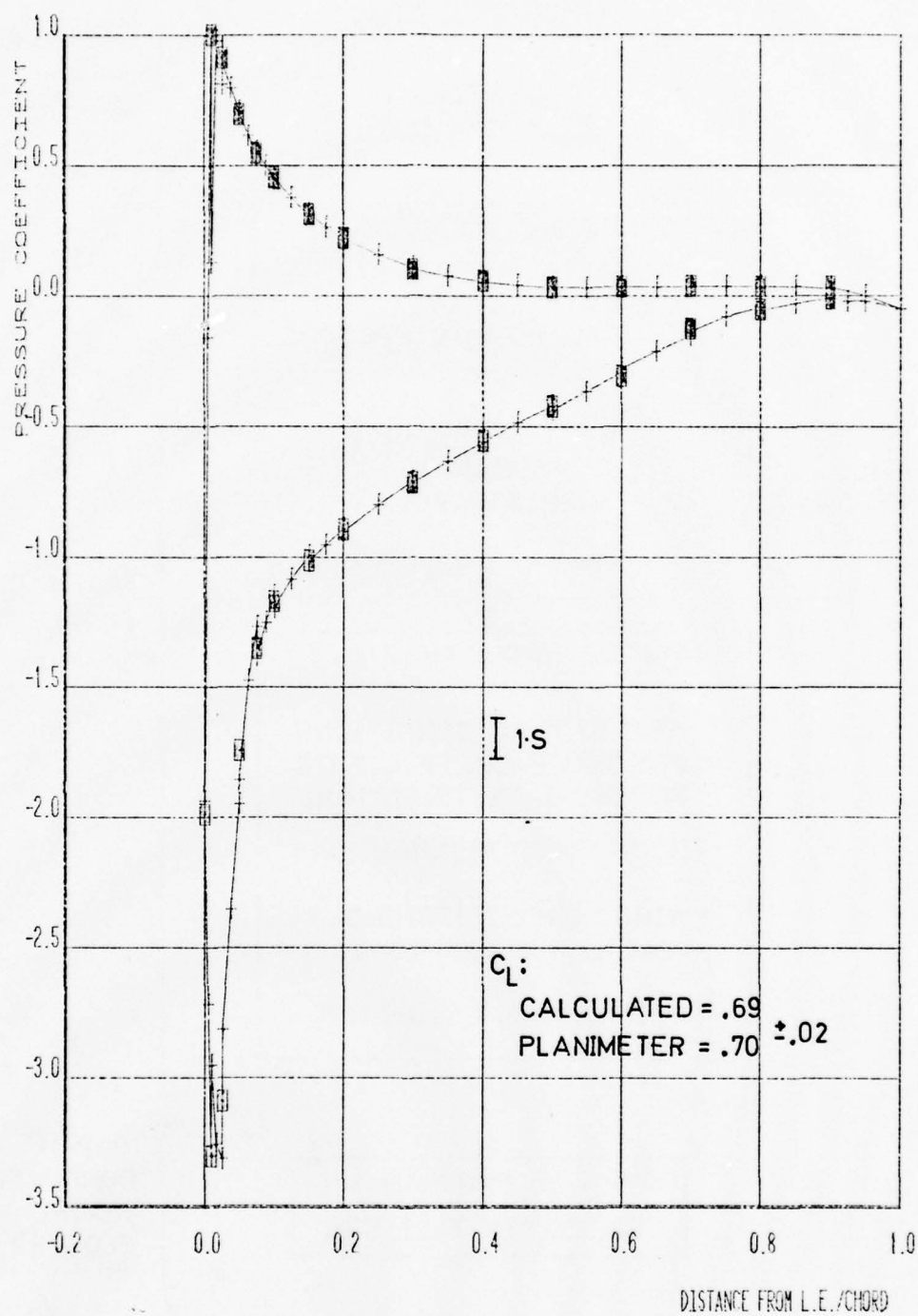


FIG. 9 - ORGANIZATION OF THE DATA REDUCTION PROCESS



\square = EXPERIMENTAL DATA $+$ = LEAST-SQUARES QUADRATIC FIT

FIG. 10 - DEMONSTRATION OF LEAST-SQUARES CURVE FIT USED
FOR INTEGRATION OF PRESSURE DISTRIBUTION

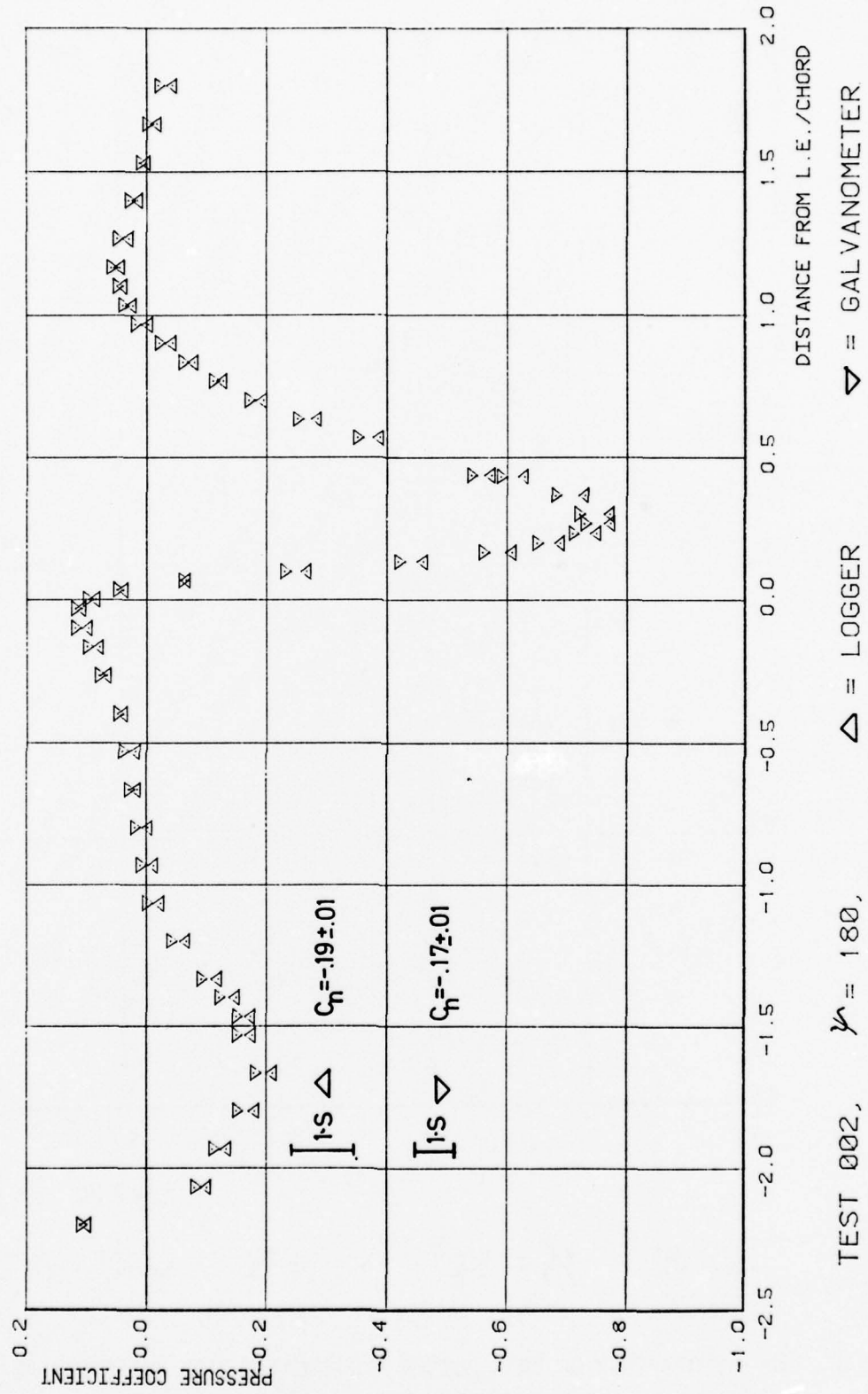
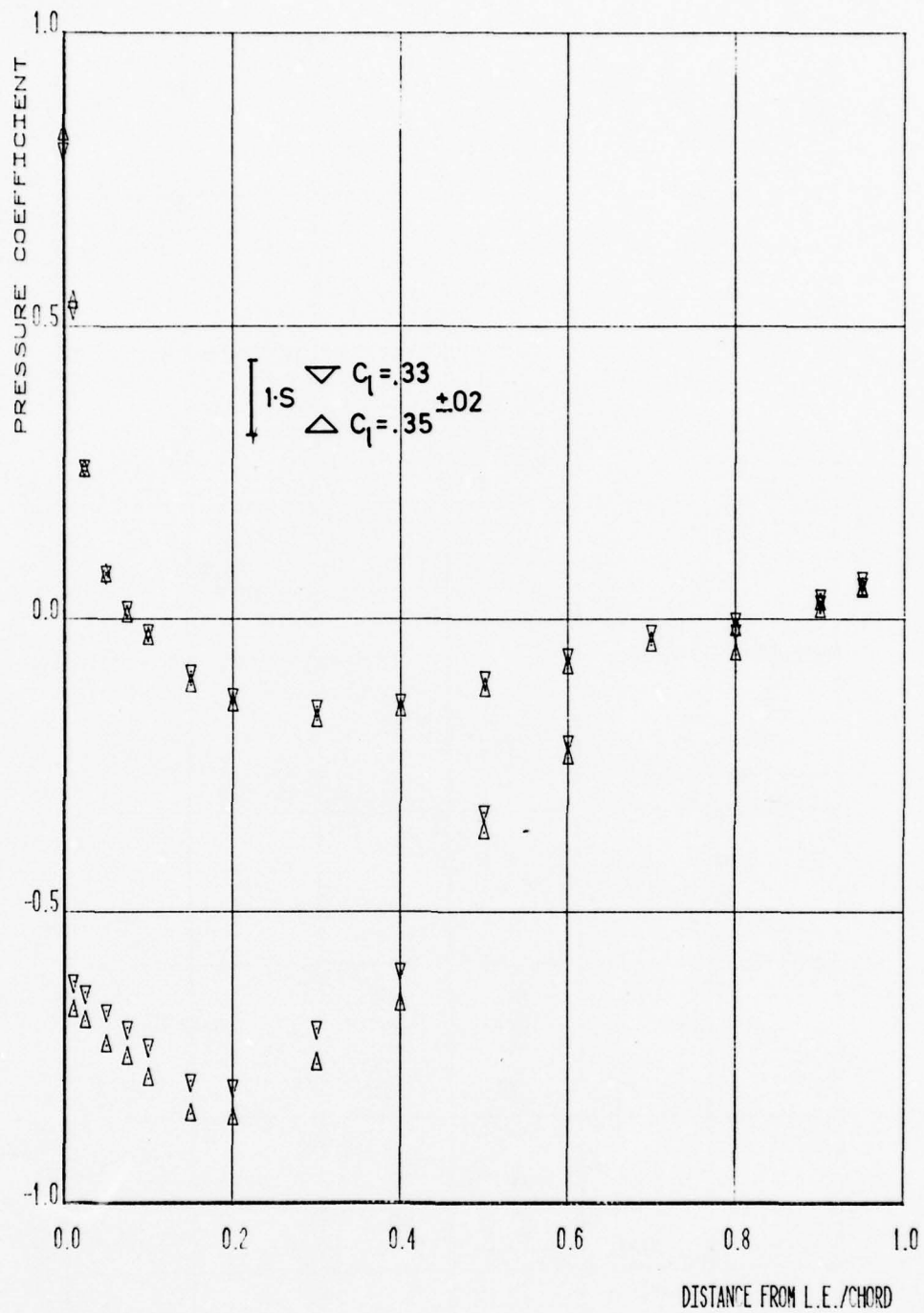
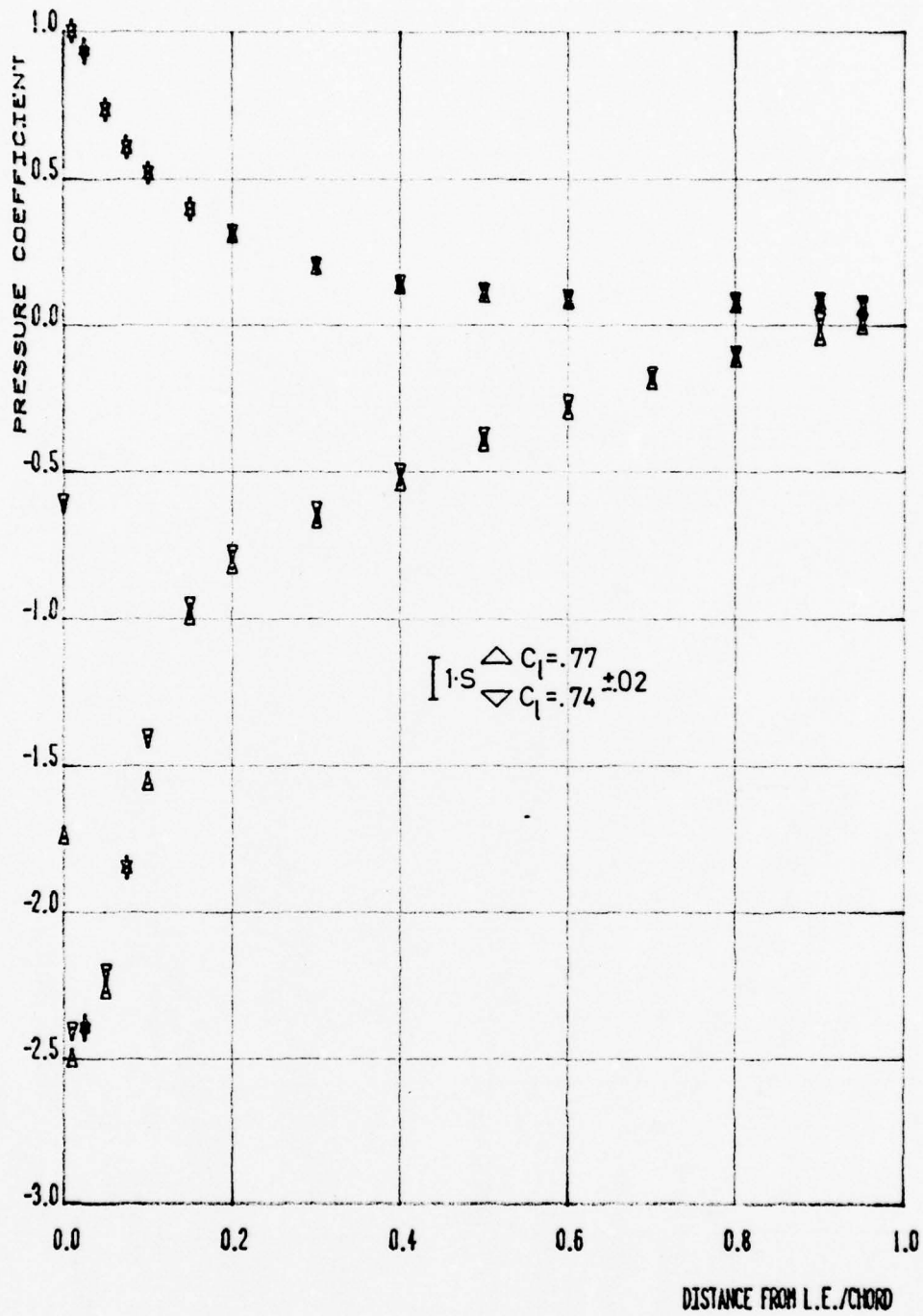


FIG. 11a - COMPARISON OF DATA LOGGER AND GALVANOMETER PRESSURE DATA FOR BODY



TEST 002, $y/s = .019$ \triangle = LOGGER ∇ = GALVANOMETER

FIG. 11b - COMPARISON OF DATA LOGGER AND GALVANOMETER PRESSURE DATA
FOR WING



TEST 007, \triangle = LOGGER ∇ = GALVANOMETER

FIG. 12 - PRESSURE DISTRIBUTION FOR WING STATION IN UNSTEADY FLOW

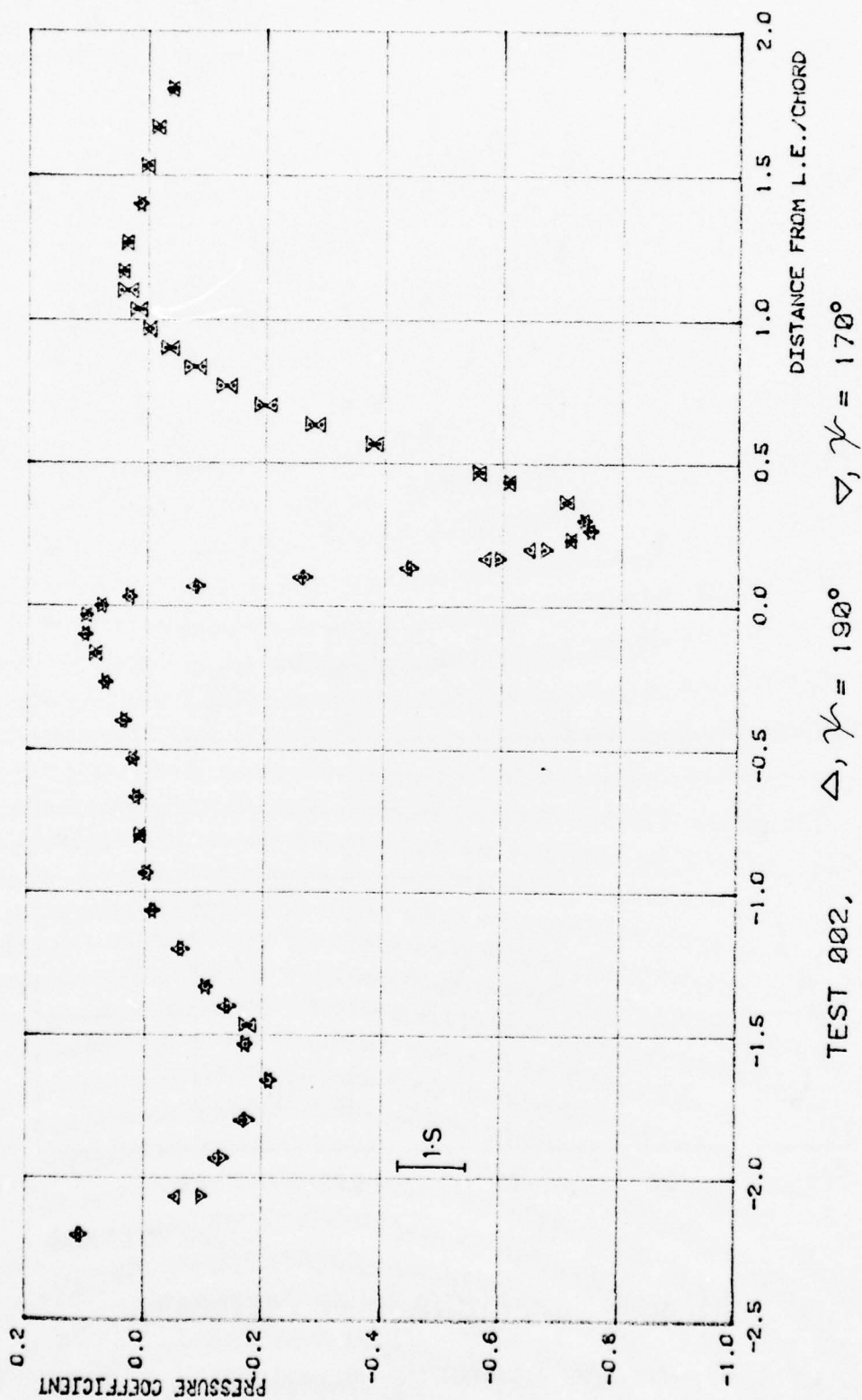


FIG. 13 - DEMONSTRATION OF SYMMETRY IN THE BODY PRESSURE DISTRIBUTIONS

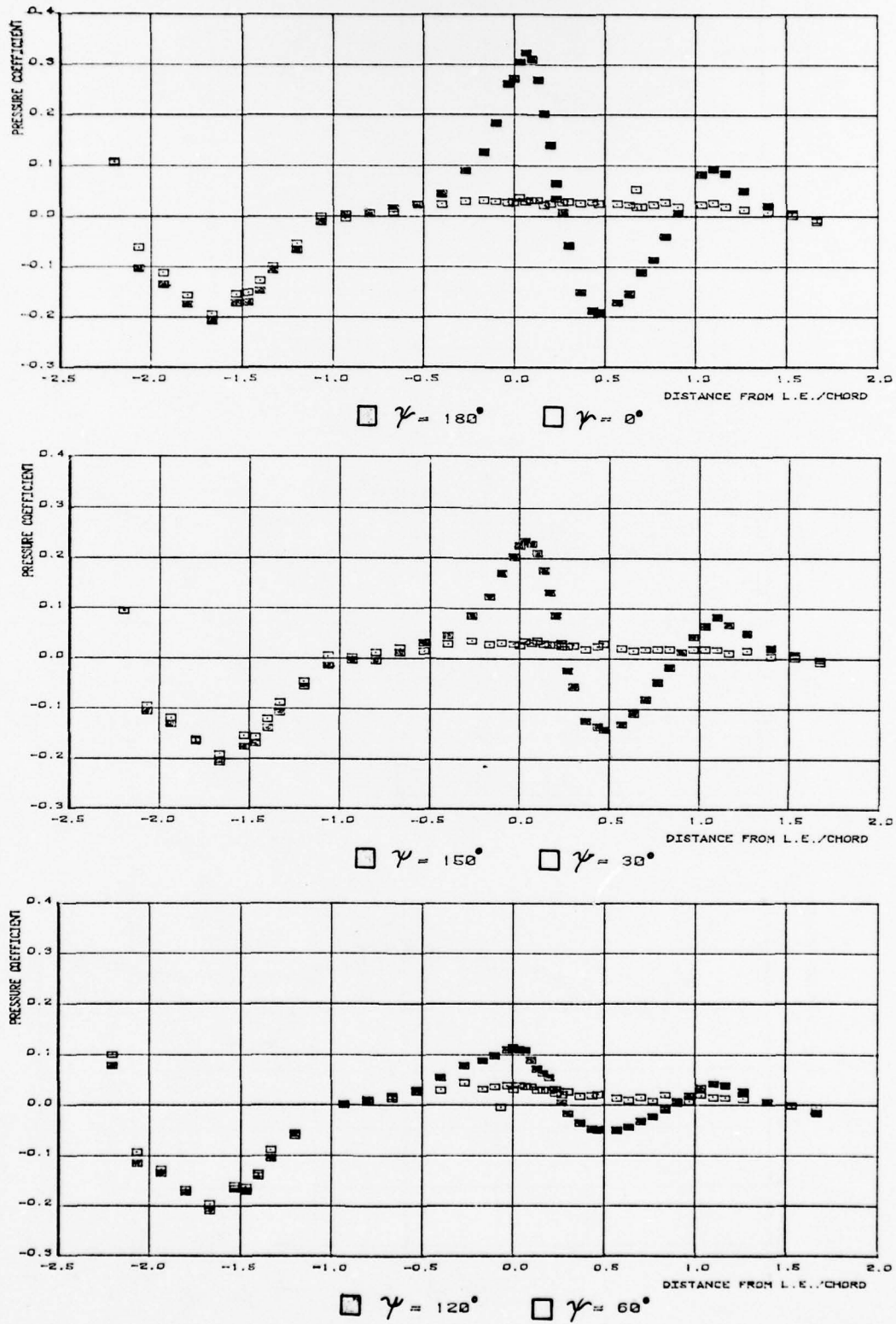


FIG. 14 - BODY CHORDWISE PRESSURE DISTRIBUTIONS FOR HIGH WING

$\theta_w = 3^\circ$, $H/C : .45$

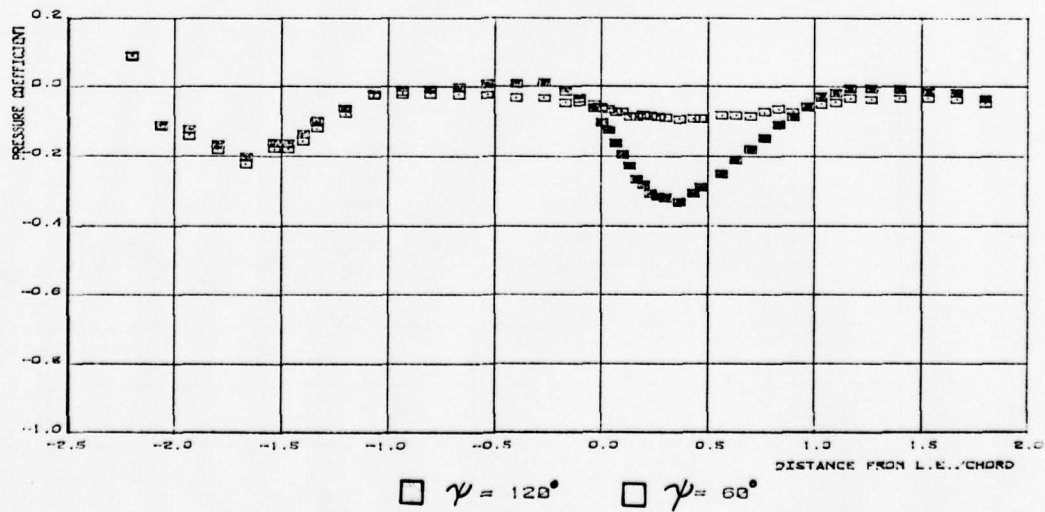
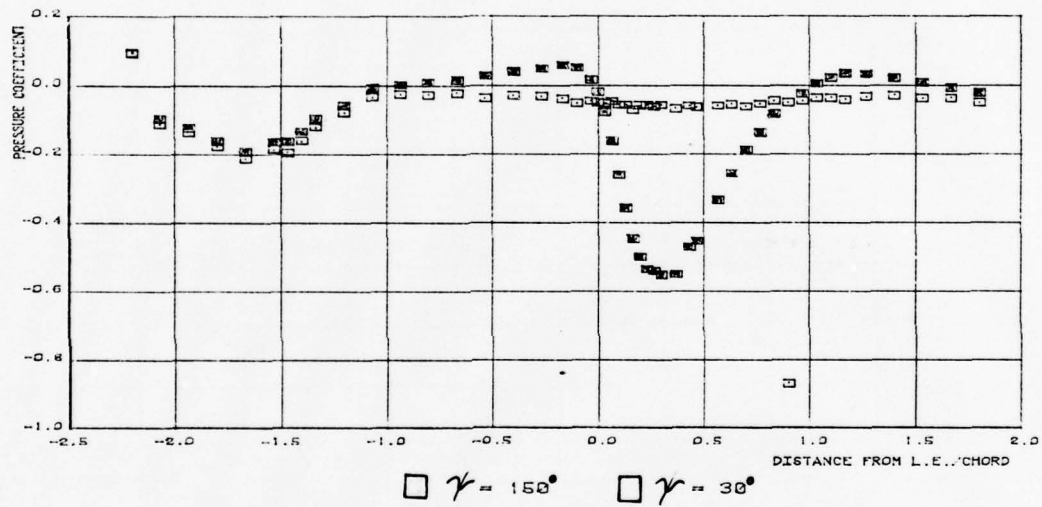
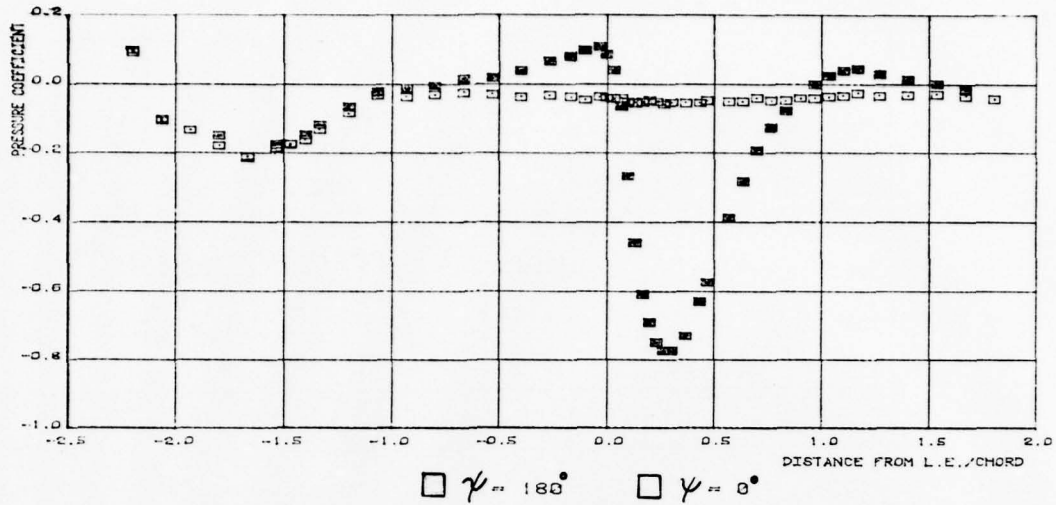
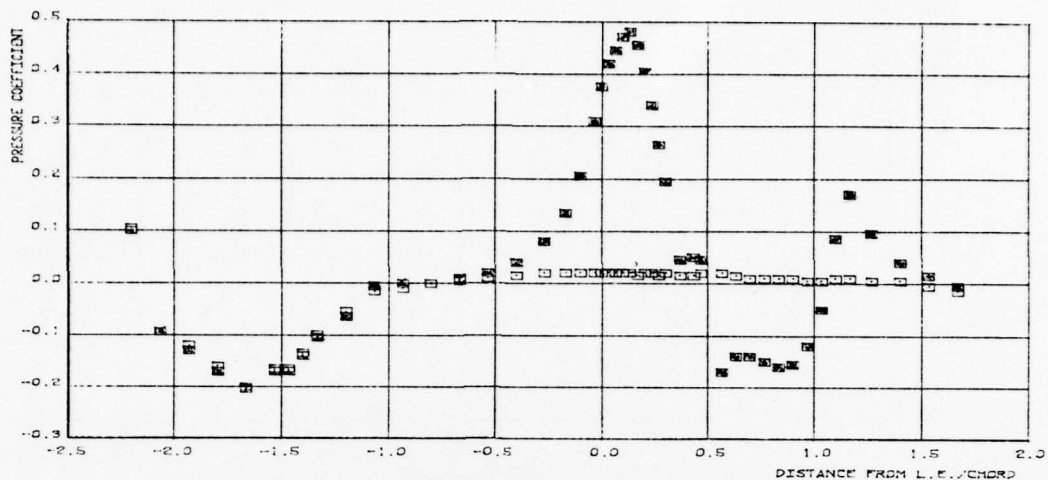
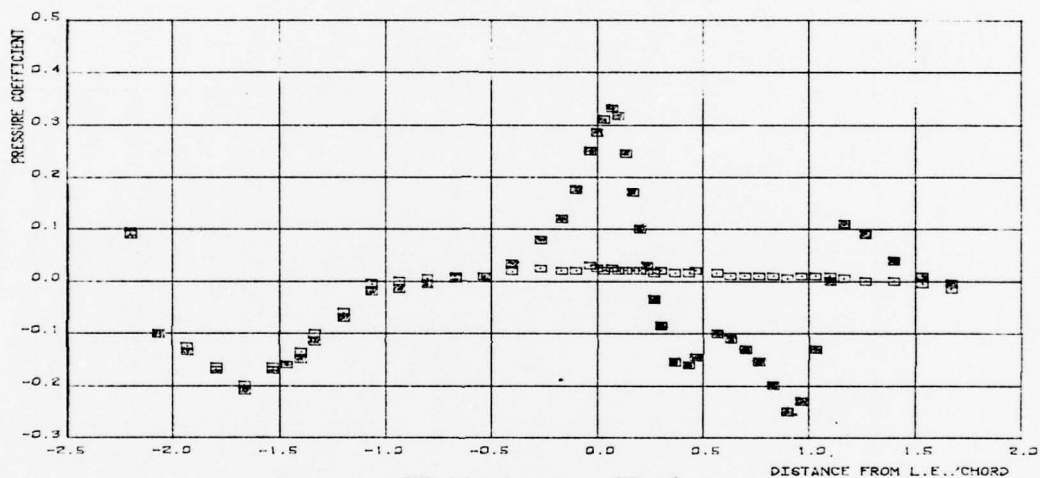


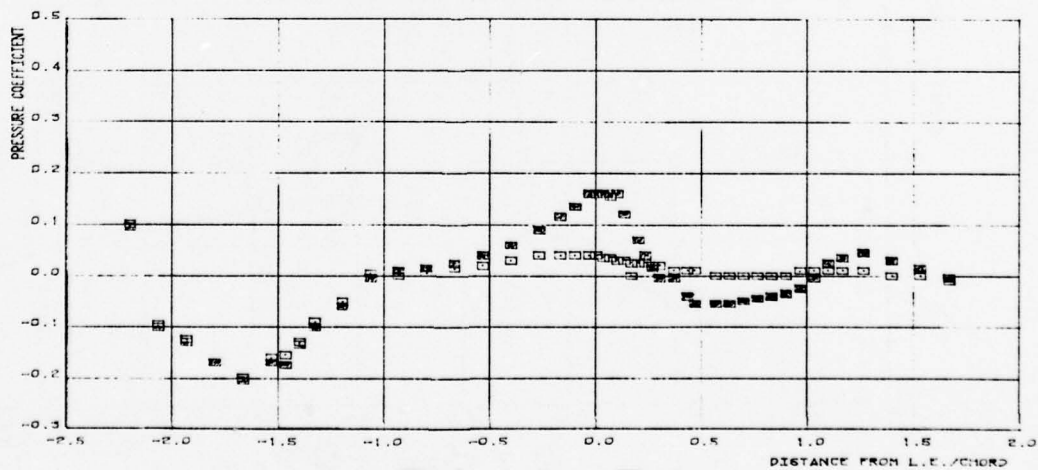
FIG. 15 - BODY CHORDWISE PRESSURE DISTRIBUTIONS FOR LO/1 WING
 $\theta_w = 3^\circ$, $H/C = .45$



$\square \gamma = 180^\circ$ $\circ \gamma = 0^\circ$



$\square \gamma = 150^\circ$ $\circ \gamma = 30^\circ$



$\square \gamma = 120^\circ$ $\circ \gamma = 60^\circ$

FIG. 16 - BODY CHORDWISE PRESSURE DISTRIBUTIONS FOR HIGH WING

$\theta_w = 3^\circ$, $H/C = .39$ (minimum gap)

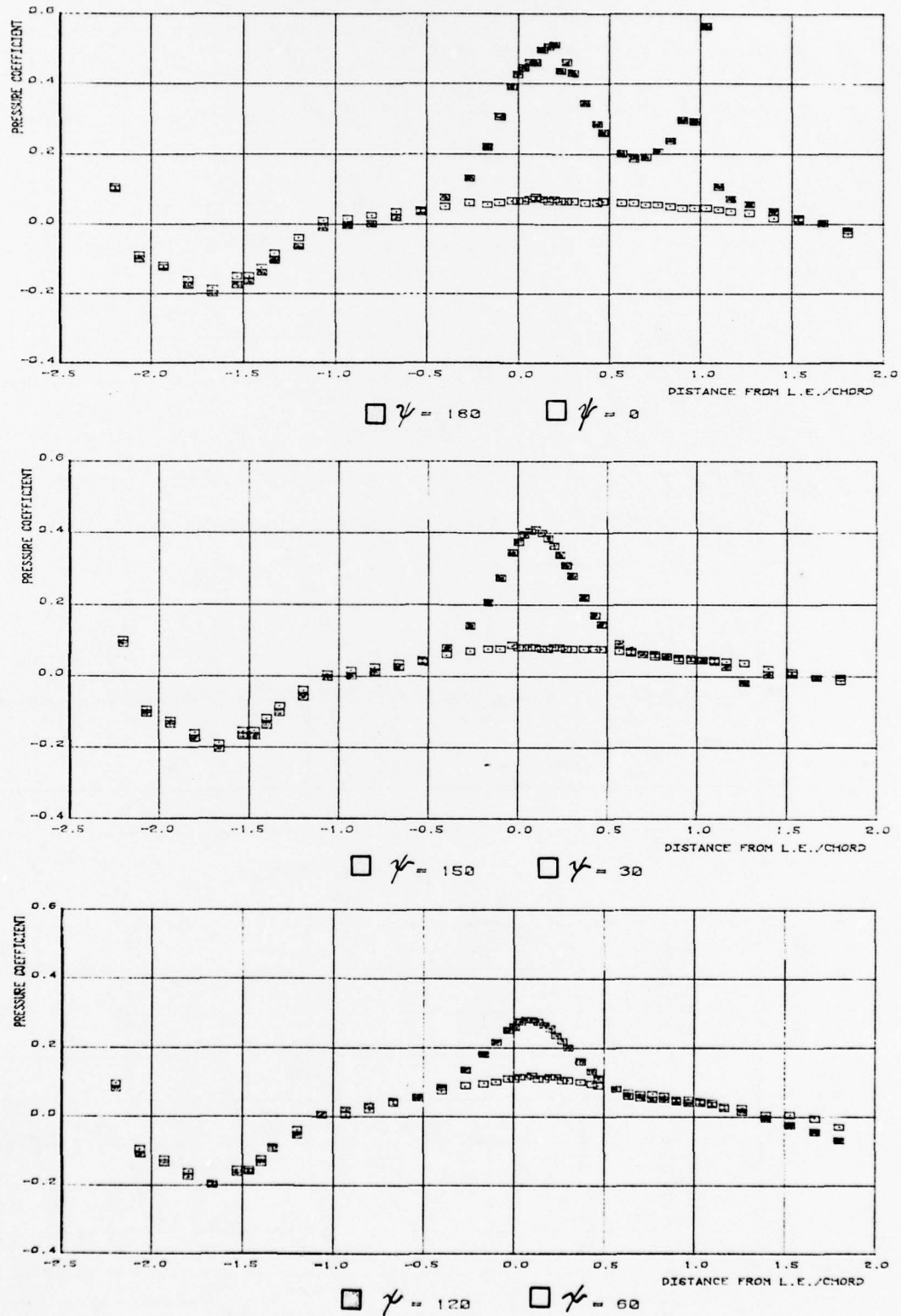
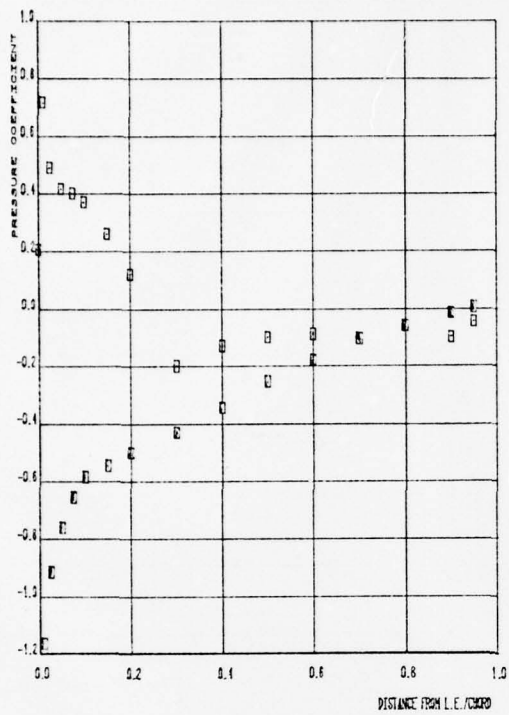
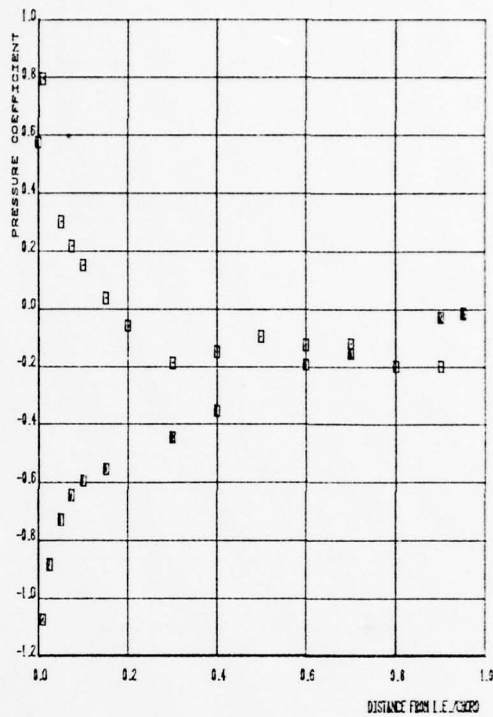


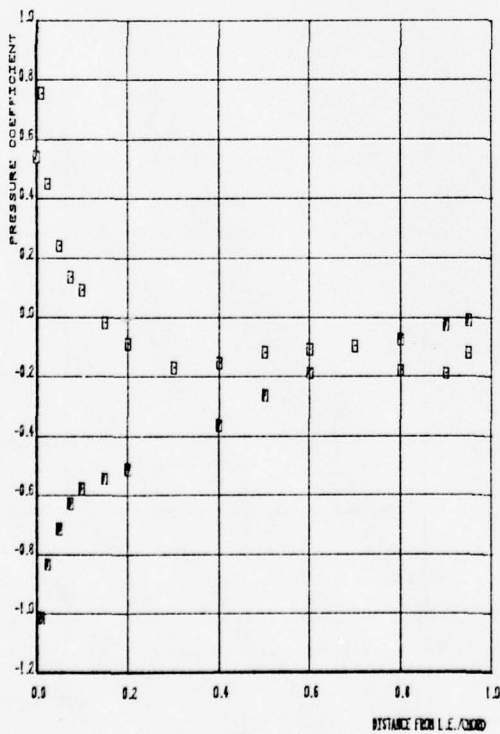
FIG. 17 - BODY CHORDWISE PRESSURE DISTRIBUTIONS FOR HIGH WING
 $\theta_w = 9^\circ$, $H/C = .45$ (minimum gap)



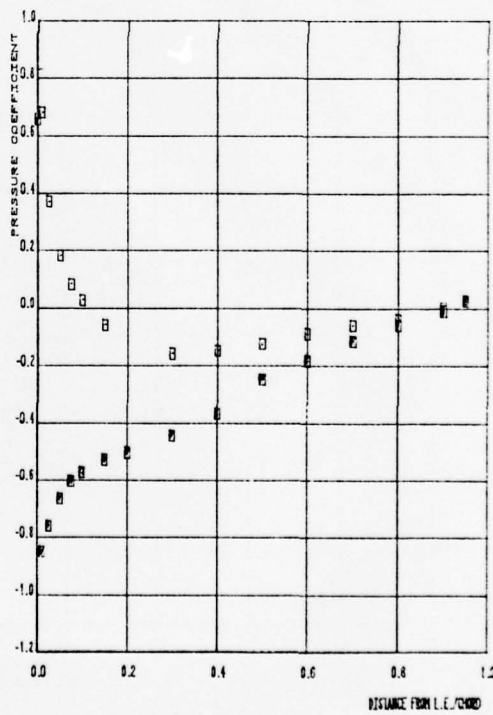
$$y/s = 0.019$$



$$y/s = 0.064$$



$$y/s = 0.094$$

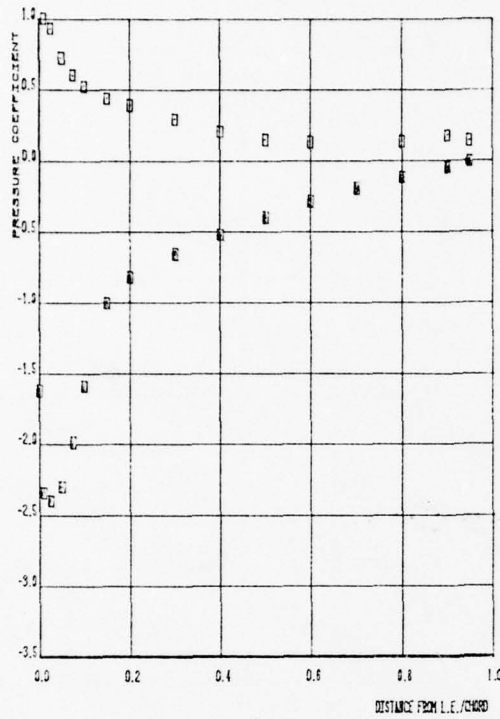


$$y/s = 0.109$$

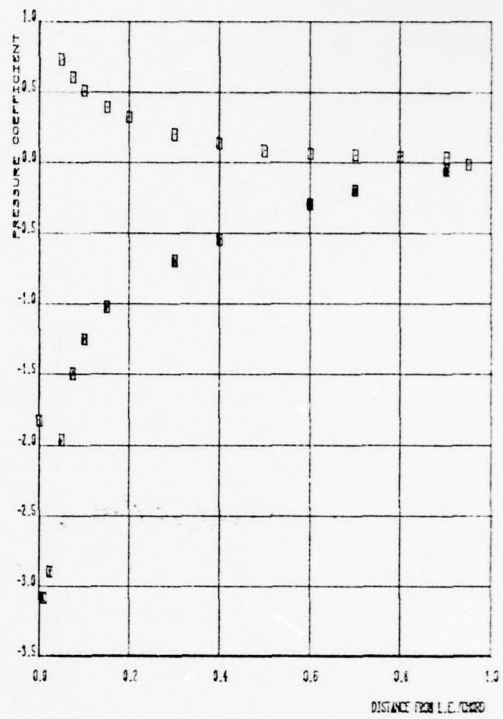
FIG. 18 - WING CHORDWISE PRESSURE DISTRIBUTIONS FOR HIGH WING
 $\theta_w = 3^\circ$, $H/C = .39$ (minimum gap)

18

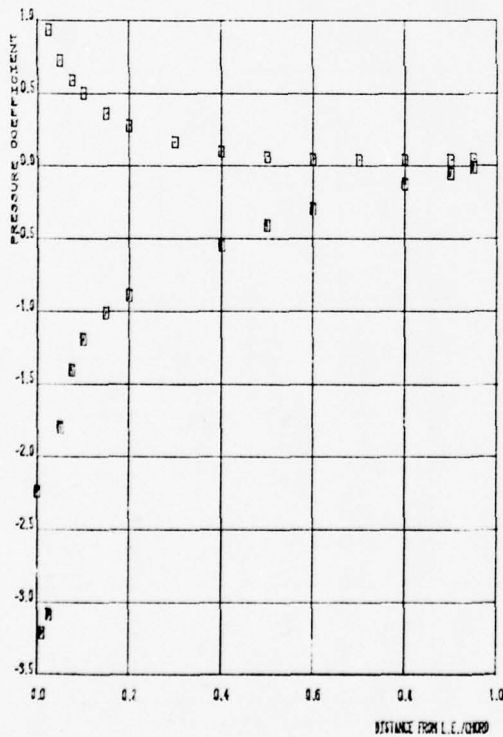
22



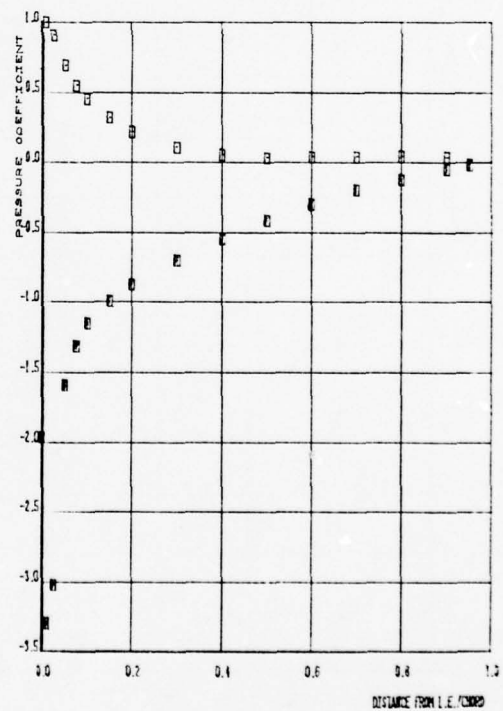
$$y/s = 0.019$$



$$y/s = 0.064$$



$$y/s = 0.094$$



$$y/s = 0.160$$

FIG. 19 - WING CHORDWISE PRESSURE DISTRIBUTIONS FOR HIGH WING
 $\theta_w = 9^\circ$, $H/C = .45$ (minimum gap)

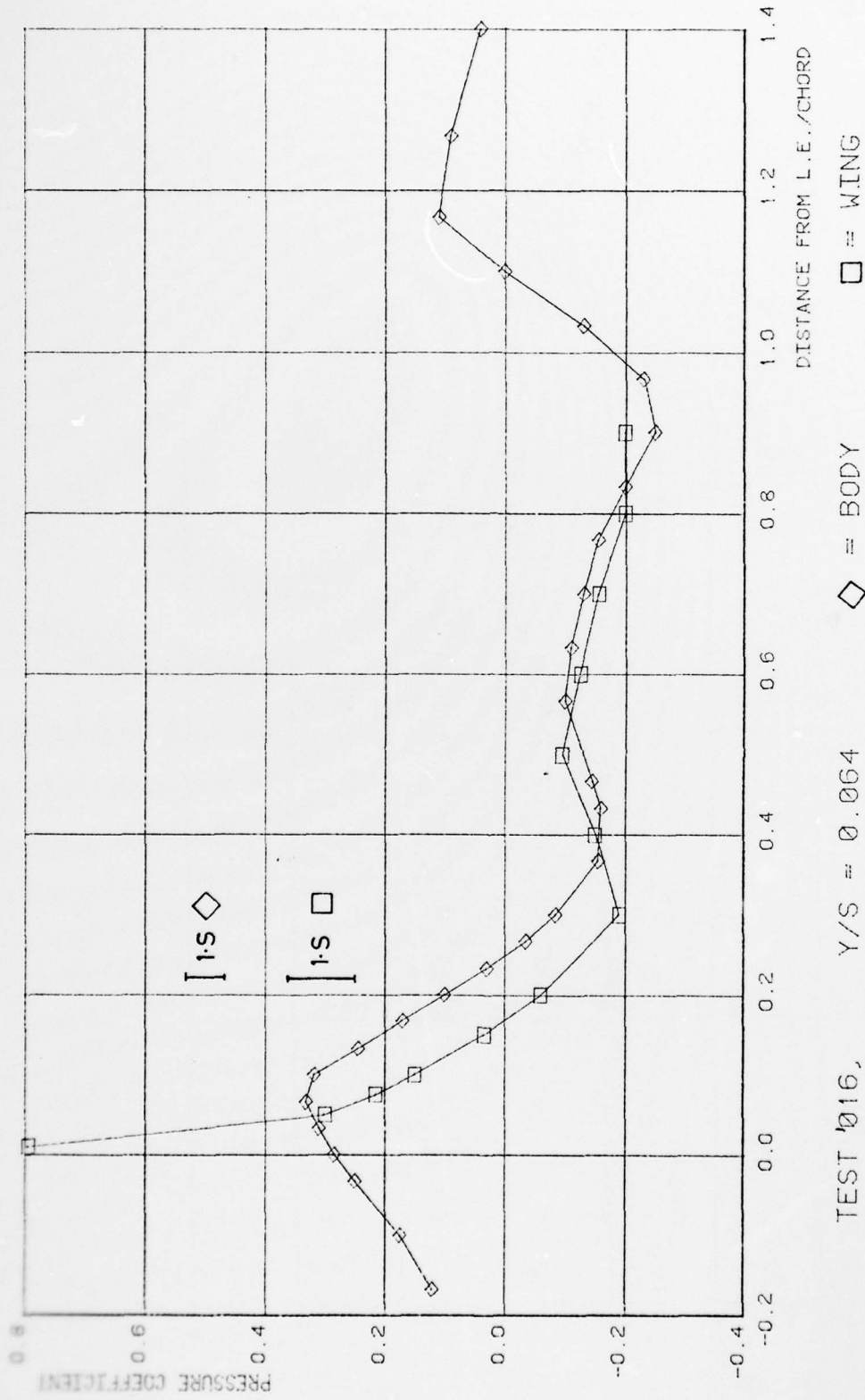


FIG. 20 - COMPARISON OF WING AND BODY CHORDWISE PRESSURE DISTRIBUTION AT $Y/S = .064$ FOR HIGH WING

$\theta_w = 3^\circ$, $H/C = .39$ (minimum gap)

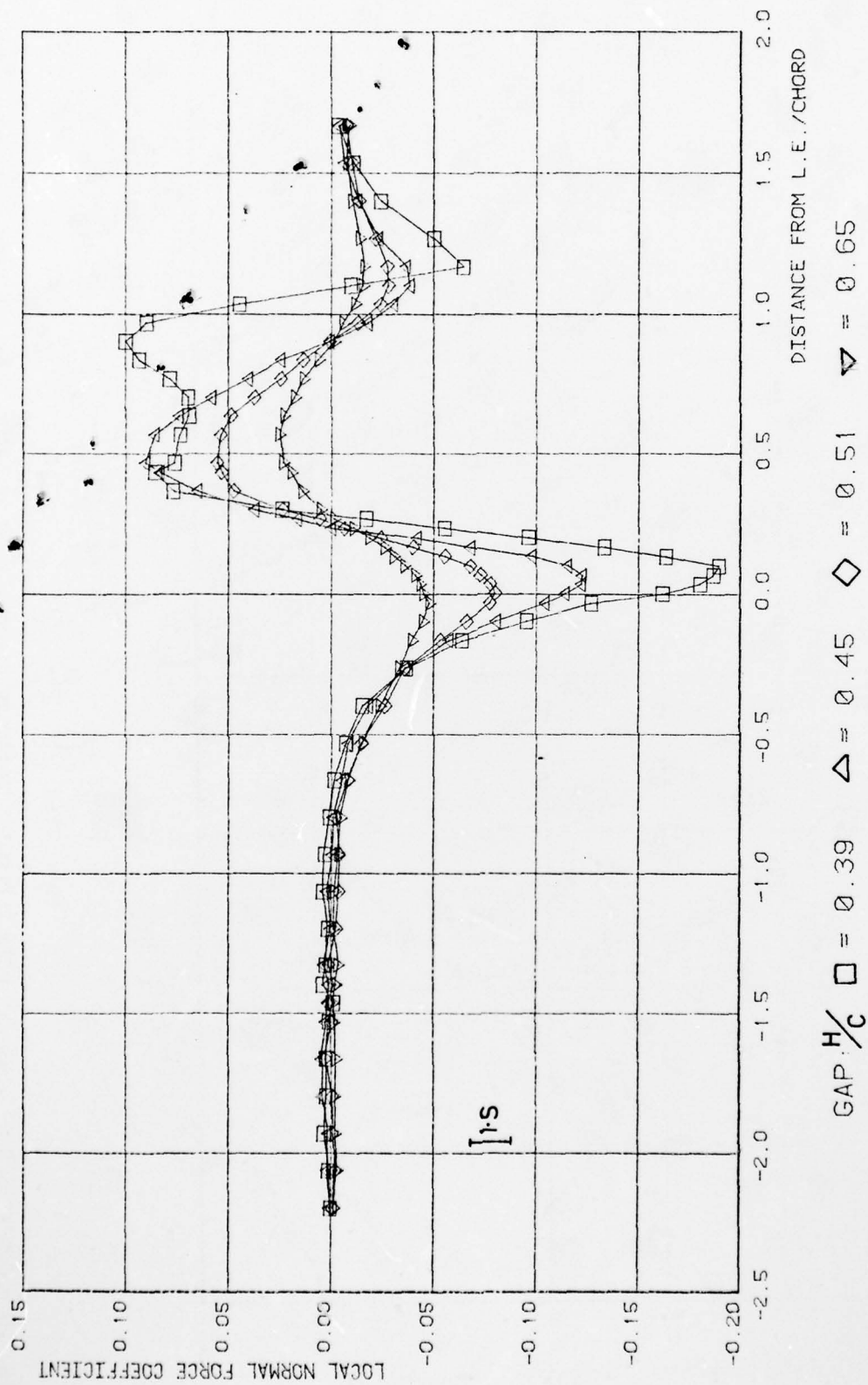


FIG. 21 - BODY CHORDWISE NORMAL FORCE DISTRIBUTION VERSUS GAP HEIGHT FOR HIGH WING, $\theta_w = 3^\circ$

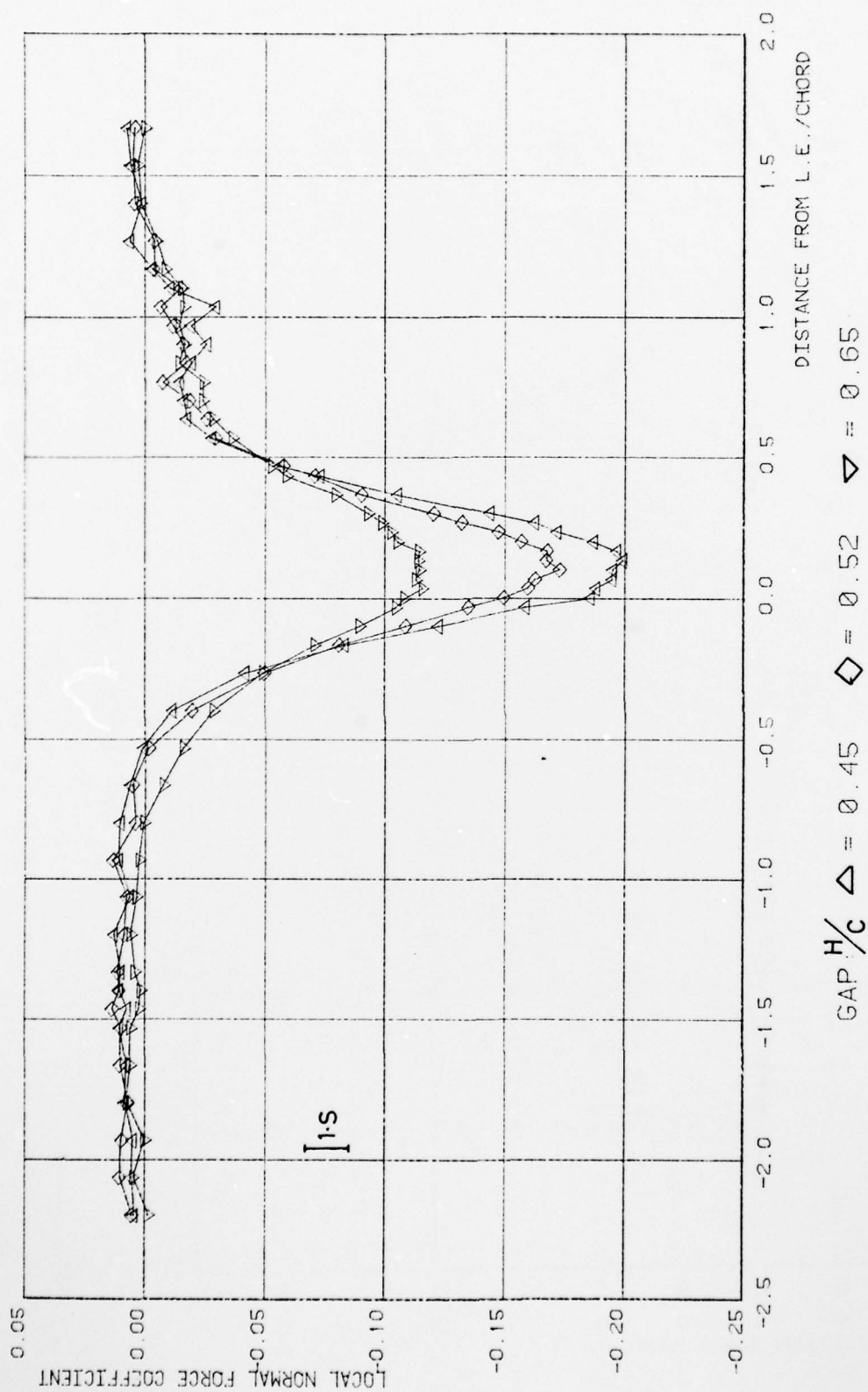


FIG. 22 - BODY CHORDWISE NORMAL FORCE DISTRIBUTION VERSUS GAP HEIGHT FOR HIGH WING, $\theta_w = 9^\circ$

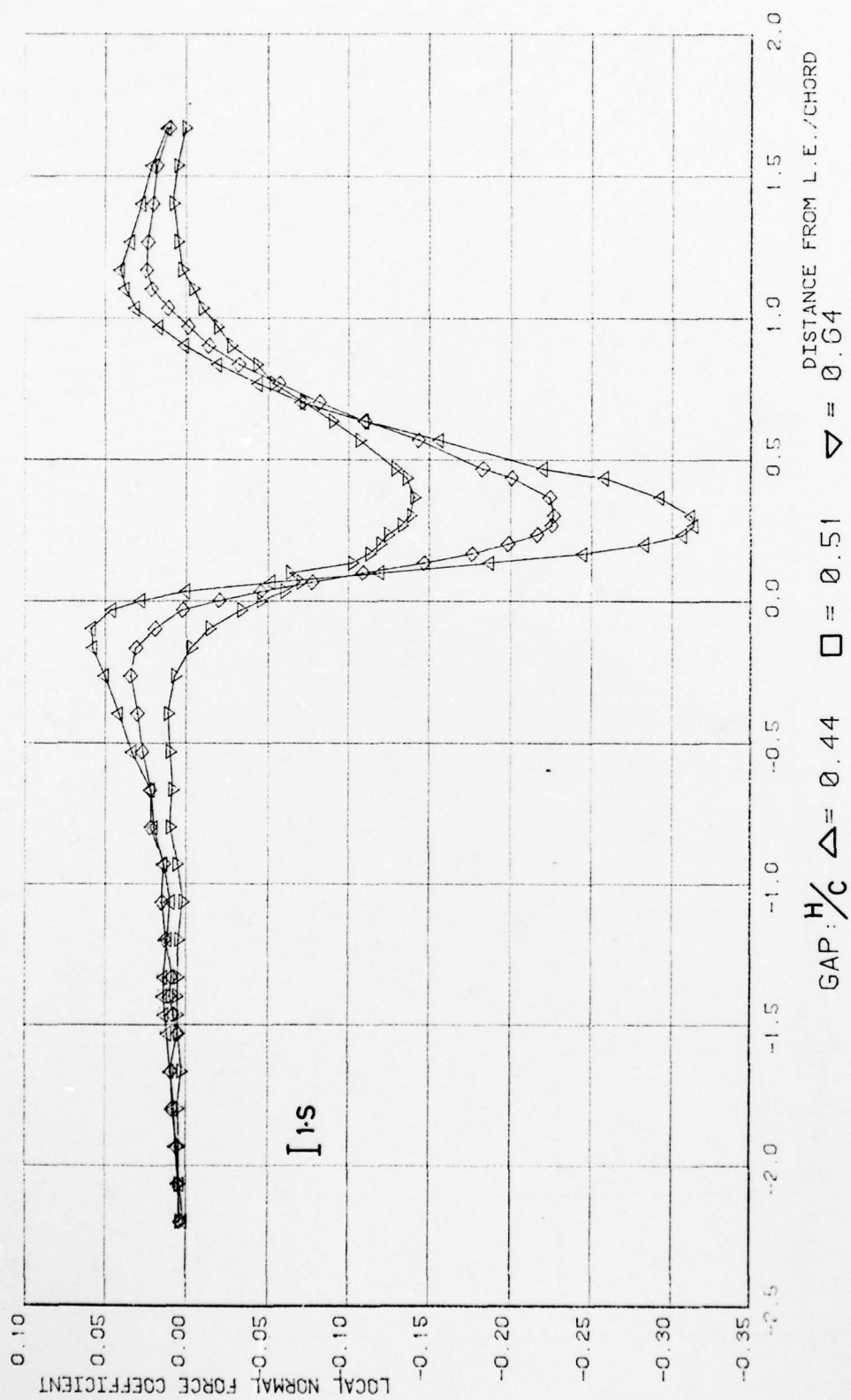


FIG. 23 - BODY CHORDWISE NORMAL FORCE DISTRIBUTION VERSUS GAP HEIGHT FOR LOW WING, $\theta_w = 3^\circ$

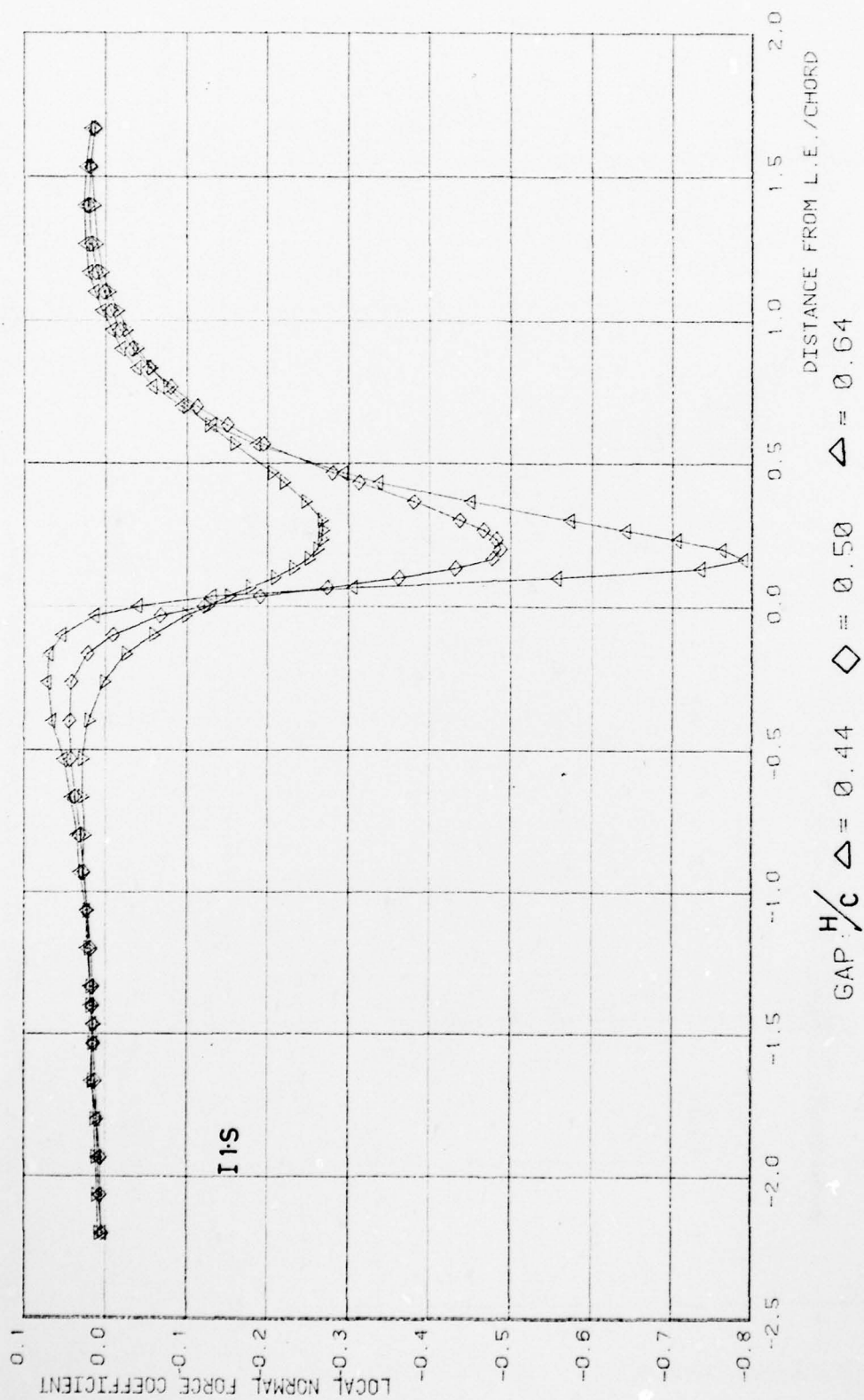


FIG. 24 - BODY CHORDWISE NORMAL FORCE DISTRIBUTION VERSUS GAP HEIGHT FOR LOW WING, $\theta_w = 9^\circ$

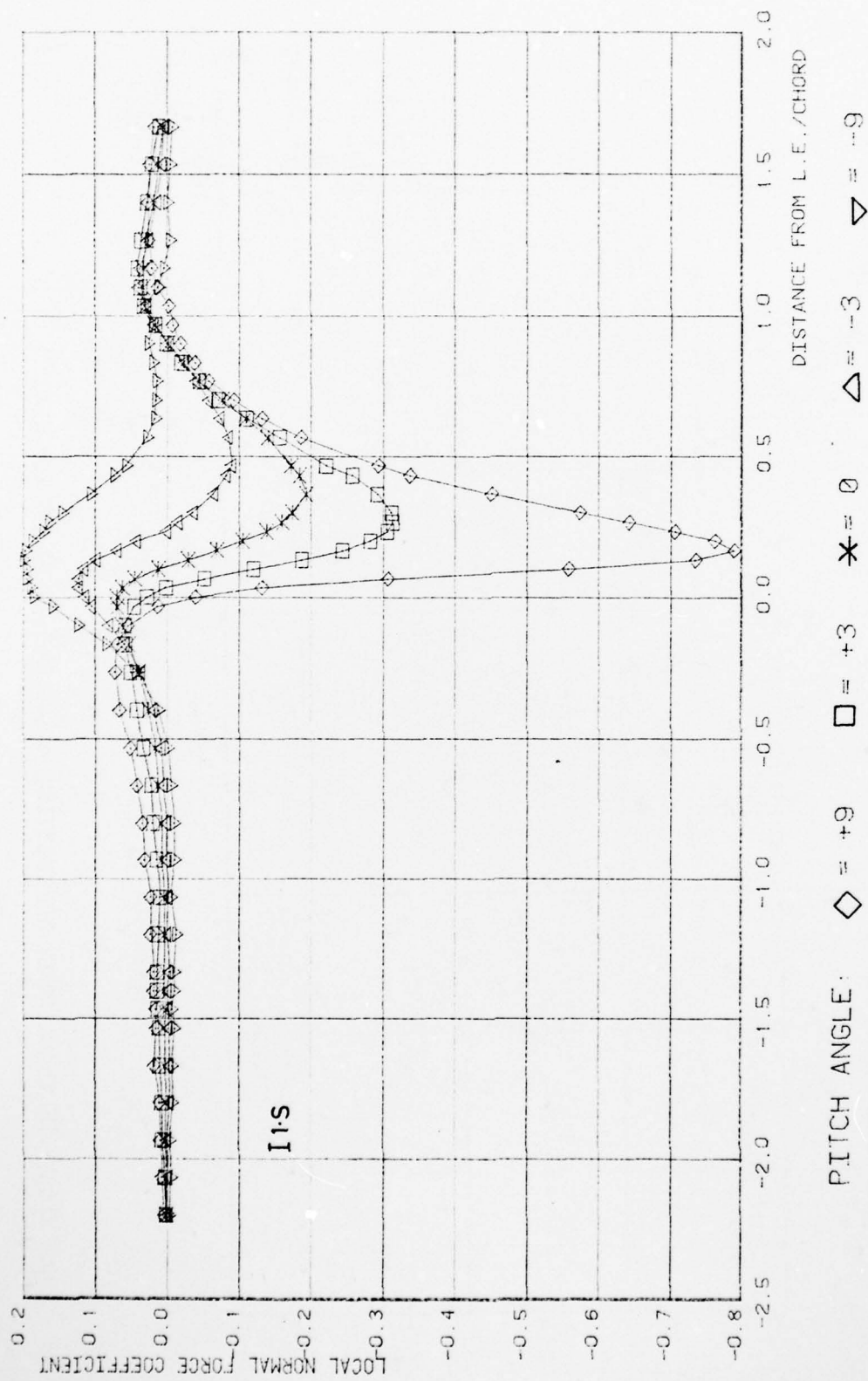
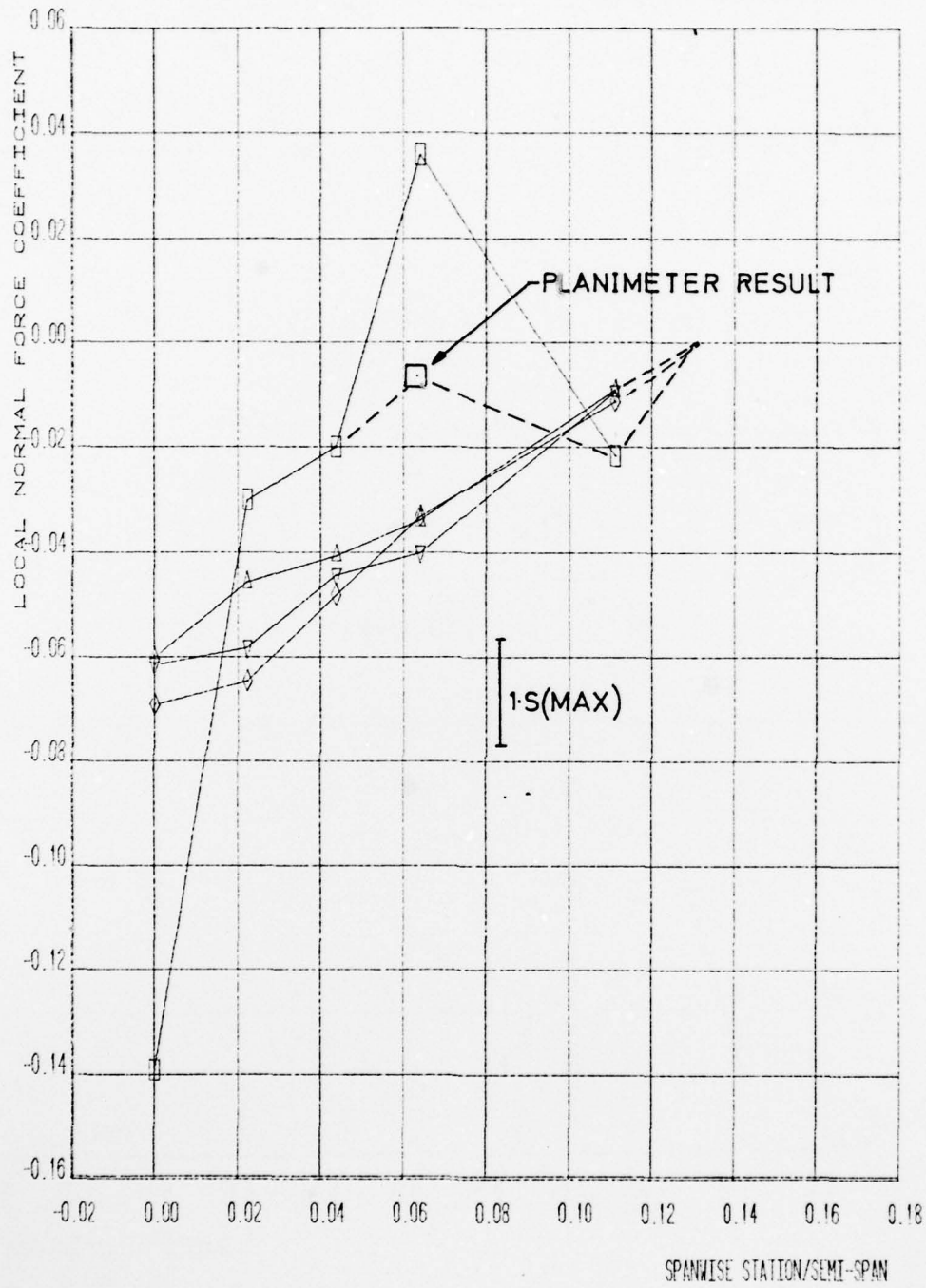
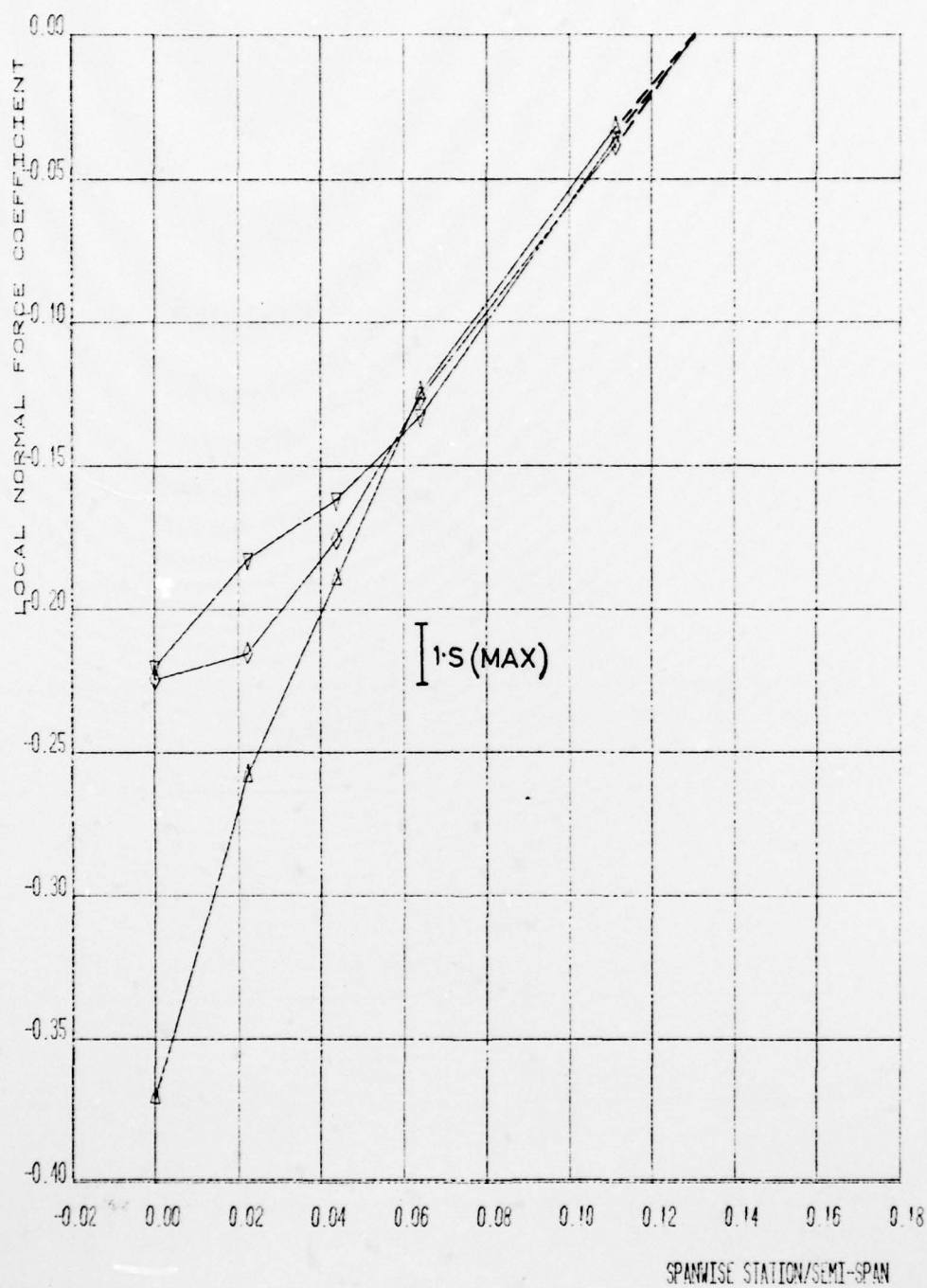


FIG. 25 - BODY CHORDWISE NORMAL FORCE DISTRIBUTION VERSUS WING PITCH ANGLE FOR LOW WING, $H/C = .45$



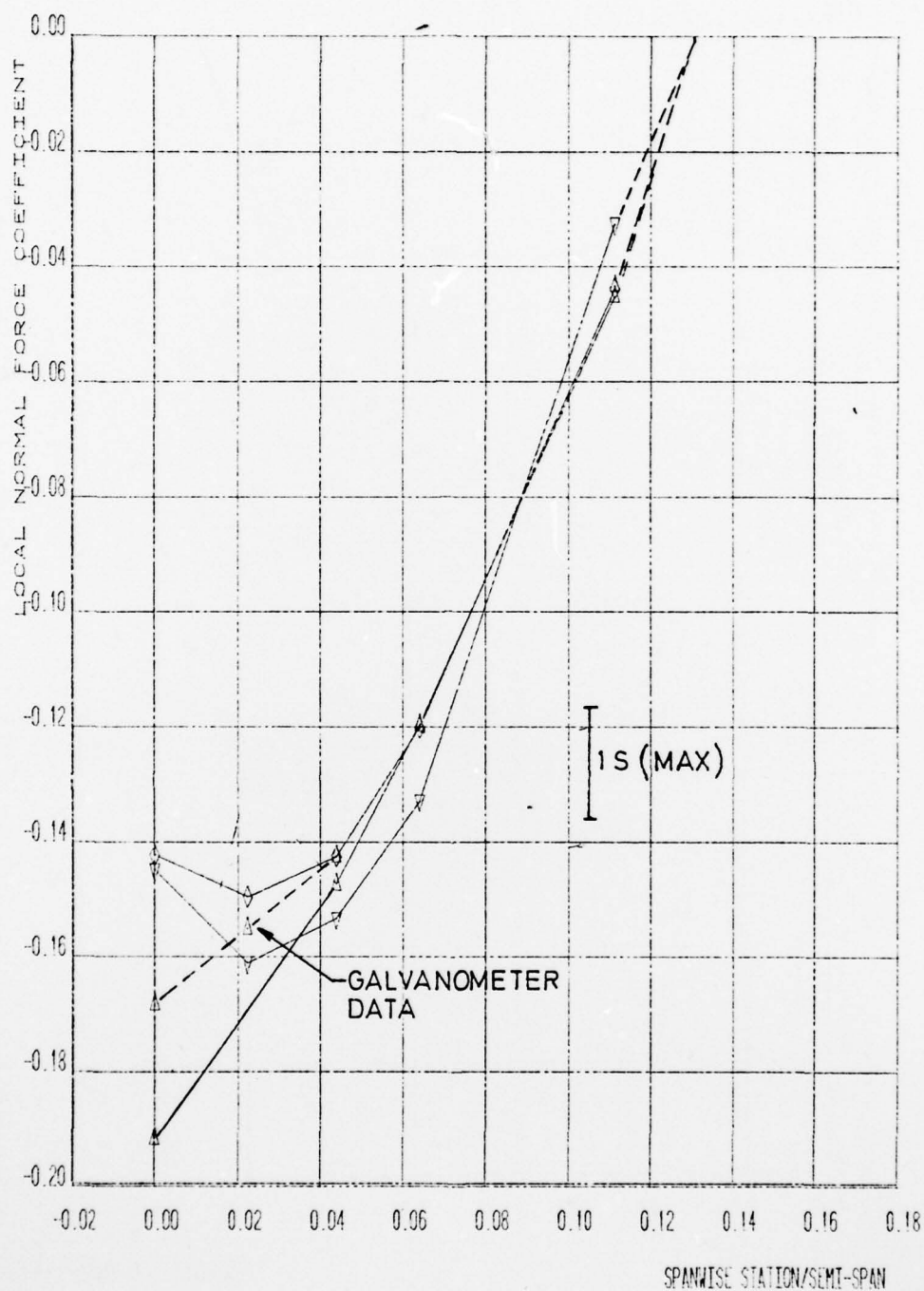
$$\text{GAP } H/C \quad \square = 0.39 \quad \triangle = 0.45 \quad \diamond = 0.51 \quad \nabla = 0.65$$

FIG. 26a - BODY SPANWISE NORMAL FORCE DISTRIBUTION VERSUS GAP HEIGHT
FOR HIGH WING, $\theta_w = 3^\circ$



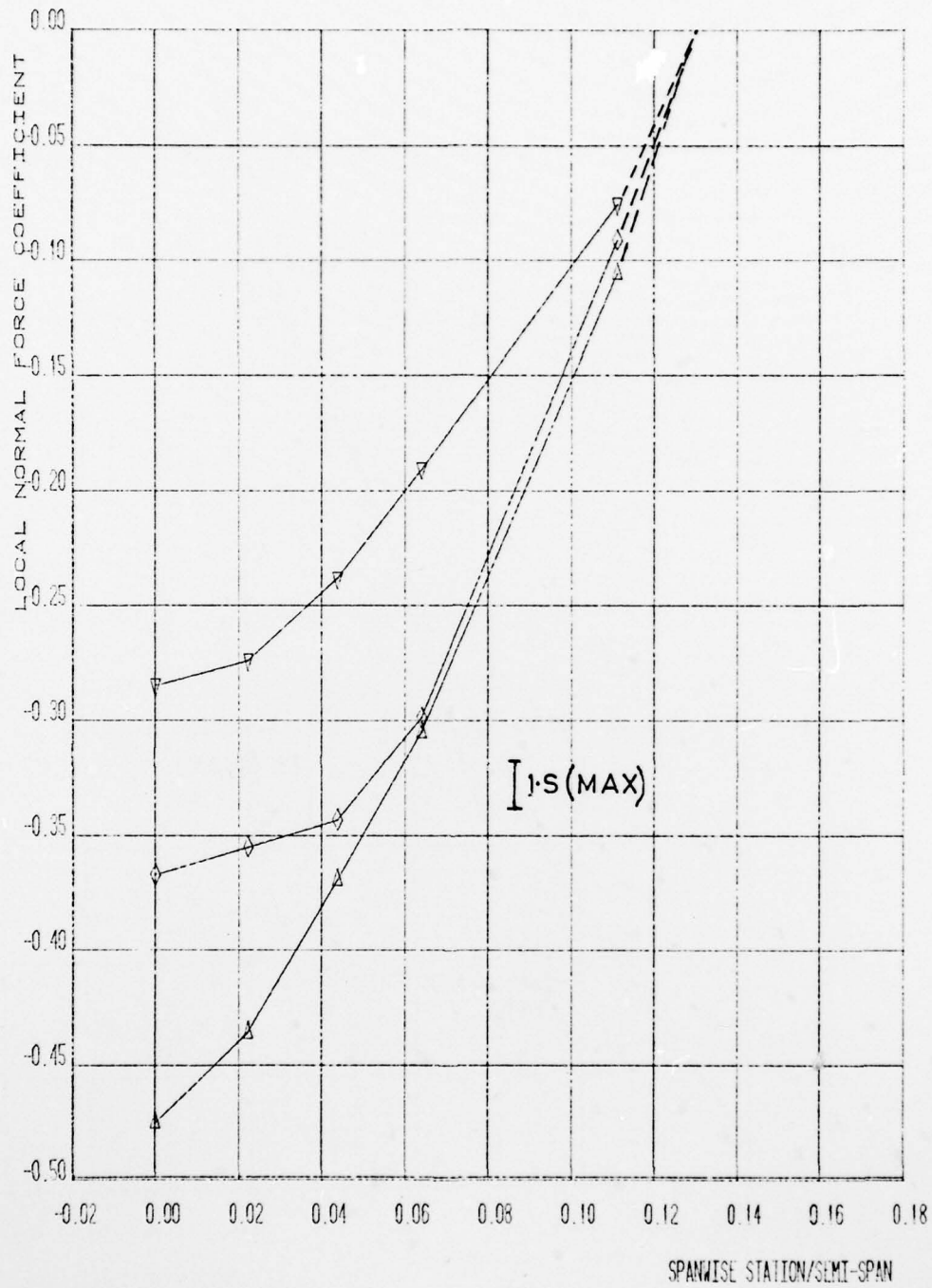
$GAP/H_c \Delta = 0.45 \quad \diamond = 0.52 \quad \nabla = 0.65$

FIG. 26b - BODY SPANWISE NORMAL FORCE DISTRIBUTION VERSUS GAP HEIGHT FOR HIGH WING, $\theta_w = 9^\circ$



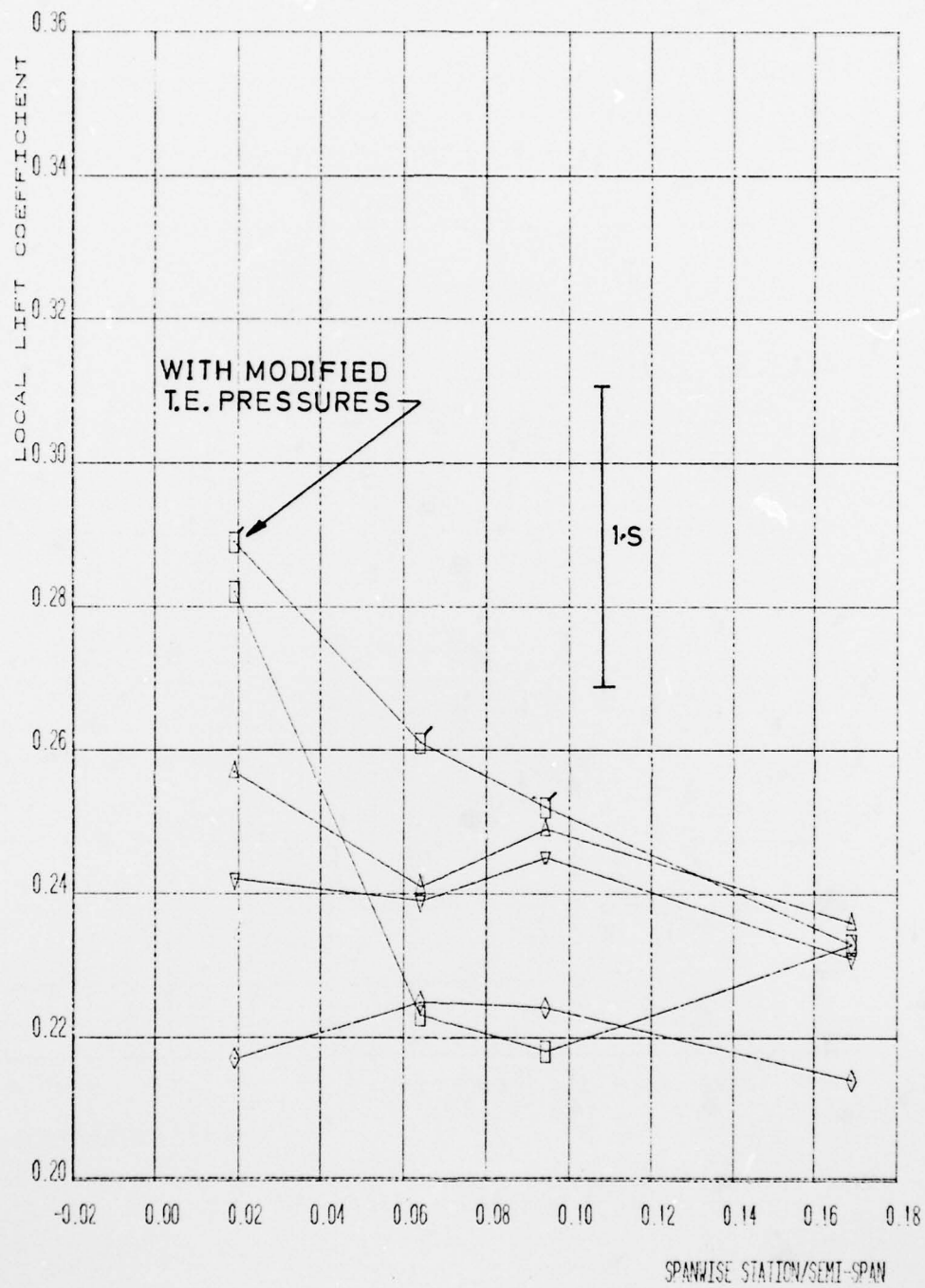
$$\text{GAP } \frac{H}{C} = 0.44 \quad \diamond = 0.51 \quad \nabla = 0.64$$

FIG. 27a - BODY SPANWISE NORMAL FORCE DISTRIBUTION VERSUS GAP HEIGHT FOR LOW WING, $\theta_w = 3^\circ$



$$GAP/H/C \triangle = 0.44 \quad \diamond = 0.50 \quad \nabla = 0.64$$

FIG. 27b - BODY SPANWISE NORMAL FORCE DISTRIBUTION VERSUS GAP HEIGHT FOR LOW WING, $\theta_w = 9^\circ$



GAP $\frac{H}{c}$ □ = 0.39 △ = 0.45 ◇ = 0.51 ▽ = 0.65

FIG. 28a - WING-SPANWISE LIFT DISTRIBUTION VERSUS GAP HEIGHT FOR HIGH WING

$\theta_w = 3^\circ$

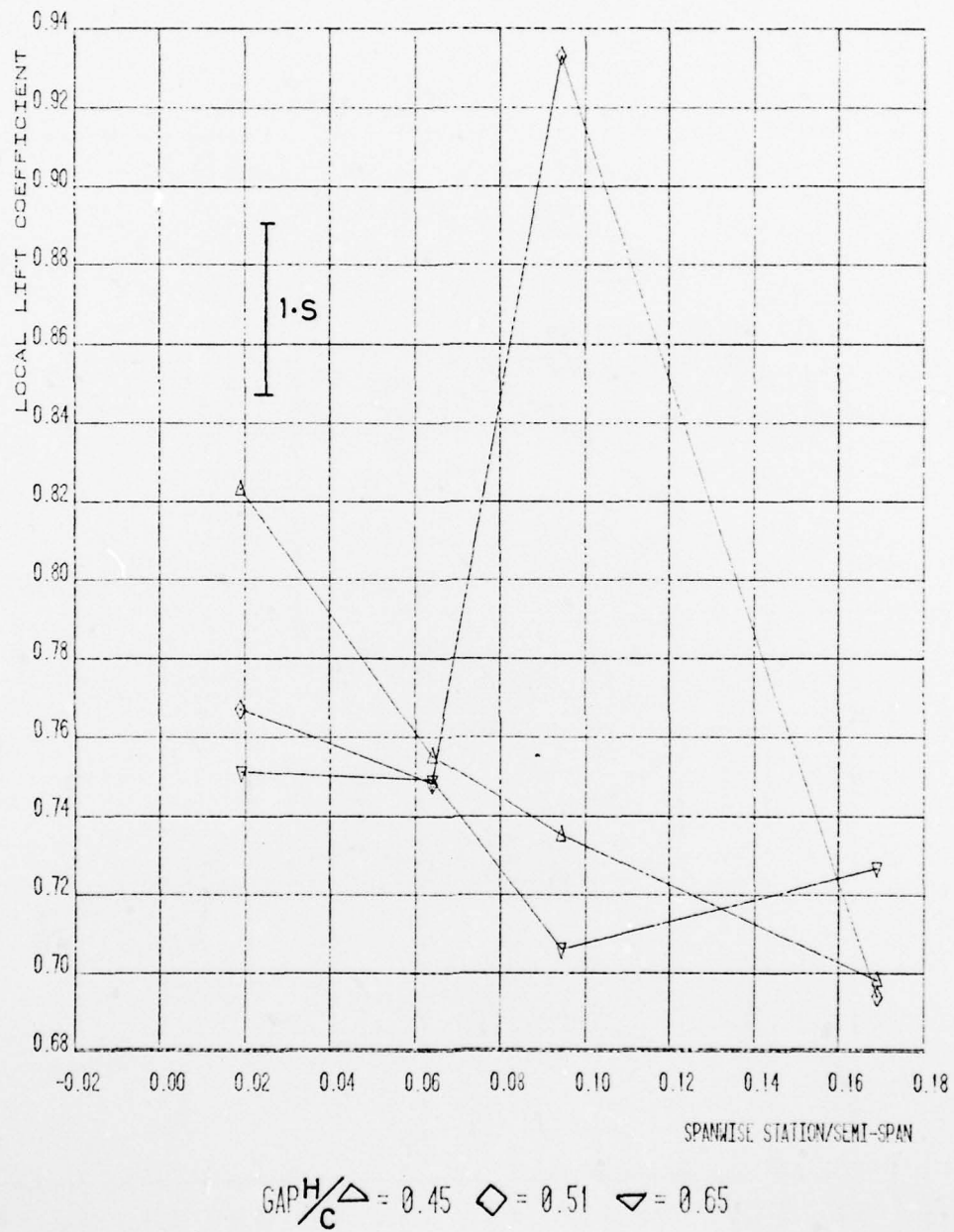
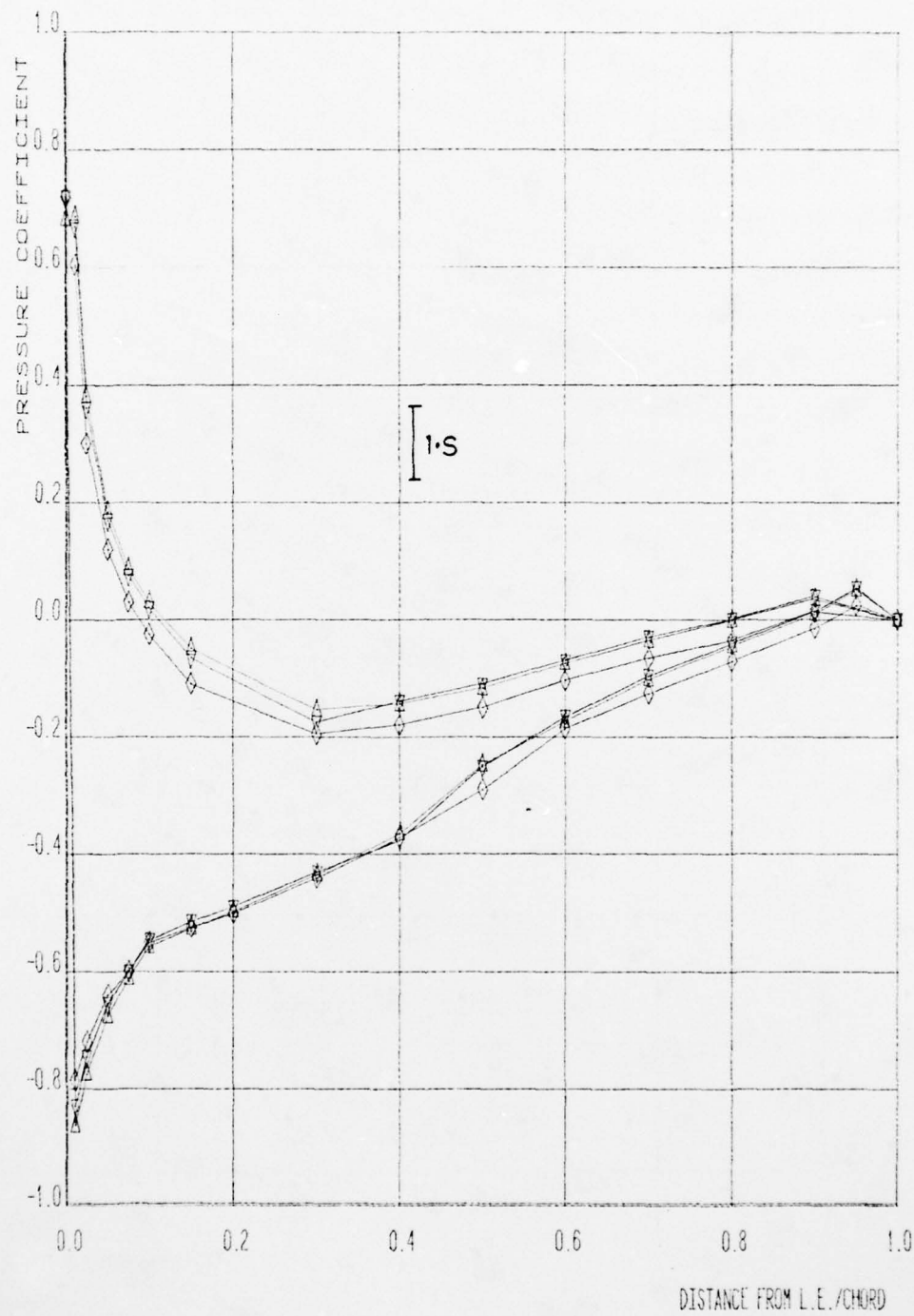
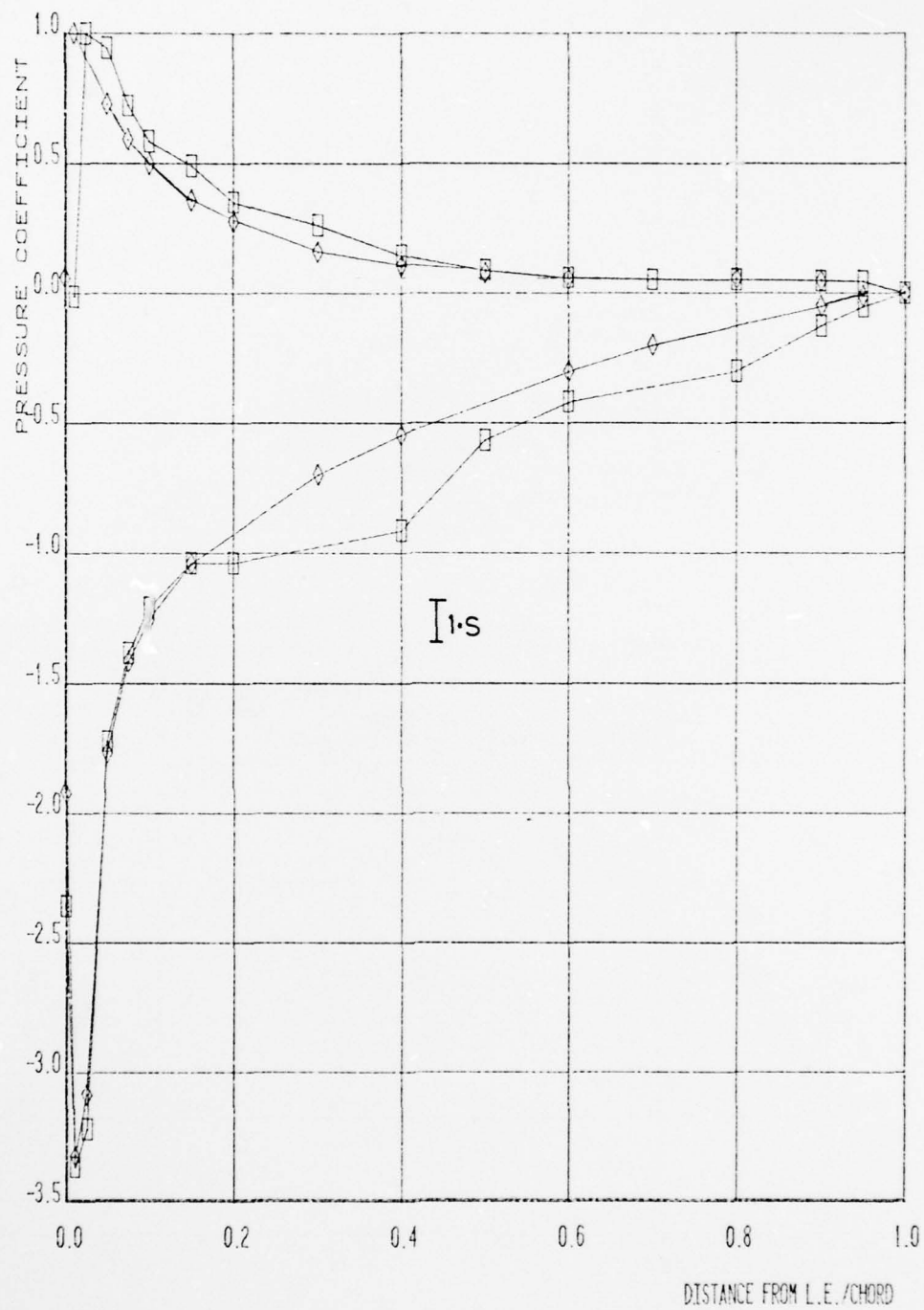


FIG. 28b - WING-SPANWISE LIFT DISTRIBUTION VERSUS GAP HEIGHT FOR HIGH WING
 $\theta_w = 9^\circ$



GAP $\frac{H}{C} \triangle = 0.45 \quad \diamond = 0.51 \quad \nabla = 0.65$

FIG. 29 - WING CHORDWISE PRESSURE DISTRIBUTION AT $Y/S = .169$ VERSUS GAP HEIGHT FOR HIGH WING, $\theta_w = 3^\circ$



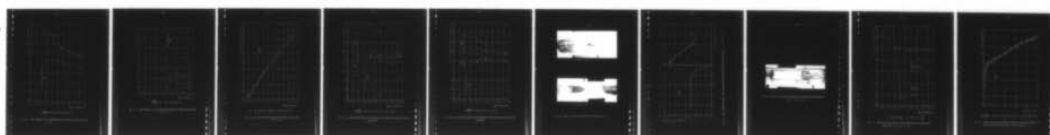
Y/S: $\square = 0.094$ $\diamond = 0.169$

FIG. 30 - WING CHORDWISE PRESSURE DISTRIBUTIONS FOR HIGH WING
 $\theta_w = 9^\circ$, H.C. = .51

AD-A078 957 VON KARMAN INST FOR FLUID DYNAMICS RHODE-SAINT-GENESE--ETC F/6 20/4
VARIATION OF SPANWISE CIRCULATION ACROSS AN AIRCRAFT FUSELAGE: --ETC(U)
OCT 79 R DOWGWILLO AFOSR-79-0099
UNCLASSIFIED VKI-1979-22 EOARD-TR-80-4 NL

2 OF 2

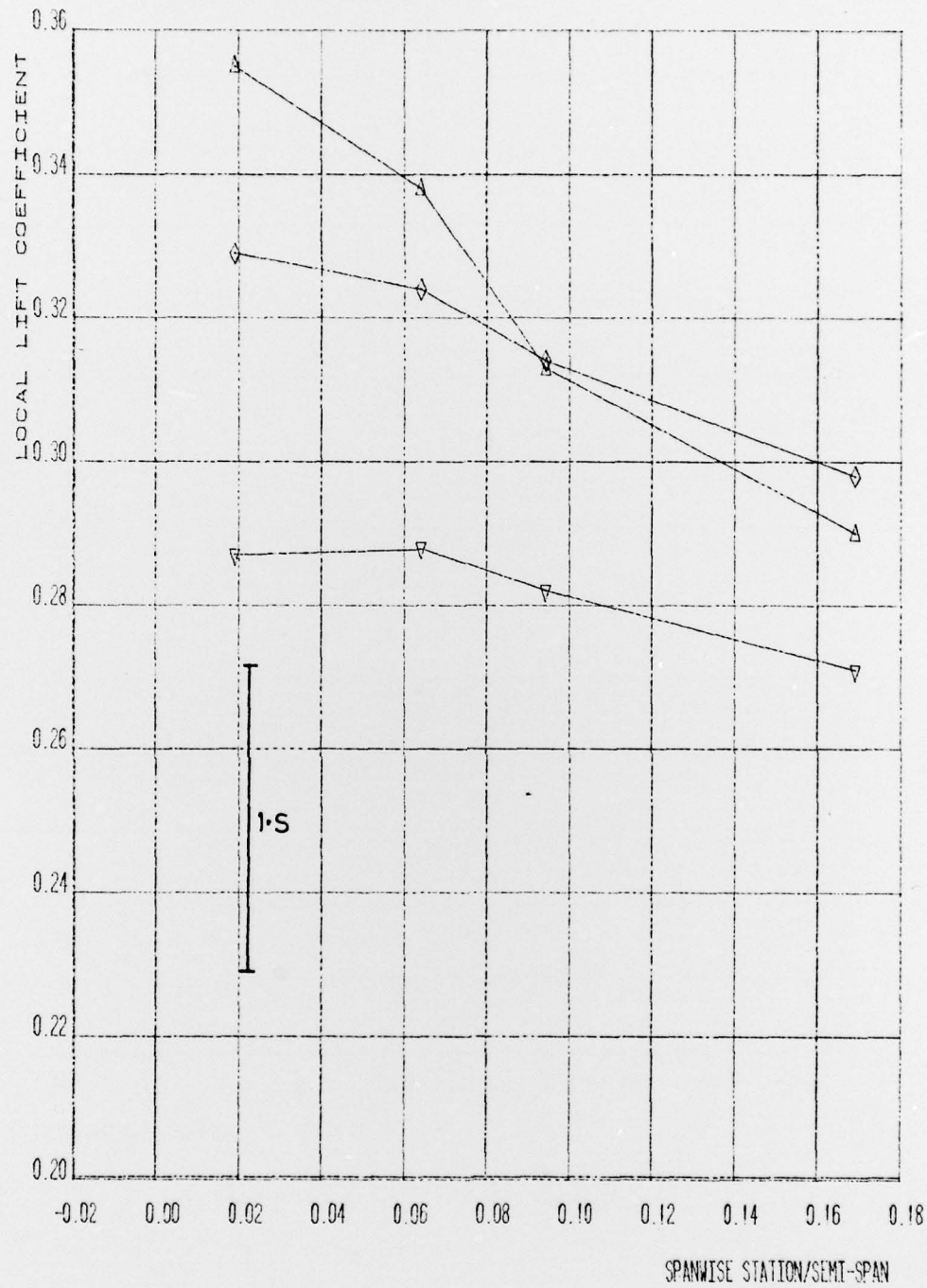
AD
A078957



END
DATE
FILMED

1 -80

DDC



$\text{GAP}/c = 0.44 \quad \diamond = 0.51 \quad \nabla = 0.64$

FIG. 31a - WING SPANWISE LIFT DISTRIBUTION VERSUS GAP HEIGHT FOR LOW WING
 $\theta_w = 3^\circ$

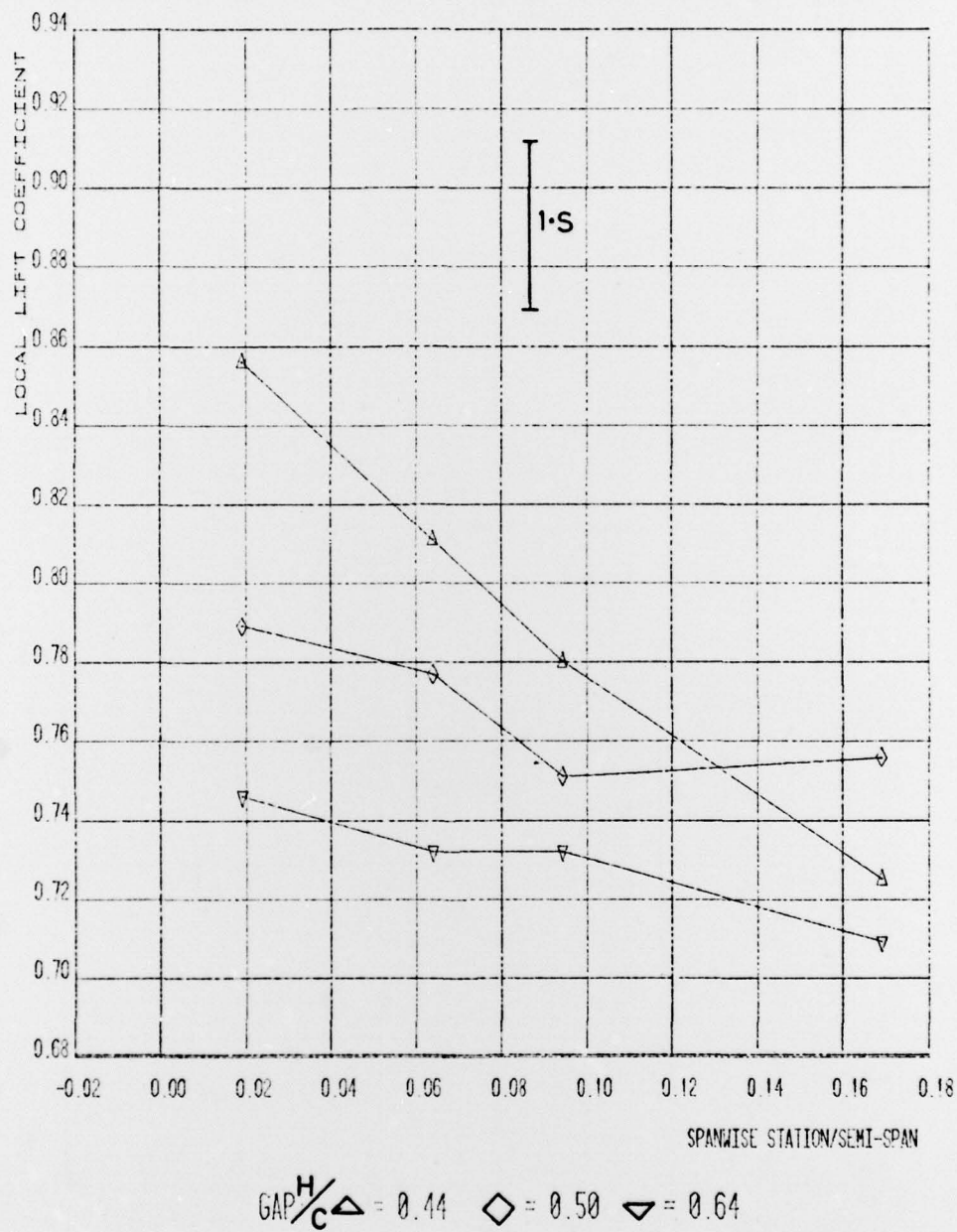
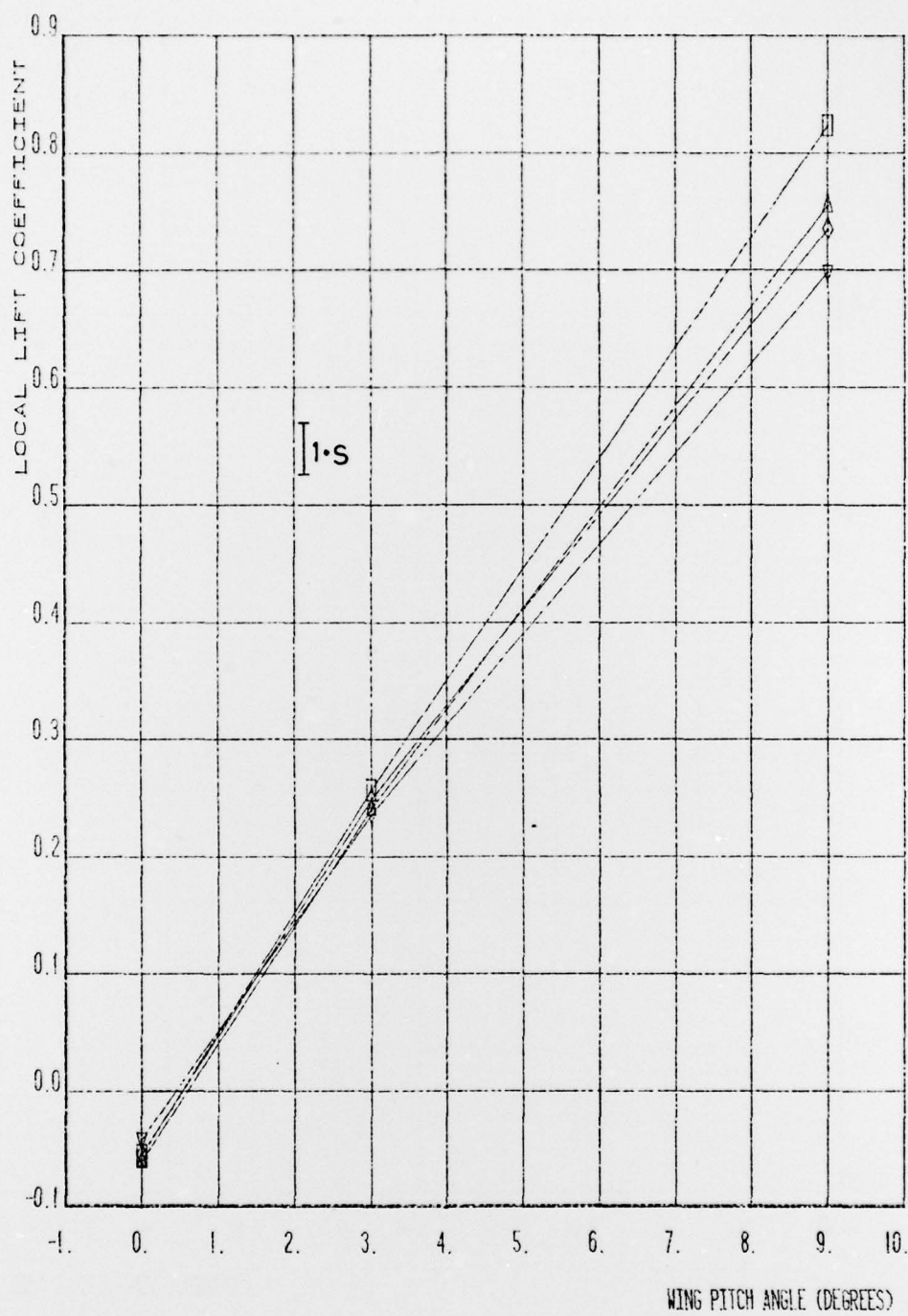
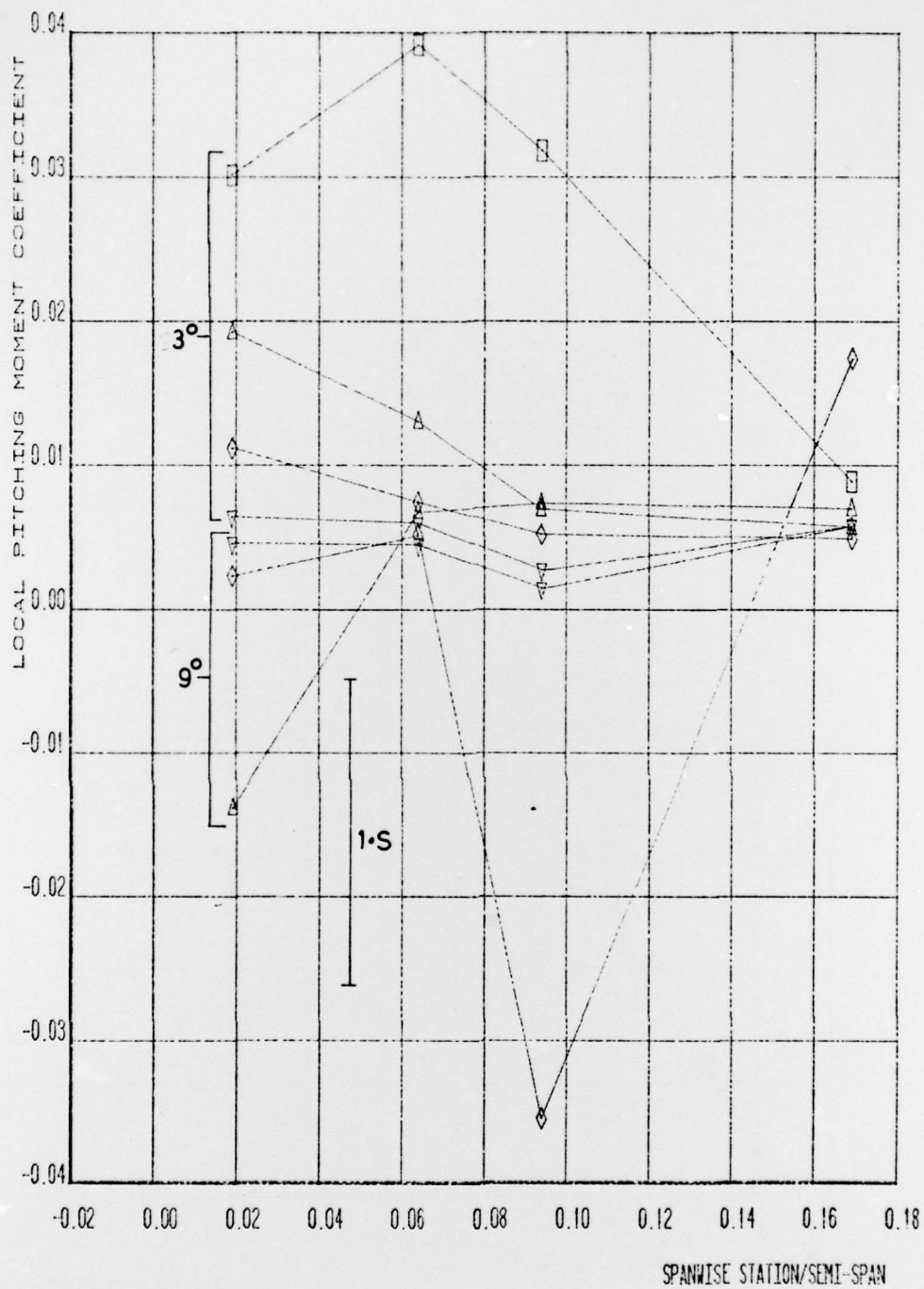


FIG. 31b - WING SPANWISE LIFT DISTRIBUTION VERSUS GAP HEIGHT FOR LOW WING
 $\theta_w = 9^\circ$



Y/S: □ = 0.019 △ = 0.064 ◇ = 0.094 ▽ = 0.169

FIG. 32 - WING LIFT CURVE VERSUS WING STATION FOR HIGH WING
H/C = .39



$$\text{GAP } \frac{H}{c} \square = 0.39 \quad \triangle = 0.45 \quad \diamond = 0.51 \quad \nabla = 0.65$$

FIG. 33a - WING QUARTER-CHORD PITCHING MOMENT DISTRIBUTIONS VERSUS GAP HEIGHT
- HIGH WING -

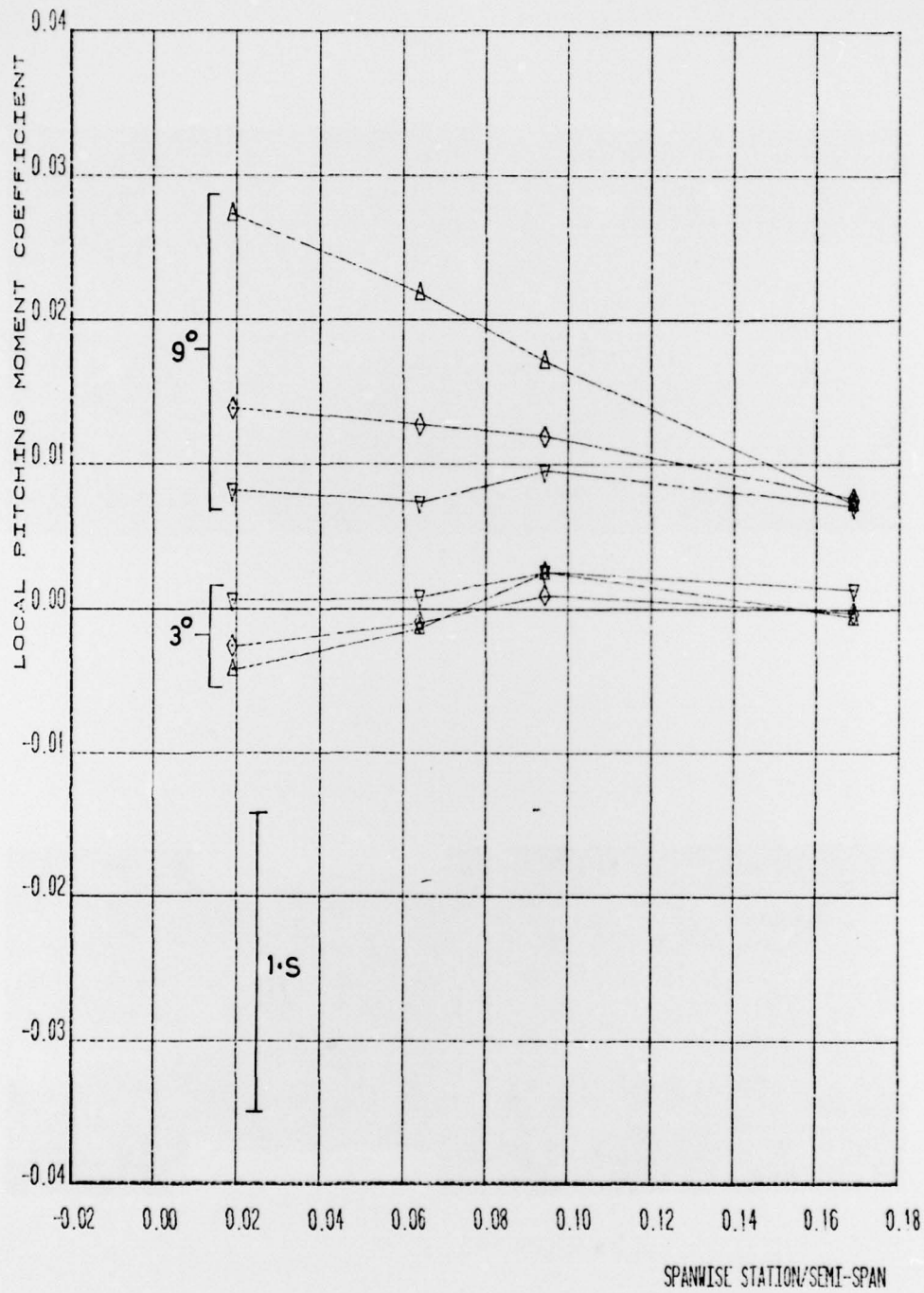
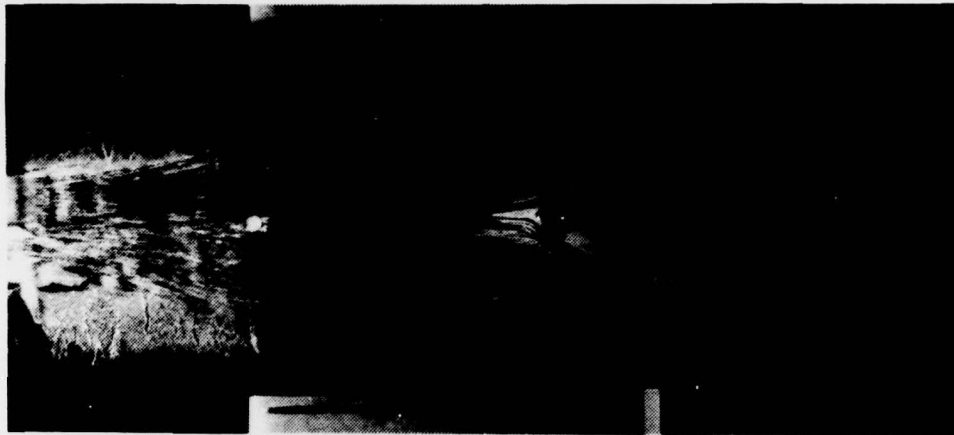
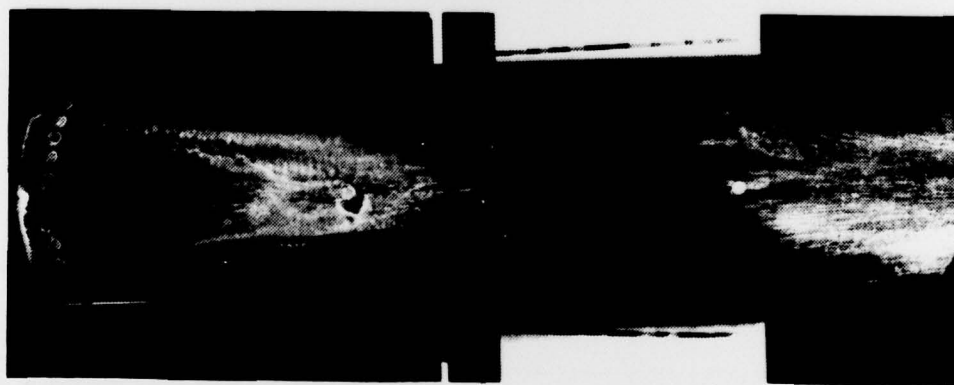


FIG. 33b - WING QUARTER-CHORD PITCHING MOMENT DISTRIBUTIONS VERSUS GAP HEIGHT
- LOW WING -



a) $H/C = .39$



b) $H/C = .45$

FIG. 34 - BODY OIL FLOW VISUALIZATION FOR LOW WING $\theta_w = 9^\circ$

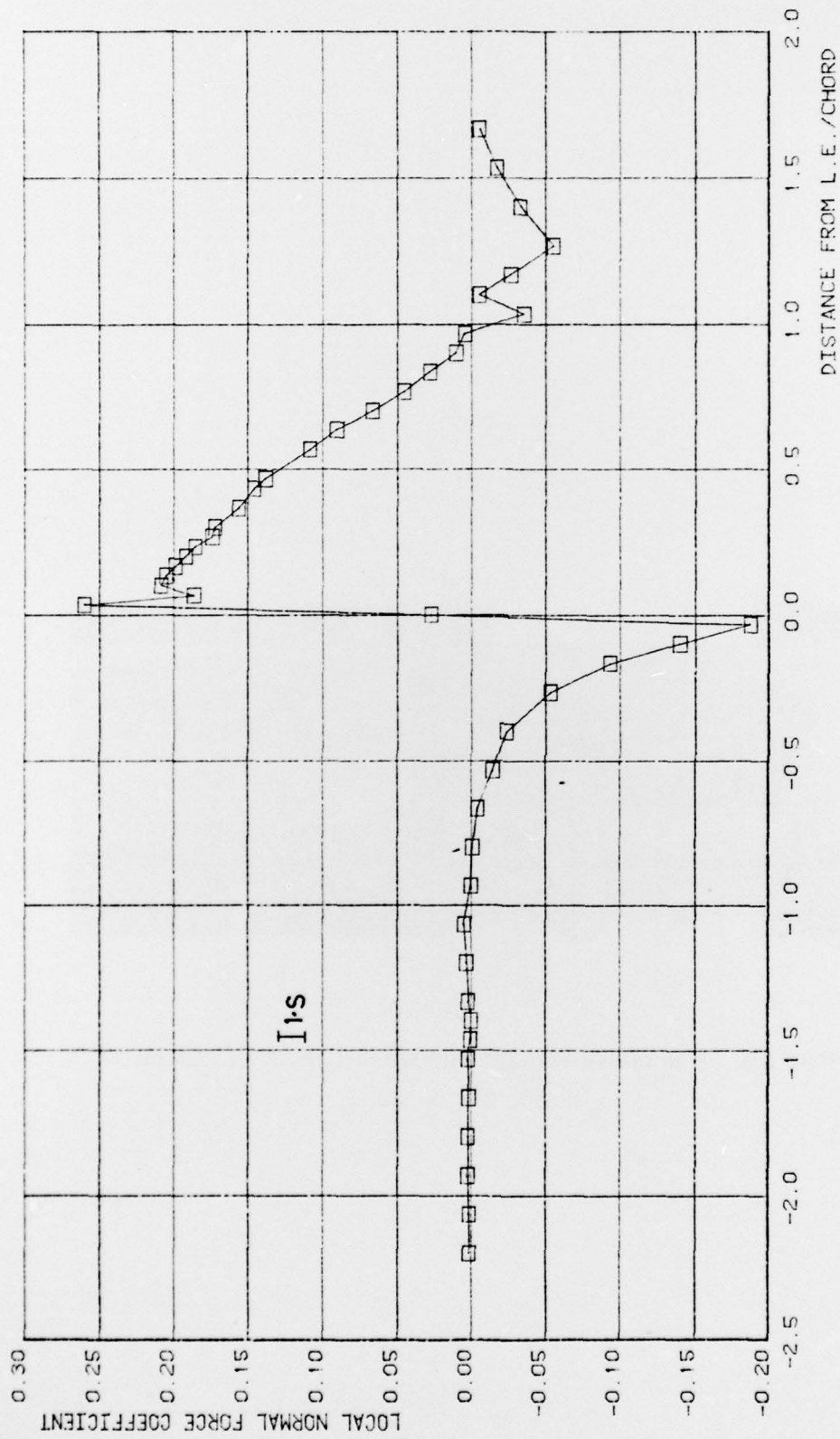


FIG. 35 - BODY CHORDWISE NORMAL FORCE DISTRIBUTION FOR HIGH WING WITH SEALED GAP, $\theta_w = 3^\circ$, $H/C = .40$

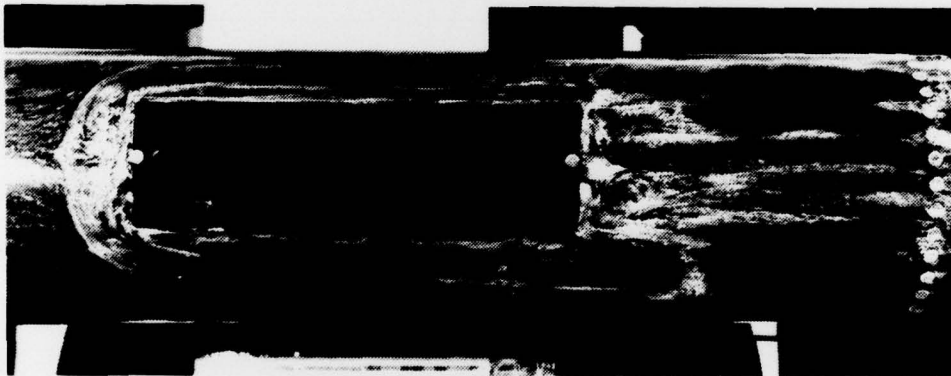


FIG. 36 - BODY OIL FLOW VISUALIZATION FOR HIGH WING WITH SEALED GAP

$$\theta_w = 3^\circ, H/C = .40$$

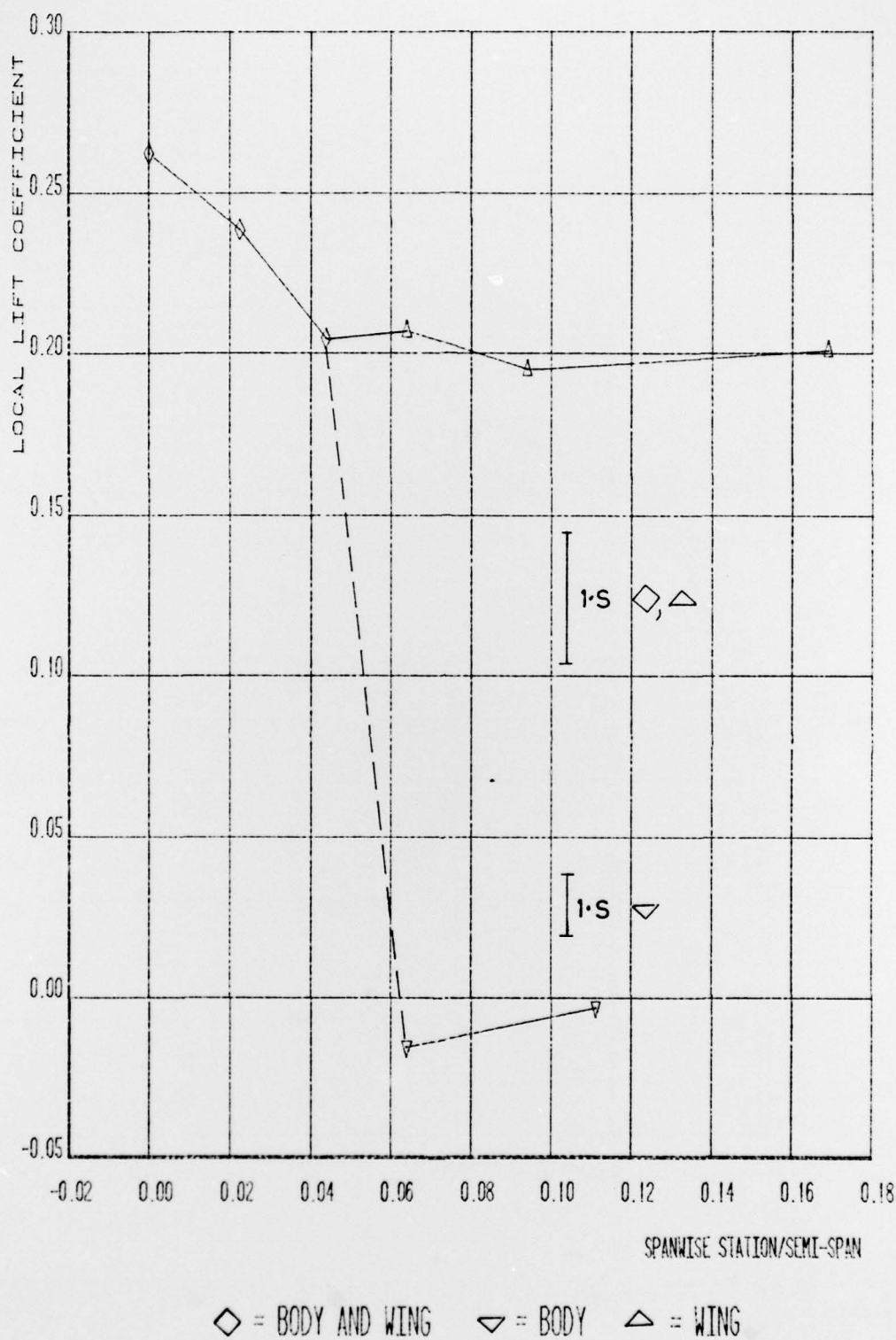
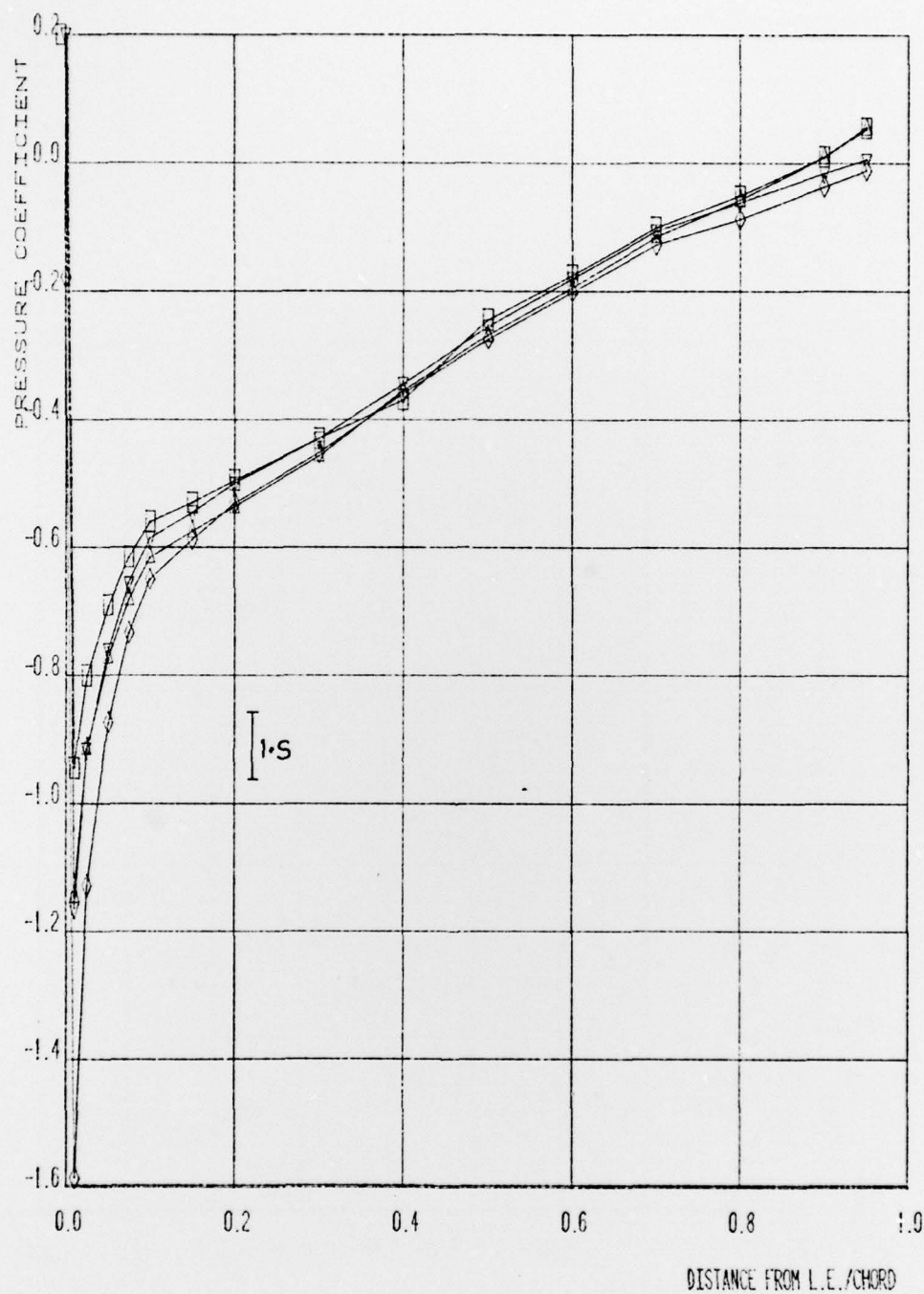


FIG. 37 - CONFIGURATION SPANWISE LIFT DISTRIBUTION FOR HIGH WING WITH SEALED GAP, $\theta_w = 3^\circ$, $H/C = .40$



GAP H/C ∇ = 0.389 \triangle = 0.446 \square = 0.646 \diamond = 0.400 (SEALED GAP)

FIG. 38 - UPPER SURFACE WING CHORDWISE PRESSURE DISTRIBUTION VERSUS GAP HEIGHT, INCLUDING SEALED GAP, FOR HIGH WING, $\theta_w = 3^\circ$